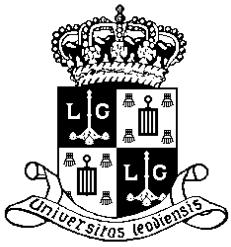

UNIVERSITÉ DE LIÈGE
FACULTÉ DES SCIENCES

GENIEsim: the GENIE Science Simulator

Mémoire de fin d'études présenté par

Olivier ABSIL

en vue de l'obtention du Diplôme
d'Etudes Approfondies en Sciences.

Année académique 2002-2003.

Acknowledgements

First and foremost, I would like to express my deepest gratitude to my advisor, Jean Surdej. Since the beginning of my diploma thesis, he has always been there to lead me in the right direction. I thank him for his patience and dedication.

I wish to express my very special thanks to Philippe Gondoin for giving me the opportunity to work on the GENIE project, and to all the members of the ESA GENIE Team, especially Roland den Hartog and Lisa Kaltenegger, without whom the content of this thesis would have been much less complete. Their kindness and enthusiasm made my stays in Noordwijk a real pleasure.

I am also very grateful to Vincent Coudé du Foresto and Pierre Léna for inviting me to spend one year in Meudon in 2001-2002, and to all the members of the Interferometry Group at Observatoire de Meudon for making this stay an enjoyable experience. Working with Vincent during this year has been an invaluable experience. I thank him for his incomparable support and for countless advice on interferometry.

My thanks also go to Prof. J.-P. Swings and Prof. C. Jamar for accepting to read and evaluate this thesis.

I also wish to give thanks to the Alcatel GENIE Team, especially Marc Barillot and Cyril Ruilier, for constructive and fruitful discussions about GENIE and its technological challenges. My warmest thanks also go to Frédéric Cassaing and Emmanuel di Folco for inviting me several times in ONERA and for their incomparable support in the field of fringe tracking.

Finally, I take a particular pleasure in thanking my wife, Véronique, for her help in typesetting this thesis and for her unconditional love and support.

This research was supported by a fellowship from the Belgian National Science Foundation ("Aspirant du F.N.R.S."). During his stay at the Observatoire de Paris, the author was supported through a European Community Marie Curie Fellowship

Contents

Notations and abbreviations

Atmospheric windows

K band:	from 2.0 to 2.4 μm
L' band:	from 3.5 to 4.1 μm
M band:	from 4.5 to 5.1 μm
N band:	from 8 to 13 μm

Notations

R_*, T_*, L_*:	radius, temperature and luminosity of the star
B_ν, B_λ:	surface brightness, respectively per frequency and per wavelength unit
B:	surface brightness, integrated on the waveband
F_ν, F_λ:	total flux, respectively per frequency and per wavelength unit
F:	total flux, integrated on the waveband (in Watts or in photons/sec)

Units

arcmin (or '):	minute of arc ($\simeq 2.9 \times 10^{-4}$ radian)
arcsec (or "):	second of arc ($\simeq 4.85 \times 10^{-6}$ radian)
mas:	milli-arcsec (10^{-3} arcsec)
AU:	Astronomical Unit ($\simeq 1.495 \times 10^{8}$ km)
pc:	parsec ($\simeq 3.08 \times 10^{14}$ km)
Jy:	Jansky (10^{-26} W m^{-2} Hz^{-1})

Abbreviations

AMBER:	Astronomical Multiple Beam Recombiner (near-IR instrument for the VLTI)
AO:	Adaptive Optics
AT:	VLTI Auxiliary Telescope (1.8 m)
CCD:	Charge-Coupled Device
COBE:	Cosmic Background Explorer
DAC:	Degenerated Angel Cross
DIRBE:	Diffuse Infrared Background Experiment
DL:	Delay Line
DM:	Deformable Mirror
ESA:	European Space Agency
ESO:	European Southern Observatory
FINITO:	Fringe Tracking Instrument of Nice and Torino
FLUOR:	Fiber Linked Unit for Optical Recombination
FoV:	Field-of-View
FSU:	Fringe Sensing Unit
IR:	Infrared
IRAS:	Infra-Red Astronomical Satellite
MACAO:	Multi Application Curvature Adaptive Optics
MICS:	Mid-Infrared Camera and Spectrometer
MIDI:	Mid-Infrared instrument for the VLTI
OPD:	Optical Path Difference
OPDC:	OPD Controller
PRIMA:	Phase-Referenced Imaging and Microarcsecond Astrometry
PSD:	Power Spectral Density
RMS:	Root Mean Square
SED:	Spectral Energy Distribution
SNR:	Signal-to-Noise Ratio
STRAP:	System for Tip-tilt Removal with Avalanche Photodiodes
SU:	Sensing Unit
TPF:	Terrestrial Planet Finder
TRP:	Technology Research Program
UKIRT:	United Kingdom Infra-Red Telescope
UT:	VLTI Unit Telescope (8 m)
VLTI:	Very Large Telescope Interferometer
WDA:	Water-vapor Displacing Air
YSO:	Young Stellar Object

Chapter 1

Introduction

1.1 The Darwin/TPF mission

Darwin is one of the most challenging space projects ever considered by the European Space Agency (ESA). Its principal objectives are to detect Earth-like planets around nearby stars, to characterize their atmospheres and to search for potential signs of biological activity in order to answer central questions such as "How unique is the Earth as a planet?" and "How unique is life in the Universe?".

Direct detection of Earth-size bodies orbiting nearby stars is extremely difficult because of the weak planetary signal emitted within a fraction of an arcsecond from an overwhelmingly bright star. A solar type star outshines an Earth size planet by a factor of more than 10^9 in the visible wavelength range. In the infrared spectral range, where the planet's thermal emission increases and the star's emission decreases, the contrast is still higher than 10^6. Only the planetary signal, a millionth of the stellar light, should remain in the input feed of a spectrograph in order to register a planet spectrum in a reasonable time. To accomplish such an extinguishing of light at the relevant spatial scales, the technique of *nulling interferometry* has been selected for Darwin.

The principle of nulling interferometry is to combine the light incident on a array of telescopes in a co-axial mode, adjusting their respective phases in order to produce a totally destructive interference on the optical axis. Figure 1.1 illustrates the theoretical design of such an interferometer, in the case of two telescopes (*Bracewell interferometer* [Bra78]). The recombining system induces an achromatic phase shift of π radians between the two electric fields to achieve the destructive interference. By placing the central star under this null and by adjusting the interferometer baseline to the required angular resolution, planets can be detected in the "habitable zone" of their parent star. The actual shape and transmission properties of the pattern around the central null depend on the configuration and the distance between the telescopes.

It must be stressed that the destructive interference takes place in a pupil plane. Nulling interferometry cannot be performed in the image plane because the central dark fringe would only cancel a part of the stellar image (the fringe pattern is much narrower

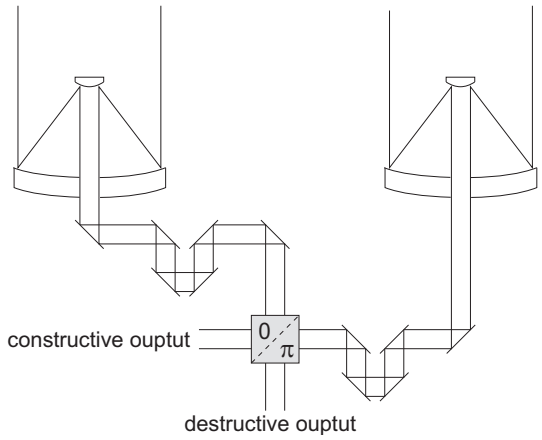

Figure 1.1: Principle of a Bracewell nulling interferometer. The recombining system produces a destructive interference by applying an achromatic π phase shift to one of the two input beams and by superposing them in a co-axial way.

than the diffraction pattern associated to the star). Therefore, *no image is formed*: the flux transmitted by the interferometer is integrated over the whole field-of-view. This is a major difficulty associated with nulling interferometry: one cannot immediately tell whether an unusually high flux at the destructive output is due to the presence of a planet, of circumstellar dust or to a bad suppression of the stellar light.

The Darwin mission concept [ESA00] consists of six 1.5 m telescopes, each of which is a free flying spacecraft transmitting its light to a central beam-combining unit (see Figure 1.2). Using the nulling interferometry technique, the beam-combiner extinguishes the stellar light by destructive interferences on-axis and transmits the off-axis signal of the orbiting planet. The light from Earth-like planets at interstellar distances of up to 25 pc can then be analyzed.

1.2 The Darwin Technology Research Programme

In order to develop the innovative technologies required for Darwin, an ambitious Technology Research Programme (TRP) has been initiated by ESA.

1.2.1 Formation flying

The mission concept is based on the ability to co-phase telescopes on independent spacecrafts to an accuracy better than 20 nm and to perform nulling interferometry with a rejection factor of $\sim 10^5$ in a wide spectral band extending from 5 to 18 μm. In-orbit co-phasing of the free-flying telescopes is performed in successive steps combining first a local radio-frequency (RF) positioning system with milli-Newton propulsion devices, then inter-satellite laser metrology with micro-Newton propulsion devices and finally

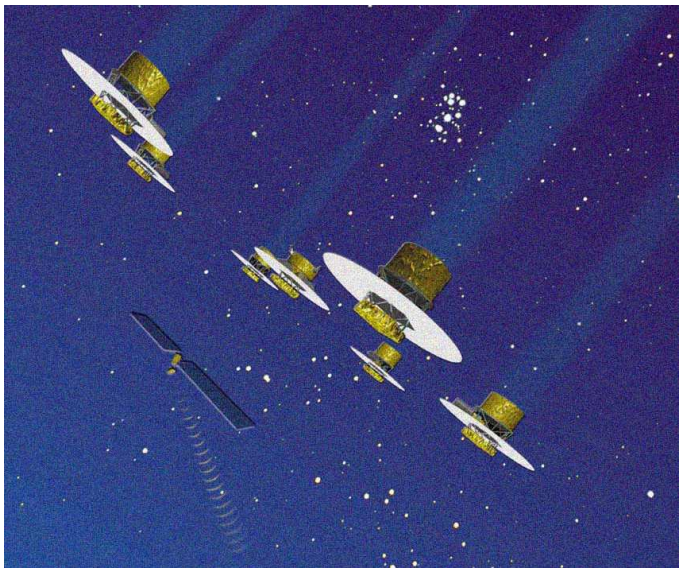

Figure 1.2: Artist view of the Darwin Space Interferometer orbiting at the Sun-Earth L2 point (courtesy Alcatel Space Division).

fringe sensors with optical delay lines. These items are currently being developed within the Darwin TRP. It is considered to test them in-orbit within the frame of the ESA SMART technology demonstration program. The following items are currently studied under TRP contracts [FG03]:

- *Metrology*: RF ranging (for deployment and coarse acquisition), laser metrology and fringe sensing.
- *Actuators*: Field Emission Electric Propulsion (μN and mN thrusters) and μN cold gas thrusters.
- *Control software*: deployment, optical path delay control (using fringe sensor and/or high precision optical metrology), formation flying command and control.

The simulation of formation flying is a part of the FINCH system simulator (Fast Interferometer Characterization), an end-to-end simulation software for the Darwin space interferometer currently developed under TRP activities.

1.2.2 Nulling interferometry

In addition to the co-phasing of free-flying telescopes, a second key issue for Darwin is the nulling interferometry technique. Hence, the TRP activities also include the development of Darwin specific optical components, namely achromatic phase shifters, wavefront filtering devices and IR single mode fibers, integrated optics, IR detectors,

electronics and coolers, optical delay lines and fringe sensors as well as other components for interferometry.

Laboratory nulling breadboards with star-planet simulators are currently evaluating the performance of the nulling interferometric technique. These innovative breadboards use the narrow telecommunication band around 1.65 μm where off-the-shelf components are available. Based on their performance, a follow-up activity has been identified which will adapt their design to the mid-IR band and test the nulling interferometry technique on sky in Darwin representative operating conditions.

1.3 The GENIE project

Within the frame of the Darwin technology program, the European Space Agency (ESA) and the European Southern Observatory (ESO) have initiated a definition study for a ground-based technology demonstrator called GENIE (Ground-based European Nulling Interferometry Experiment). This ground-based demonstrator built around the Very Large Telescope Interferometer (VLTI, Figure 1.3) in Paranal will test some of the key technologies required for the Darwin Infrared Space Interferometer. It will demonstrate that nulling interferometry can be achieved in a broad mid-IR band as a precursor to the next phase of the Darwin program. The definition study will assess the technical feasibility of the experiment and establish its design, performance, programmatics and cost. If successful, the definition study will be the base for ESA and ESO to move into the hardware development, integration and exploitation phases of the GENIE project.

Figure 1.3: The ESO Very Large Telescope Interferometer, with its four 8-m Unit Telescopes, an artist view of three of its four 1.8-m Auxiliary Telescopes, and its central interferometric laboratory.

1.3.1 A technology demonstrator

The primary objective of the GENIE nulling experiment is to gain experience on the design, manufacture and operation of a nulling interferometer using Darwin representative concept and technology. Nulling tests with the highest rejection factor on single stars or close binaries in broad mid-IR spectral bands will achieve this objective with the limitations imposed by the turbulence and infrared background of the Earth atmosphere. A starlight rejection rate of 10^{-3} is required for nearby main-sequence stars[1], with a goal of 10^{-4}.

The GENIE experiment will combine all optical functions foreseen in the future Darwin Infrared Space Interferometer. It will benefit from the existing VLTI infrastructure, including the 8-m Unit Telescopes (UT) and 1.8-m Auxiliary Telescopes (AT) with chopping and adaptive optics, delay lines, fringe sensors and a beam combiner laboratory. The overall performance of the instrument will depend on the performance of all VLTI subsystem and in particular on the adaptive optics and co-phasing subsystems. The GENIE optical bench within the VLTI laboratory will provide the functions specific to the nulling interferometry technique, namely photometry and amplitude control, polarization matching, phase shifting, beam combination and internal modulation, spatial filtering, spectrometry, detection, electronics and cryogenics. The detailed architecture of GENIE will be established during the definition study. It will take into account the ESO VLTI interface characteristics and the output of the ESA TRP activities.

1.3.2 A preparation of the Darwin science program

The second main objective of GENIE is to prepare the Darwin science program through a systematic survey of Darwin candidate targets. The solar zodiacal cloud, a sparse disk of 10-100 μm diameter silicate grains, is the most luminous component of the solar system after the Sun. Its optical depth is only $\sim 10^{-7}$, but a patch of the solar zodiacal cloud 0.3 AU across has roughly the same flux as an Earth sized planet. Similar and even brighter clouds may be common in other planetary systems and present a severe obstacle for the direct detection of extra-solar terrestrial planets. A systematic survey of Darwin candidate targets will screen-out those stars for which circumstellar dust prevents the detection of Earth-like planets.

Bright exozodiacal clouds are easier to detect than extra-solar terrestrial planets, but finding an exozodiacal cloud is still difficult. The total emission from our zodiacal cloud is no more than 10^{-4} of the Sun's at any wavelength. Photometric surveys like the Infrared Astronomical Satellite (IRAS) survey can only detect exozodiacal clouds that are at least 500 times as optically thick as the solar clouds [BP93]. Attempts to spatially resolve faint exozodiacal clouds with single dish telescopes in the mid-infrared [KBK98] and near infrared [KB00] have not yielded better detection limits. A nulling interferometer using the ESO VLTI 8-m Unit Telescopes will provide a much better sensitivity.

[1] The typical target for GENIE is a Sun-like star at 10 pc.

GENIE also aims at performing Darwin-related science including the characterization of debris disks around main-sequence stars and of proto-planetary disks around Young Stellar Objects. The detection and low-resolution spectroscopy of low-mass companions (including brown dwarfs and hot Jupiters) orbiting nearby stars is also an objective of the GENIE project and would provide an excellent demonstration of nulling interferometry.

Finally, GENIE will also be a general-user instrument that will be useful to study any target requiring both a high dynamic and a high angular resolution. Besides circumstellar environments and high-contrast binaries, Active Galactic Nuclei could benefit from the capabilities of GENIE.

1.4 The need for a GENIE science simulator

In the design of such a complex instrument as GENIE, early access to simulation software is a valuable asset. For example, the choice of the operation wavelength and the design of the control subsystems are two critical points that cannot be addressed without a realistic simulation of the instrument operation. Therefore, we are currently building an IDL package called GENIEsim to simulate future observations with the GENIE instrument, taking into account all noise sources encountered in ground-based interferometry. The objectives of the simulator are the following:

- define GENIE functions, operation and calibration modes,
- define top-level specifications,
- quantify the impact of the atmosphere,
- trade-off between different concepts and/or designs,
- estimate GENIE performance,
- simulate GENIE observation scenarios and nulling tests,
- test data reduction and analysis procedures.

The simulator is based on the physical modeling of atmospheric turbulence and on experimental data when available, e.g. for the sky background fluctuations and for the sky transmission. Its inputs consist of specifications for the interferometer configuration, target source, observational scenario, atmospheric conditions, and for detector and control loop performance. The outputs are a series of detected photon-electrons (for constructive and destructive interference modes) as a function of time and wavelength, mimicking actual CCD output. GENIEsim can be operated in any infrared atmospheric window, but is more specifically designed for the L' and N bands (respectively centered at 3.8 μm and 10.5 μm), which are the preferred wavelengths for the GENIE instrument (see [Abs02] and chapter 4).

In this thesis, we present the physical effects taken into account in the GENIE simulator and, based on a preliminary design of the instrument, the GENIE subsystems and their expected performance are discussed. First, a brief reminder of the basic equations of nulling interferometry is given in chapter 2. In chapter 3 are described the astronomical sources modeled in the simulator, namely stars, circumstellar disks and giant planets. Then, chapters 4, 5 and 6 discuss in detail the environment of the GENIE instrument, the noise sources it encounters, and possible ways to reduce them by means of control subsystems. Finally, in chapter 7 are presented the results of observation simulations with the GENIE simulator for circumstellar disks and hot Jupiters.

Chapter 2

Basic equations of nulling interferometry

In this section, we briefly present the basic equations of nulling interferometry in the particular case of a Bracewell interferometer (i.e., a two-telescope interferometer). This is the simplest configuration for nulling interferometry, and it is considered as the most probable choice for GENIE [Abs02]. A few other configurations have been discussed in a Technical Report [Abs02], and a more general discussion of aperture configurations for nulling interferometry can be found in [Abs01].

2.1 The interferometer's response

2.1.1 Transmission map

The *transmission map* of a pupil plane interferometer results from the superposition of two patterns:

- the diffraction pattern associated with a single telescope,
- the interference pattern produced at the destructive output of the beam-combiner.

The interference pattern is computed as the superposition of the complex amplitudes of the beams collected by the two telescopes, taking into account the additional π phase shift introduced by the phase-shifting device. The relative phase of the beams is given by the difference of optical paths followed by the two beams before reaching the telescopes. Taking the center of the telescope array as a phase reference, the phases of the two beams in Figure 2.1 are equal to $\pm\pi\frac{b\theta}{\lambda}\cos\phi$. With the notations of Figure 2.1, the expression

of the transmission map for a Bracewell interferometer thus writes (see [Abs01]):

$$\begin{aligned} T(\theta,\phi) &= \frac{1}{2}\left(\frac{2J_1(\pi\theta D/\lambda)}{\pi\theta D/\lambda}\right)^2 \left|\exp\left(j\pi\tfrac{b\theta}{\lambda}\cos\phi\right) - \exp\left(-j\pi\tfrac{b\theta}{\lambda}\cos\phi\right)\right|^2 \\ &= 2\left(\frac{2J_1(\pi\theta D/\lambda)}{\pi\theta D/\lambda}\right)^2 \sin^2\left(\pi\tfrac{b\theta}{\lambda}\cos\phi\right) \end{aligned} \tag{2.1}$$

with J_1 the first order Bessel function. In this expression, the first factor accounts for the diffraction pattern of a single telescope of diameter D, while the second factor is due to the interference between the beams collected by the two telescopes, separated by a distance b called the baseline. Only one half of the total intensity is sent to the destructive output, the other half being sent to the constructive one.

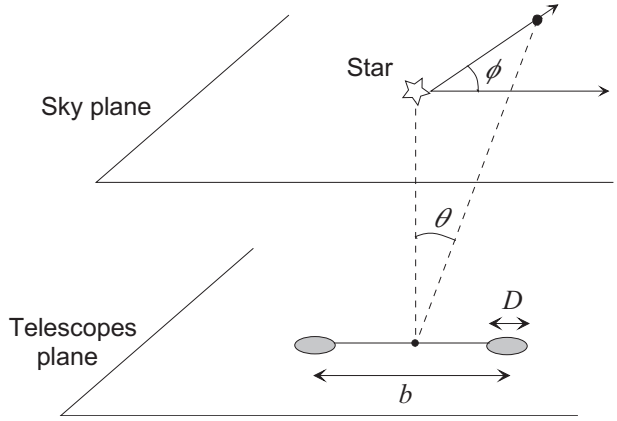

Figure 2.1: Geometrical configuration of the interferometer and of the stellar system. The two angular coordinates (θ, ϕ) denote the position in the sky. In this sketch, the star is assumed to be at zenith.

Using a more general aperture configuration, consisting of n telescopes with diameters D_k, placed at polar coordinates (L_k, δ_k) with respect to the center of the array, and affected by achromatic phase-shifts ϕ_k, the expression of the interference factor of equation (2.1) is given by [Men99]:

$$R(\theta,\phi) = \left|\sum_{k=1}^{n} D_k e^{j2\pi(L_k\theta/\lambda)\cos(\delta_k-\phi)}\, e^{j\phi_k}\right|^2 , \tag{2.2}$$

and is called the *interferometric response* of the array. When divided by the number of outputs of the interferometer, this is also the expression of the transmission map close to the optical axis (where diffraction is negligible).

2.1.2 Field-of-view

As explained in section 4.3.1, GENIE will make use of spatial filtering, most probably in the form of single-mode infrared fibers. The field-of-view (FoV hereafter) of a single-

mode fiber is related to its beam width. The beam width is defined as the product of the beam surface A and of the beam aperture Ω, and is conserved throughout any optical device. The beam width $A\Omega$ of a single-mode fiber is approximately equal to λ^2 [CdF94] and thus approximately matches the size of the central Airy ring of the telescope (even if the Gaussian shape of the fiber acceptance cone does not match the "Bessel shape" of the Airy disk). The beam width being conserved, the FoV can be computed on the sky, at the telescope entrance:

$$\Omega_{\mathrm{FoV}} = \frac{\lambda^2}{A_{\mathrm{tel}}} \Rightarrow \theta_{\mathrm{FoV}} = \frac{\lambda}{\pi R_{\mathrm{tel}}} \,, \tag{2.3}$$

where θ_{FoV} is the FoV angular radius and R_{tel} the telescope radius. Table 2.1 gives the FoV angular radius for typical GENIE configurations, using the VLT Unit Telescopes (UT) or Auxiliary Telescopes (AT). The transmission map of a Bracewell interferometer formed of two UTs within its interferometric FoV is presented in Figure 2.2.

	UT (8 m)	AT (1.8 m)
N band	172 mas	764 mas
L'band	62 mas	277 mas

Table 2.1: Fiber-limited FoV computed from equation (2.3).

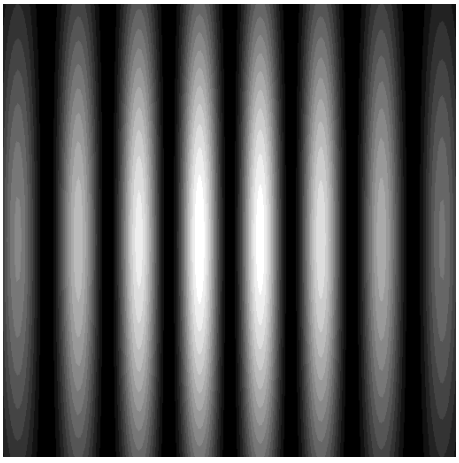

Figure 2.2: Transmission map of a 46 m Bracewell interferometer formed of two UTs. The interferometric field-of-view is respectively of 125 mas and 345 mas at 3.8 μm and 10.5 μm, while the spacing between two successive bright fringes is of 17 mas and 47 mas.

2.1.3 Output of a nulling interferometer

To compute the flux detected at the destructive output of a nulling interferometer, the transmission map is projected onto the sky plane. It determines the regions of the field-of-view that are transmitted and those that are cancelled by the interference process. The output signal of a Bracewell nulling interferometer pointing to a star surrounded by a dust cloud and/or a planet can be expressed as follows:

$$F(t) = A_{\rm tot} \int_\theta \int_\phi \left[T(\theta,\phi,t) \left(B_*(\theta,\phi) + B_{\rm exo}(\theta,\phi) + B_{\rm p}(\theta,\phi) \right) + B_{\rm bckg}(t) \right] \theta {\rm d}\phi {\rm d}\theta \ , \quad (2.4)$$

with $T(\theta,\phi,t)$ the time-dependent transmission map of the interferometer, possibly degraded by random instrumental errors (see section 5.4), and with $B_*(\theta,\phi)$, $B_{\rm exo}(\theta,\phi)$ and $B_{\rm p}(\theta,\phi)$ the brightness of the star, the exozodiacal dust disk and the planet, integrated on the observation waveband $\Delta\lambda$. $B_{\rm bckg}(t)$ is the time-dependent brightness of the incoherent background that includes the thermal emission from the sky, the telescope and from the instrument optics.

2.2 Stellar leakage and rejection rate

For small values of $\pi\theta b/\lambda$, the expression of the transmission map can be simplified by noting that:

$$\begin{aligned} \sin^2\left(\pi\tfrac{b\theta}{\lambda}\cos\phi\right) &\simeq \left(\pi\tfrac{b\theta}{\lambda}\cos\phi\right)^2 \\ \frac{2J_1(\pi\theta D/\lambda)}{\pi\theta D/\lambda} &\simeq 1 \end{aligned}$$

so that the transmission map for small values of the off-axis angle θ is given by:

$$T(\theta,\phi) \simeq 2\pi^2 \frac{b^2\theta^2\cos^2\phi}{\lambda^2} \quad (2.5)$$

The transmission close to the centre of the field-of-view is thus proportional to the square of the off-axis angle θ, and the Bracewell configuration is called a "θ^2 configuration".

Even with an ideal Bracewell interferometer, the stellar signal is only perfectly cancelled on the optical axis. The finite stellar diameter allows for light from the edges of the star to "leak" through the fringe pattern. The amount of *stellar leakage* is given by the integration of the transmission map on the stellar disk:

$$\begin{aligned} F_{\rm leak} &= A_{\rm tel} \int_0^{\theta_*} \int_0^{2\pi} T(\theta,\phi) B_*(\theta,\phi) \theta {\rm d}\phi {\rm d}\theta \\ &\simeq A_{\rm tel} B_* \int_0^{\theta_*} \int_0^{2\pi} 2\pi^2 \frac{b^2\theta^2\cos^2\phi}{\lambda^2} \theta {\rm d}\phi {\rm d}\theta \end{aligned} \quad (2.6)$$

In this relation, the stellar brightness per square meter per steradian B_* is considered as constant over the whole stellar surface, which has an angular radius θ_*. When computing the integral, we end up with

$$F_{\text{leak}} = A_{\text{tel}} B_* \frac{\pi^3 b^2 \theta_*^4}{2\lambda^2} \,. \tag{2.7}$$

In GENIEsim, stellar leakage is computed by performing the double integral of equation (2.6), using the actual transmission map of the interferometer, which takes into account all instrumental imperfections discussed in chapter 5.

We define the *stellar transmission* τ as the ratio between the transmitted stellar flux and the initial stellar flux at the input of the beam-combiner (flux coming from both telescopes)[1]. The total collecting surface $2A_{\text{tel}}$ must be used in this expression because the transmission map takes the number of telescopes into account:

$$\tau = \frac{F_{\text{leak}}}{2A_{\text{tel}} B_* \pi \theta_*^2} = \frac{\pi^2}{4} \left(\frac{b\theta_*}{\lambda} \right)^2 \tag{2.8}$$

The rejection rate ρ is then defined as the inverse of the stellar transmission:

$$\rho = \frac{4}{\pi^2} \left(\frac{\lambda/b}{\theta_*} \right)^2 \tag{2.9}$$

The *rejection ratio* depends on two parameters: the ratio of wavelength to baseline, which sets the angular resolution of the interferometer, and the angular radius of the star θ_*. The rejection ratio decreases for longer baselines (or shorter wavelengths) as the stars gets more and more resolved.

2.2.1 Influence of distance and baseline

The rejection rate ρ depends on the baseline and distance in a quadratic way. In Table 2.2, the rejection ratio for the Sun placed at different distances is given for three different baselines in the K, L' and N bands. This table shows that the K band is not very appropriate to study the circumstellar environment of nearby stars: because of the too high angular resolution, the star is partially resolved and the rejection ratio is quite small, making it difficult to detect dust or planets. On the other hand, the rejection ratio is very large in the N band, because the dark fringe is very broad. However, this can also be a disadvantage if we want to detect a planet very close to its parent star: the planetary signal will be partially cancelled by the central dark fringe.

[1] In the case of a Bracewell interferometer, the stellar transmission is also the ratio of fluxes in destructive and constructive modes, because the stellar signal in constructive mode is approximately equal to the total flux collected by the interferometer.

	K band (2.2 μm)			L' band (3.8 μm)			N band (10.5 μm)		
	25 m	50 m	100 m	25 m	50 m	100 m	25 m	50 m	100 m
Sun@5pc	154	39	9.6	460	115	29	3513	878	219
Sun@10pc	617	154	39	1840	460	115	14055	3513	878
Sun@20pc	2468	617	154	7363	1840	460	56220	14055	3513
Sun@50pc	15425	3856	964	46021	11505	2876	351376	87844	21961

Table 2.2: Rejection ratio for Sun-like stars at a distance of 5, 10, 20 and 50 pc in the K, L' and N bands, using three different baseline lengths (25, 50 and 100 m). The stars are assumed to be at zenith so that the length of the baseline projected onto the sky plane is the same as its physical length.

2.2.2 Influence of spectral type

In Table 2.3 are listed the rejection rates for five different stellar types, all of them located at 10 pc. This table shows that early-type stars cannot be efficiently nulled at a distance of 10 pc. This is not a problem since early-type stars are luminous (and can thus be observed further away), and because anyway early-type stars are not abundant in the close solar neighborhood. On the contrary, due to their small diameter, late-type stars as M dwarfs can be efficiently nulled even at 5 pc, which is good news since M dwarfs are very dim and thus will not be studied further than 10 pc.

	L' band	N band
A0V	74	562
F0V	272	2079
G0V	417	3187
K0V	637	4863
M0V	1160	8853

Table 2.3: Values of rejection rate for stars at 10 pc with different spectral types. A Bracewell configuration with a baseline of 50 m is used. The stars are located at zenith.

Chapter 3

Astronomical sources

Three types of astronomical sources are included in the GENIE simulator. Besides stars, which are currently modeled as blackbodies, circumstellar disks and exoplanets can be used as inputs for the observation simulations. These are the three main targets that will be studied by GENIE: single stars for nulling tests, circumstellar disks and exoplanets to prepare the Darwin science programme.

3.1 The star catalogue

The basic list of target stars for GENIE was compiled from the Gliese star catalogue. The star selection criteria were:

- late spectral type: from late F-, over G- and K- to early M-type stars,
- small distance: within 25 pc,
- good observability from the VLTI: declinations between $+20°$ and $-70°$.

All in all, this list contains 121 F stars, 193 G stars, 406 K stars and 353 M stars. Several other compiled lists can be used in GENIEsim for targets observable from Cerro Paranal, sorted by decreasing K magnitude. Currently available are:

- a list of G, K and M stars for GENIE from the DARWIN target catalogue,
- a list of all stars with detected planets via radial velocity search,
- a list of main sequence stars with known debris disks,
- a list of Young Stellar Objects with known disks.

These lists include values for the temperature, luminosity, radius and mass of the star according to their sub-stellar class using a linear interpolation model and their estimated K, L, L' magnitude, the real K magnitude measurements if available, estimates of the extent of the habitable zone and the radial extent of the stellar disk. Besides these lists, the

user is free to specify any other target of interest for GENIE. More sophisticated stellar models will be soon available, e.g. based on the Kurucz model atmospheres [Kur79].

3.2 The DISKPIC package

In the DISKPIC package, we have implemented a simple model for optically thin disks. This model is based on a morphological description of the dust disk: the physical processes leading to the given morphology are not modeled. A simple model such as DISKPIC is very handy in a science simulator, because it uses a short list of explicit parameters such as luminosity, inner and outer radius, density and temperature power-laws, whose influence on the detected flux can be studied independently.

3.2.1 Basic assumptions

DISKPIC is supposed to be very general, in order to simulate as many types of disks as possible. The following assumptions are necessary to keep the simulation code rather simple, but do not prevent it from simulating dust disks in a realistic way.

- *Dust properties independent of vertical position*: the properties of the dust grains at any place (r_c, φ_c, z_c) in the cloud are the same as at the position (r_c, φ_c, 0) in the ecliptic plane of the dust cloud (we assume that the ecliptic plane is equivalent to the invariant Laplace plane). This assumption is valid if the thickness of the cloud is much smaller than its radius.

- *Dust properties independent of azimuth*: we assume that the disk is azimuthally symmetric.

- *Optically thin cloud*: we assume that there is no screening effect between dust grains. The observer therefore sees the emission from every single dust grain located within the field-of-view.

- *Only thermal emission*: we do not take the scattered light into account.

These assumptions make DISKPIC very well suited for the simulation of debris disks and exozodiacal disks because they are optically thin, generally flat and symmetric. DISKPIC is not designed to simulate circumstellar disks around Young Stellar Objects (YSO), which are optically thick. In addition, the presence of gas and the vertical dependence of the dust properties make these disks much more complicated than debris disks, so that YSO disks require specific physical codes for a realistic simulation. Such codes should be implemented in GENIEsim in a few months. Meanwhile, DISKPIC can still be used to simulate face-on YSO disks with a user-specified spectrum.

3.2.2 Morphology of the dust cloud

3.2.2.1 Geometry of the cloud

The geometry of the cloud is defined by the inner and outer radii ($r_{\rm in}$ and $r_{\rm out}$), by the inner height $h_{\rm in}$ and by the flaring parameter f (see Figure 3.1). The flaring parameter allows for a linear or exponential flaring of the disk. The vertical thickness of the cloud is given by:

$$h(r_c) = h_{\rm in}\,(r_c/r_{\rm in})^f \tag{3.1}$$

Setting f to 1 produces a linearly flared cloud, while setting f to 0 produces a flat disk of vertical thickness $h_{\rm in}$. Flaring is very rare for debris disks (β Pic is the only known example), while YSO disks have a default flaring parameter of 9/8 [KH87].

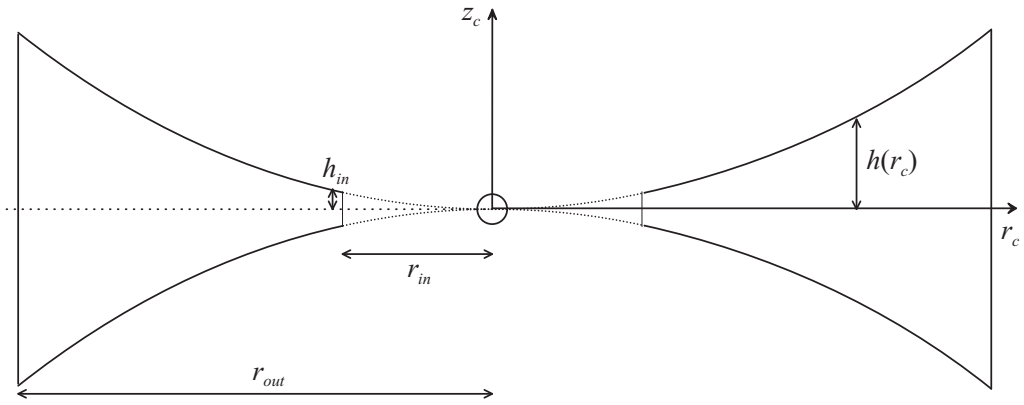

Figure 3.1: Basic parameters for the cloud morphology.

3.2.2.2 Orientation of the cloud

In the following developments, the sky coordinates are denoted (x,y,z), with the z axis towards the observer and the x axis towards the South Celestial Pole (see Figure 3.2). The cloud coordinates are denoted (x_c,y_c,z_c). The orientation of the dust cloud, or more precisely the orientation of its ecliptic plane, is defined by the inclination i with respect to the sky plane and by the position angle p. The position angle is the angle between the South Celestial Pole and the line of nodes of the dust cloud, the line of nodes being the intersection between the ecliptic plane and the sky plane. In DISKPIC, the inclination will always be reduced to a value between 0° and 90°, while the position angle can take any value between 0° and 360°.

3.2.2.3 Density and temperature power-laws

The number density for the dust grains is described by a power-law:

$$N(r_c) = N_0\,(r_c/r_{\rm in})^{-\alpha} \tag{3.2}$$

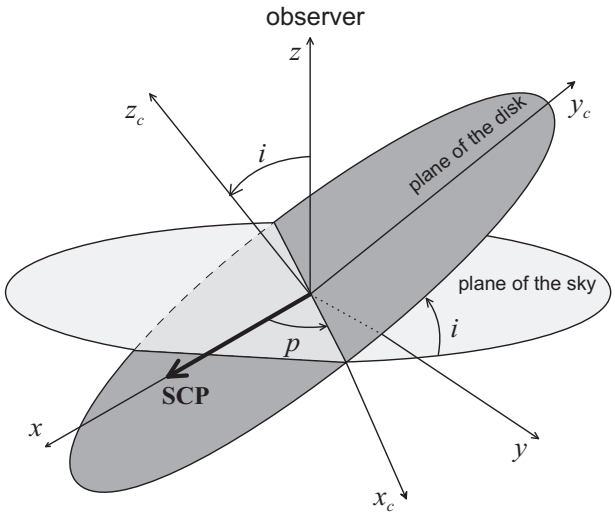

Figure 3.2: The orientation of the dust cloud is defined by the two angles i and p.

valid for $r_c > r_{\rm in}$, and with N_0 the number density at the inner radius, expressed in m^{-3}. In the following developments, we will assume that the dust grains are all of the same size, or at least that the size distribution is independent of the distance to the star (i.e., independent of r). The cross-sectional area of dust grains per unit volume can then be written as:

$$\Sigma(r_c) = \Sigma_0 \left(r_c/r_{\rm in}\right)^{-\alpha} \tag{3.3}$$

with $\Sigma_0 = \pi a^2 N_0$ in m^{-1} the cross-sectional area per unit volume at the inner cut-off, where a is the mean radius of the dust grains. We also allow for a smooth density decrease within the dust inner radius:

$$N(r_c) = N_0 \left(r_c/r_{\rm in}\right)^{\alpha_2} \tag{3.4}$$

valid for $r_* < r_c < r_{\rm in}$. The DISKPIC routine only uses positive values of α_2 to prevent density from being infinite at $r_c = 0$. If α_2 is set to a negative value by the user, a sharp cut-off will be produced (as if $\alpha_2 = \infty$) instead of letting $N(r_c)$ increase inside $r_{\rm in}$. In that case, $N(r_c) = 0$ for $r_c < r_{\rm in}$. In practice, it is not clear if α_2 has a real physical meaning and is essentially used for testing purpose. It can also be used to simulate two-component disks, such as expected for β Pic.

The temperature also follows a power-law:

$$T(r_c) = T_{\rm in} \left(r_c/r_{\rm in}\right)^{-\delta} \tag{3.5}$$

with $\delta = 0.5$ as default, relevant for an optically thin cloud with blackbody grains.

3.2.2.4 Inner radius and inner temperature

In order to specify the inner radius $r_{\rm in}$ and the temperature $T_{\rm in}$ at the inner cut-off, the user has four possibilities. In the input parameters, one can set:

- $r_{\rm in}$ and $T_{\rm in}$: the temperature power-law is fully determined,
- only $r_{\rm in}$: the inner temperature is computed from the radiative equilibrium between the stellar flux absorbed by the grains and their thermal emission:

$$\begin{aligned} F_{\rm abs} = F_{\rm emit} &\Rightarrow \pi a^2 \frac{4\pi r_*^2 \sigma T_*^4}{4\pi r_{\rm in}^2} = 4\pi a^2 \sigma T_{\rm in}^4 \\ &\Rightarrow T_{\rm in} = \frac{1}{\sqrt{2}} T_* \left(r_*/r_{\rm in}\right)^{0.5} \end{aligned} \tag{3.6}$$

  If $T_{\rm in}$ is greater than the sublimation temperature $T_{\rm subl}$, we let $T_{\rm in} = T_{\rm subl}$ and $r_{\rm in}$ is computed as in equation (3.8).

- only $T_{\rm in}$: the inner radius is computed from the stellar parameters, as the location where the equilibrium temperature is equal to $T_{\rm in}$. From equation (3.6), we get:

$$r_{\rm in} = \frac{r_*}{2} \left(T_*/T_{\rm in}\right)^2 \tag{3.7}$$

  If set by the user, the parameter $T_{\rm in}$ supersedes $T_{\rm subl}$. The inner radius can thus be inside the sublimation radius if $T_{\rm in}$ is set.

- neither $r_{\rm in}$ nor $T_{\rm in}$: the inner temperature is set to the sublimation temperature, and the inner radius is given by:

$$r_{\rm in} = \frac{r_*}{2} \left(T_*/T_{\rm subl}\right)^2 \tag{3.8}$$

In these expressions, r_*, T_* and L_* are respectively the stellar radius, effective temperature and luminosity. The default sublimation temperature $T_{\rm subl}$ is 1500 K. If $r_{\rm in}$ is less than r_*, we let $r_{\rm in} = r_*$ and $T_{\rm in} = T_*$. We assume that there is no dust for $r_c < r_*$, whatever the input parameters.

3.2.3 Dust cross-sectional area

To compute the flux of the dust cloud at the relevant wavelength, the only observational data is generally the fractional luminosity $L_{\rm d}/L_*$, where $L_{\rm d}$ and L_* are the bolometric luminosities of the dust disk and of the star. The stellar properties are also supposed to be known (radius r_*, temperature T_*, luminosity L_* and distance d). In the following paragraph, we show how the flux of the disk can be computed at a given wavelength from these informations and from the cloud morphology.

3.2.3.1 Mean cross-sectional area

Assuming that the dust grains emit like blackbodies, the luminosity of the dust cloud writes:

$$L_{\rm d} = \int_{S_{\rm d}} \int_{2\pi} \int_0^\infty B_\nu \left(T\left(r_c\right)\right) {\rm d}\nu \, {\rm d}\Omega \, \cos\theta \, {\rm d}S \, , \tag{3.9}$$

where S_d is the total surface of the dust, taking all individual grains into account, and where θ is the angle between the elementary solid angle and the perpendicular to the elementary surface (see Figure 3.3). The integral on the solid angle is limited to 2π instead of 4π because each elementary surface only emits in the half space above itself. The expression of the Planck function $B_\nu(T)$ in W/m^2/Hz/sr is the following:

$$B_\nu(T) = \frac{2h\nu^3}{c^2}\left(\exp\left(\frac{h\nu}{kT}\right) - 1\right)^{-1} \tag{3.10}$$

Instead of W/m^2/Hz/sr, we will generally use Jy/sr, with the Jansky (Jy) defined as 10^{-26} W/m^2/Hz. By integrating the Planck function over the whole spectrum and solid angle, we obtain the Stefan-Boltzmann law for the blackbody emission, expressed in W/m^2:

$$\begin{aligned} E(T) &= \int_{2\pi}\int_0^\infty B_\nu(T)\cos\theta\,\mathrm{d}\nu\,\mathrm{d}\Omega \\ &= \sigma T^4 \end{aligned} \tag{3.11}$$

with $\sigma = 5.670 \times 10^{-8}$ W/m^2/K^4 the Stefan-Boltzmann constant. In DISKPIC, all distances are expressed in AU, so that we will use $\sigma_\mathrm{AU} = 1.269 \times 10^{15}$ W/AU^2/K^4 and $E(T)$ in W/AU^2.

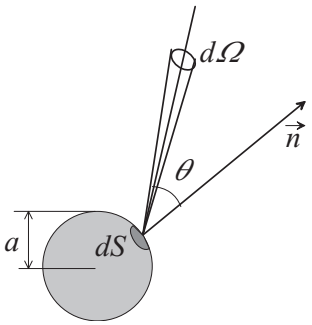

Figure 3.3: The bolometric luminosity of a single dust grain is computed by integrating the Planck function for thermal emission over its surface, all possible emission directions and over the whole spectrum.

The integral on the surface of the dust will be computed in two steps. Let us first compute the luminosity of one dust grain:

$$L_\mathrm{grain} = \int_{S_\mathrm{grain}} \sigma_\mathrm{AU} T_\mathrm{grain}^4 \mathrm{d}S = 4\pi a^2 \sigma_\mathrm{AU} T_\mathrm{grain}^4 \tag{3.12}$$

Then, the luminosity of the whole dust cloud is obtained by integrating the elementary

luminosity of the dust grains in the whole cloud volume $V_{\rm cloud}$:

$$\begin{aligned}
L_{\rm d} &= \int_{V_{\rm cloud}} N(r_c) L_{\rm grain}(r_c) {\rm d}V \\
&= 4\pi a^2 \int_{V_{\rm cloud}} N(r_c) \sigma_{\rm AU} T(r_c)^4 {\rm d}V \\
&= 4\pi a^2 \sigma_{\rm AU} T_{\rm in}^4 \int_0^{2\pi} \int_{r_*}^{r_{\rm out}} \int_{-h_{\rm in}(r/r_{\rm in})^f}^{h_{\rm in}(r/r_{\rm in})^f} N(r_c) \left(r_c/r_{\rm in}\right)^{-4\delta} {\rm d}z \; r_c \; {\rm d}r_c {\rm d}\varphi \\
&= 4\pi a^2 \sigma_{\rm AU} T_{\rm in}^4 \int_0^{2\pi} \int_{r_*}^{r_{\rm out}} 2h_{\rm in} \left(r_c/r_{\rm in}\right)^f N(r_c) \left(r_c/r_{\rm in}\right)^{-4\delta} r_c \, {\rm d}r_c {\rm d}\varphi \\
&= 16\pi^2 a^2 N_0 \sigma_{\rm AU} T_{\rm in}^4 h_{\rm in} \left(\int_{r_*}^{r_{\rm in}} \left(r_c/r_{\rm in}\right)^{f+\alpha_2-4\delta} r_c {\rm d}r_c + \int_{r_{\rm in}}^{r_{\rm out}} \left(r_c/r_{\rm in}\right)^{f-\alpha-4\delta} r_c {\rm d}r_c \right)
\end{aligned}$$

If α_2 is set to a negative value in the default file, the first integral is not computed (no dust within the inner radius). From this expression, we infer the cross-sectional area of dust per unit volume at the inner cut-off radius:

$$\Sigma_0 = \frac{\left(L_{\rm d}/L_*\right) L_*}{16\pi\sigma_{\rm AU} T_{\rm in}^4 h_{\rm in} \left(\int_{r_*}^{r_{\rm in}} \left(r_c/r_{\rm in}\right)^{f+\alpha_2-4\delta} r_c {\rm d}r_c + \int_{r_{\rm in}}^{r_{\rm out}} \left(r_c/r_{\rm in}\right)^{f-\alpha-4\delta} r_c {\rm d}r_c \right)} \tag{3.13}$$

All the parameters in the right-hand side must be specified by the user among the input parameters. The value of Σ_0 will be expressed in 1/AU. If $\alpha_2 = \infty$, the first integral drops.

3.2.3.2 Wavelength dependence

In DISKPIC, we can account for a wavelength-dependence of the dust emissivity. This is done by multiplying the cross-sectional area by a "normalized spectrum". The normalized spectrum is user-specified in a separate ASCII file (such as `specdisk_N.txt`). Using this spectrum, one can also take into account the mean size of the dust particles. From the grain size a, we can define a critical wavelength $\lambda_0 \sim a$. According to [DWHG00], the dust grains emit like blackbodies for $\lambda < \lambda_0$, while the emissivity is proportional to $(\lambda/\lambda_0)^\beta$ for $\lambda > \lambda_0$. The exponent β is called the opacity index.

3.2.4 Flux of the whole dust cloud

The flux produced by a single dust grain in the direction of the observer is given by:

$$\begin{aligned}
F_{\nu,{\rm grain}} &= \frac{1}{d^2} \int_{S_{\rm grain}} B_\nu \left(T_{\rm grain}\right) \cos\theta \, {\rm d}S \\
&= \frac{\pi a^2}{d^2} B_\nu \left(T_{\rm grain}\right)
\end{aligned} \tag{3.14}$$

The flux emitted by the whole dust disk, expressed in Jy, is thus given by:

$$\begin{aligned} F_\nu &= \int_{V_{\rm cloud}} N(r_c)\frac{\pi a^2}{d^2} B_\nu\left(T\left(r_c\right)\right) \mathrm{d}V \\ &= \frac{1}{d^2}\int_0^{2\pi}\int_{r_*}^{r_{\rm out}}\int_{-h_{\rm in}(r/r_{\rm in})^f}^{h_{\rm in}(r/r_{\rm in})^f} \Sigma(r_c) B_\nu\left(T\left(r_c\right)\right) \mathrm{d}z\, r_c\, \mathrm{d}r_c \mathrm{d}\varphi \\ &= 4\pi h_{\rm in}\frac{\Sigma_0}{d^2}\left(\int_{r_*}^{r_{\rm in}} \left(r_c/r_{\rm in}\right)^{f+\alpha_2} B_\nu(T(r_c)) r_c\, \mathrm{d}r_c + \int_{r_{\rm in}}^{r_{\rm out}} \left(r_c/r_{\rm in}\right)^{f-\alpha} B_\nu(T(r_c)) r_c \mathrm{d}r_c\right) \end{aligned}$$

3.2.5 Image of the dust cloud in the GENIE field-of-view

Now that the total flux of the cloud within the FoV is known, we have to produce its image, digitalized over a given number of pixels. The image of the dust cloud will be produced by integrating the flux emitted by the dust particles located along the lines-of-sight crossing the center of each pixel. Note that the small FoV of the GENIE instrument will generally not allow to include the whole cloud.

3.2.5.1 Digitalization of the field-of-view

In order to get a regular digitalization of the FoV, we will use the Cartesian coordinates (x,y) in the plane of the sky. The image of the dust cloud will be computed on a $P \times P$ matrix where P is the number of pixels along one direction. The linear size of the pixels is noted $(\Delta x, \Delta y)$, and is expressed in AU.

The flux from an exozodiacal cloud mainly comes from the central part of the cloud, where the dust density and temperature are larger. For example, in the case of our local zodiacal cloud, less than 10% of the flux comes from the region outside 1 AU (see Figure 3.8). Since 1 AU corresponds to 100 mas around a star at 10 pc, the FoV of a single mode fiber at the focus of a large telescope, defined in section 2.1.2, is well adapted to detect a large part of the exozodiacal emission.

There are three critical points when choosing the number and size of the pixels:

1. *Vertical thickness*: In order to simulate a flat disk, the user must specify its vertical thickness. If the cloud is seen edge-on, this choice can influence the result of the simulation: if the thickness is too small, it can happen that no pixel has its center within the dust cloud. In that case, DISKPIC produces an empty image. The disk thickness should therefore not be smaller than the pixel size. On the other hand, the disk should not be too thick, so that the vertical dependence of temperature and density can actually be neglected. In practice, a thickness of about 0.1 AU is recommended for flat disks at a distance of 10 pc, unless another value is available in the literature.

2. *Number of pixels*: In order to compute the dust emission with a sufficient precision, a sufficiently large number of pixels must be used. A good sampling of the dust

emission is particularly important near the inner cut-off, especially when the inner cut-off lies close to the star (the temperature and density gradients are particularly high close to the star). In general, 128 pixels across each direction is sufficient for a good sampling of the dust cloud. When the inner cut-off is very close to the star, or when the target star is further than 100 pc, the user must ensure that the sampling is adequate. This can be done by comparing the analytical value for the flux of the whole disk returned by DISKPIC (by integration of the whole dust emission in the cloud coordinates) and the flux in the disk image (also computed by DISKPIC, by integration along the lines-of-sight). A large difference between these two values is symptomatic of an insufficient sampling. The default sampling for DISKPIC is 128×128, while ZODIPIC uses 144×144 as default. In DISKPIC, any number of pixels can be used, while in ZODIPIC it must be a multiple of 16.

3. *Field-of-view*: A good sampling of the exozodiacal cloud requires about 128 pixels along the two directions of the exozodi image (total number of pixels: 16384). In order to efficiently use these pixels, the total size of the exozodi image produced by DISKPIC must be equal to the FoV defined by the fiber. Table 3.1 gives the pixel sizes to meet this requirement.

	UT (8m)	AT (1.8 m)
N band	2.61 mas	11.6 mas
L' band	0.97 mas	4.33 mas

Table 3.1: Pixel sizes in the exozodi image to match the FoV defined by the single-mode fiber (128 pixels are used across each direction).

For example, we have simulated the disk around zeta Leporis, a Vega-type star located at 21 pc (see chapter 7). We have used an edge-on disk with a semi-thickness $h_{\rm in}$ of 0.1 AU (i.e., 10 milli-arcsec for the total thickness). The FoV defined by the fiber is 345 mas in diameter. With 128×128 pixels, the pixel size is about 2.7 mas, and so there are only four pixels to sample the total disk thickness. DISKPIC returns a total flux within the FoV of 286 mJy. With 256×256 pixels (of 1.35 mas each) the computed flux is of 216 mJy. With 512×512 pixels (of 0.67 mas each), we get 251 mJy and with 1024×1024 pixels we also get 251 mJy. This shows that at least 512×512 pixels are needed: with a lower sampling, the flux contained in the disk image depends on the pixel size. *The pixel size should therefore be at least 5 times smaller than $h_{\rm in}$ when simulating an edge-on disk.*

3.2.5.2 Change of variables

To perform the integration along the lines-of-sight in the sky coordinates (x, y, z), we have to express the cloud coordinates (x_c, y_c, z_c) as a function of the sky coordinates. The

cloud coordinates can be derived from the sky coordinates by applying first a rotation of angle i (inclination) around the axis x, and then a rotation of angle p (position angle) around the axis z (see Figure 3.2). The relationships between the two coordinate systems write:

$$\begin{cases} x_c = x\cos p + y\sin p \\ y_c = (-x\sin p + y\cos p)\cos i + z\sin i \\ z_c = (x\sin p - y\cos p)\sin i + z\cos i \end{cases} \tag{3.15}$$

3.2.5.3 Disk image

The disk image consists of a matrix filled with the individual pixel fluxes. In order to compute the flux in each pixel, we have to integrate the flux along the line-of-sight for each pixel. The flux function $\Phi(x,y,z)$ to be integrated is the blackbody function at the temperature of the current point multiplied by the density at the current point. It writes:

$$\begin{aligned} \Phi(x,y,z) &= \frac{\pi a^2}{d^2} B_\nu(T(x,y,z))N(x,y,z) \\ &= \frac{1}{d^2} B_\nu(T(x,y,z))\Sigma(x,y,z) \end{aligned} \tag{3.16}$$

The integral to be computed for each pixel (x,y) belonging to the FoV is the following:

$$\begin{aligned} \text{Image}(x,y) &= \frac{1}{d^2}\int_{x-\Delta x/2}^{x+\Delta x/2}\int_{y-\Delta y/2}^{y+\Delta y/2}\int_{z_1}^{z_2} B_\nu(T(x,y,z))\Sigma(x,y,z)\mathrm{d}z\mathrm{d}y\mathrm{d}x \\ &\simeq \frac{\Delta x\Delta y}{d^2}\int_{z_1}^{z_2} B_\nu(T(x,y,z))\Sigma(x,y,z)\mathrm{d}z \end{aligned} \tag{3.17}$$

where Δx and Δy are the linear dimensions of a pixel in AU. This expression assumes that there is no variation of density or temperature within an elementary surface $(\Delta x, \Delta y)$ in the cloud, and that there is no screening effect between the grains (thin disk). The size of the pixels must be small enough in order to validate the former assumption. Note that we need to compute the cloud image only in one half of the FoV since the cloud is symmetric.

3.2.5.4 Integration boundaries

The major problem encountered when evaluating the previous integral is the determination of the integration limits (z_1,z_2) along the line-of-sight. The outer radius of the disk gives a first guess of the integration limits. To obtain this first estimate, we have to solve the following equation:

$$r_c(x,y,z) = r_{\text{out}} \tag{3.18}$$

with respect to z, taking x and y as parameters. Replacing $r_c(x, y, z)$ by its expression, we get:

$$\begin{aligned} & (x\cos p + y\cos p)^2 + ((-x\sin p + y\cos p)\cos i + z\sin i)^2 = r_{\text{out}}^2 \\ \Rightarrow \quad & z_{2,1} = \frac{(-x\sin p + y\cos p)\cos i}{\sin i} \pm \frac{\sqrt{r_{\text{out}}^2 - (x\cos p + y\sin p)^2}}{\sin i} \end{aligned} \tag{3.19}$$

with $z_2 \geq z_1$. In the case of a face-on disk ($i = 0$), this equation does not hold, but the integration limits can be computed directly by using the following equation:

$$z_{2,1} = \pm h_{\text{in}}(r_c(x, y)/r_{\text{in}})^f \ . \tag{3.20}$$

These are the actual values of z_2 and z_1, limited by the cloud thickness, and the following step can be skipped in this case.

Let us now compute the actual integration limits in the case where $i \neq 0$. We have to take the thickness of the cloud into account, defined by:

$$z_c(x, y, z) = \pm h_{\text{in}}(r_c(x, y, z)/r_{\text{in}})^f \tag{3.21}$$

There are three cases to be considered, depending on the values of $z_{c1} = z_c(x, y, z_1)$ and $z_{c2} = z_c(x, y, z_2)$, which are the vertical coordinates of the preliminary estimates in the cloud coordinates. These values have to be compared with the thickness of the cloud at the outer radius:

$$z_{c,\max} = h_{\text{in}}(r_{\text{out}}/r_{\text{in}})^f \tag{3.22}$$

1. If $z_{c2} > z_{c,\max}$
   This case is illustrated on the left-hand side of Figure 3.4. When $z_{c2} > z_{c,\max}$, there are three cases to consider depending on the value of z_{c1}.

   - If $z_{c1} > z_{c,\max}$: the line-of-sight is empty, and the flux is zero in that pixel.
   - If $-z_{c,\max} < z_{c1} < z_{c,\max}$: the lower boundary of the cloud is z_1, but the upper boundary z_2 has to be re-computed by solving the equation:

     $$z_c(x, y, z_2) = h_{\text{in}}(r_c(x, y, z_2)/r_{\text{in}})^f$$

   - If $z_{c1} < -z_{c,\max}$: neither z_1 nor z_2 are the actual boundaries of the dust cloud. They are computed by solving the following equations for z_1 and z_2:

     $$\begin{aligned} z_c(x, y, z_1) &= -h_{\text{in}}(r_c(x, y, z_1)/r_{\text{in}})^f \\ z_c(x, y, z_2) &= h_{\text{in}}(r_c(x, y, z_2)/r_{\text{in}})^f \end{aligned}$$

2. If $-z_{c,\max} < z_{c2} < z_{c,\max}$
   This case is illustrated in the middle of Figure 3.4. When $-z_{c,\max} < z_{c2} < z_{c,\max}$, there are two cases to consider depending on the value of z_{c1}.

- If $-z_{c,\max} < z_{c1} < z_{c,\max}$: both the lower and upper boundaries are already the good ones. But we have to take into account the fact that all points between z_1 and z_2 are not necessarily inside the dust cloud. This will be done by including only the points that have $|z_c| < h(r_c)$ in the integral.
- If $z_{c1} < -z_{c,\max}$: the upper boundary of the dust cloud is z_2, but z_1 is not its lower boundary. It must be computed by solving the following equation for z_1:

$$z_c(x, y, z) = -h_{\rm in}(r_c(x, y, z_1)/r_{\rm in})^f$$

3. If $z_{c2} < -z_{c,\max}$
   In that case, the line-of-sight is empty and the flux associated with that pixel is zero, as shown on the right-hand side of Figure 3.4.

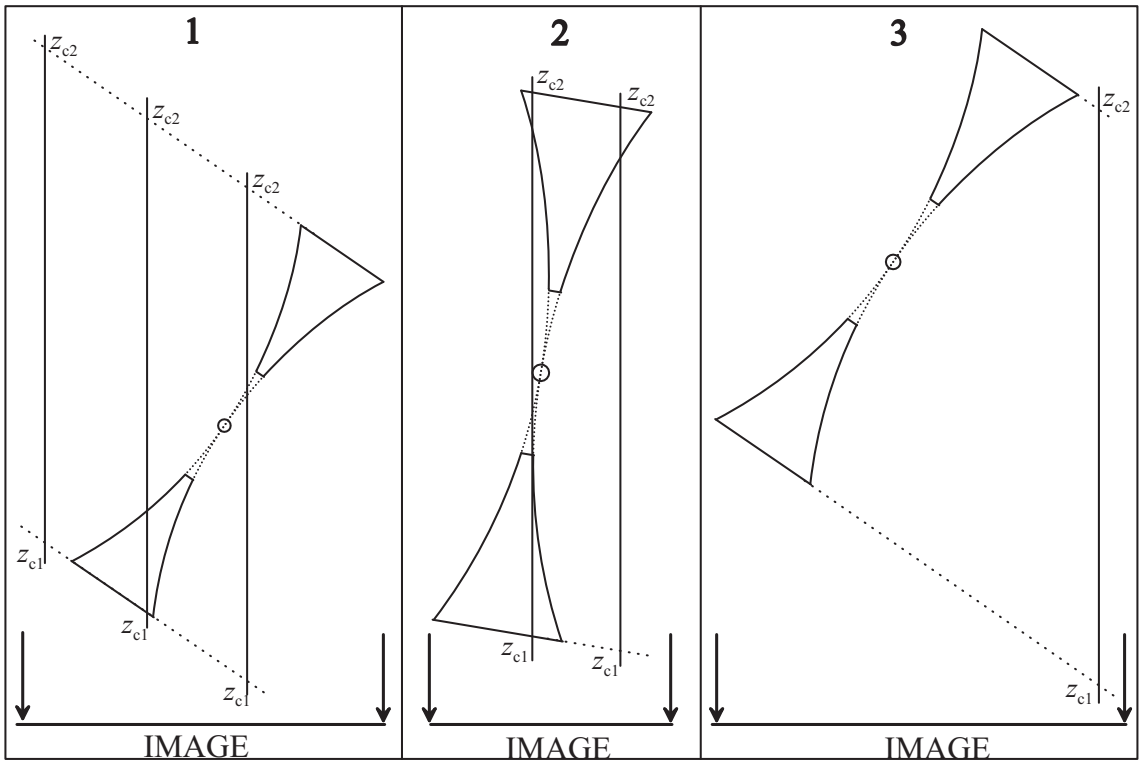

Figure 3.4: (1) If $z_{c2} > z_{c,\max}$, there are three cases to consider depending on the value of z_{c1}. (2) If $-z_{c,\max} < z_{c2} < z_{c,\max}$, there are two cases to consider depending on the value of z_{c1}. (3) If $z_{c2} < -z_{c,\max}$, the line-of-sight is empty.

3.2.6 Examples of circumstellar disks

3.2.6.1 Zodiacal disk

The modeling of the zodiacal disk with a flat disk is not an easy task, because of the complex morphology of the zodiacal disk. We will not try to reproduce the complicated vertical dependence of the dust density (the ZODIPIC package already does that). The following parameters can be used to simulate the solar zodiacal disk. They are taken from [KWF+98], and are based on COBE/DIRBE observations:

- Fractional dust luminosity: 5×10^{-7}
- Density power-law exponent: -1.34
- Temperature power-law exponent: -0.467
- Inner radius: determined by dust sublimation (just let $r_{\text{in}} = 0$ in the input parameters)
- Outer radius: 3.28 AU (where the asteroid belt stops – 2:3 resonance with Jupiter)
- Sublimation temperature: 1500 K
- Flat disk (flaring parameter: 0)
- Expected N-band excess for a solar system at 10 pc: 0.1 mJy

3.2.6.2 Debris disk (Vega-type star)

Debris disks are mostly flat disks, with density exponents in the range -0.5 to -1. The disk being optically thin, the grains are in radiative equilibrium, so that the temperature power-law is in $r^{-0.5}$. The fractional luminosity is generally smaller than 10^{-3}. Warm dust around main sequence stars has been observed only in very few cases, maybe because it is not present, or because near-IR photometry is not precise enough to reveal small near-IR excesses against the large photosphere flux (the flux ratio is generally larger than 1000 in the near-infrared).

Fajardo-Acosta et al. [FATK98] present five main-sequence stars around which warm dust has been detected. We have tried to simulate one of them, zeta Leporis, an A2V at 21.52 pc. The stellar parameters are the following:

- Radius: 1.7 $R_\odot$
- Effective temperature: 8500 K
- Luminosity: 14 $L_\odot$

The disk parameters are the following:

- Fractional dust luminosity: $1.7\times\ 10^{-4}$
- Density power-law exponent: -0.6
- Temperature power-law exponent: -0.5
- Inner radius: 0.5 AU
- Outer radius (encompassing 90% of the flux): 7 AU
- Inner temperature: 960 K
- Flat disk (flaring parameter: 0)
- Inclination: unknown
- Observed N-band excess: 0.43 Jy

Using these parameters in DISKPIC, we have produced the Spectral Energy Distribution (SED) of the ζ Lep system (star and dust disk, see Figure 3.5) and compared it with the observed SED. Our simulated SED matches the observed one quite well till $\sim$20 μm. The flux contained in the disk image in the N band is 0.46 Jy, in agreement with the the excess observed by Fajardo-Acosta (0.43 Jy).

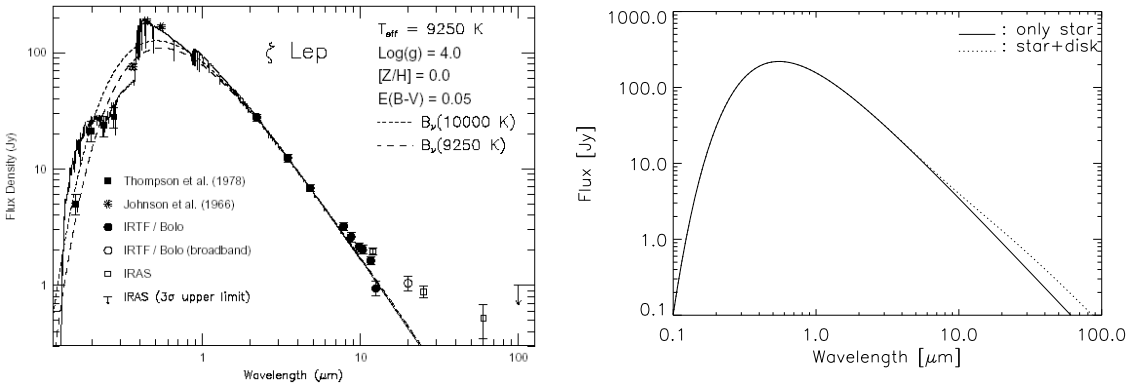

Figure 3.5: SED of the zeta Leporis system. Left: data from Fajardo-Acosta [FATK98]. Right: SED obtained with DISKPIC. The far-IR excess is not well reproduced by DISKPIC because the model only takes warm dust into account (the cloud has been truncated at 7 AU).

The image of the dust cloud within a UT interferometric field-of-view (172 mas in radius) is given in Figure 3.6. At a distance of 21.52 pc, an angle of 172 mas corresponds to 3.7 AU). Thus, the FoV is not large enough to include the whole dust disk.

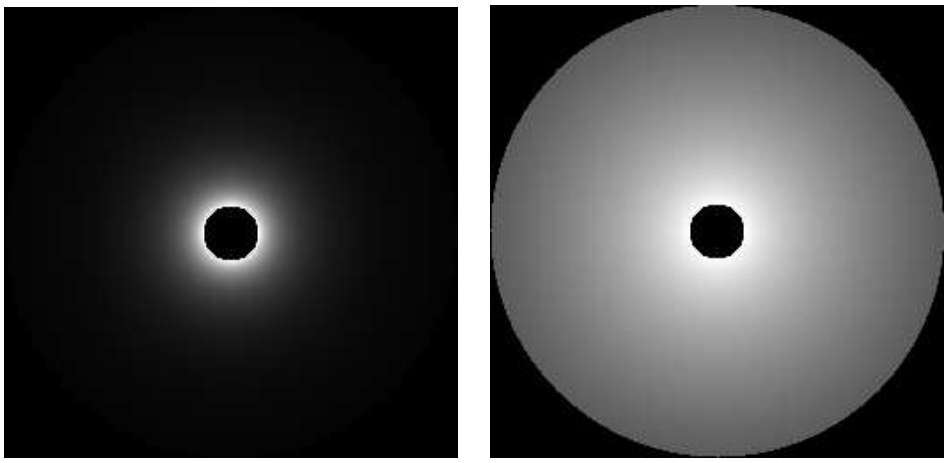

Figure 3.6: Image of the dust cloud within a UT interferometric FoV (172 mas). Left: linear scale. Right: logarithmic scale.

3.2.6.3 Young Stellar Objects

There are currently different models that account for the excess IR emission of Young Stellar Objects (YSO) [MGST01]. The answers to many questions on their evolutionary status and on the origin of their activity and variability depend critically on the relative importance of circumstellar distribution of material in disks or envelopes at different spatial scales. Observations with GENIE will enable us to investigate the properties of the inner region of circumstellar disks which are responsible for the near-infrared excess flux. The expected structure of YSO disks is much more complicated than what can be simulated with DISKPIC: the optically thickness and the presence of gas in YSO disks make the assumptions of section 3.2.1 inappropriate for these disks. However, YSO disks can still be simulated with DISKPIC under special conditions:

- the disk must be face-on in order to avoid screening effects and to reduce the effect of the vertical dependence of density and temperature,
- the temperature power-law for the surface layer of the disk must be known,

Under these conditions, DISKPIC can be used to simulate the surface brightness of YSO disks, using a user-specified Spectral Energy Distribution (SED).

T Tauri stars T Tauri stars are low-mass pre-main sequence stars ($< 2M_{\odot}$), observed near many molecular clouds in our galaxy. Roughly half of T Tauri stars have been shown to be surrounded by a disk of dust and gas, detected through IR and sub-millimeter excess emission. Standard blackbody disk models cannot reproduce the infrared and sub-millimeter SED of T Tauri disks. Kenyon and Hartmann [KH87] have analyzed these SEDs, and conclude that much of the infrared excess emission arises from reprocessing

of stellar radiation by the circumstellar dust. The contribution of accretion is shown to be negligible. These authors have also suggested that the disk tends to "flare", i.e., to have a concave upper surface so that they intercept a larger percentage of the stellar radiation. The classical parameters for a T Tauri disk are the following (see [KH87]):

- Density power law in $r^{-1.5}$ (C. Eiroa, personal communication)
- Temperature power-law in $r^{-3/4}$
- Flaring parameter $f = 9/8$
- Sublimation temperature of 1500 K
- Disk luminosity $\sim$ 0.25 to 0.5 L_*
- Typical disk size: 100 AU
- Typical target distance: 150 pc (nearest star-forming regions: Taurus and Ophiuchus)

Herbig Ae/Be stars Herbig Ae/Be (HAeBe) stars [Her60] are young stellar objects with intermediate-mass (2-10 $M_\odot$) that show broad emission lines, rapid variability, and excess infrared and millimeter-wavelength emission. These properties are consistent with the presence of hot and cold circumstellar dust and gas. These systems are simultaneously high-mass analogs of the approximately solar-mass T Tauri stars and the evolutionary precursors of the prototypical main-sequence debris-disk sources β Pic, α Lyr, and α PsA. While there is still some debate about the morphology of the circumstellar material, most observations supports the hypothesis that in many cases the dust and gas lie in a massive ($\sim$0.01 $M_\odot$) circumstellar disk [NPN$^+$01]. Direct imaging with millimeter interferometry shows strong evidence for circumstellar disks around HAeBe stars. Flattened structures around several sources have been resolved on $\sim$100 AU scales [MS97], while Hα spectro-polarimetric observations found signatures of flattened circumstellar structures around 83% of their sample and evidence for rotation around nine HAeBe stars [VDHO02].

The disks around Herbig Ae/Be stars are supposed to have essentially the same structure as disks around T Tauri stars. Only the outer radius changes: values between 300 and 800 AU should be considered (C. Eiroa, personal communication).

3.3 The ZODIPIC package

ZODIPIC is an IDL package developed by Marc Kuchner (see [KS01]). It evaluates the empirical model of the solar zodiacal cloud that Kelsall et al. [KWF$^+$98] fitted to detailed maps of the infrared sky at 10 wavelengths from 1 μm to 200 μm from the Diffuse Infrared Background Experiment (DIRBE) aboard the Cosmic Background Explorer (COBE)

satellite. This model has a face-on optical depth of $7.11 \times 10^{-8} r^{-0.34}$. Although DIRBE never mapped solar elongations $< 60°$, observations made by the Helios Satellite as far in as r = 0.3 AU and maps assembled from data from the Clementine mission extending to solar elongations as small as 3° yield consistent power-laws.

ZODIPIC is designed to be a general-purpose dust cloud-modeling tool; it can compute images at scattering as well as thermal wavelengths, and offers a variety of tweakable parameters accessible from the IDL command line. ZODIPIC is more elaborate than DISKPIC, but this is not necessarily an advantage in this preliminary study where we only use a few basic parameters to characterize the disk.

3.3.1 Mean dust distribution

In the model proposed by [KWF+98], the cloud coordinates $r = (x^2+y^2+z^2)^{1/2}$ (distance to the star) and z (height perpendicular to the ecliptic plane) are used to describe the dust density. The smooth part of the zodiacal cloud is presumed to be in a form that is separable into radial and vertical terms:

$$n_c(x, y, z) = n_0 r^{-\alpha} f(\zeta) \tag{3.23}$$

where $\zeta = |z/r|$. The vertical distribution is written in a form representing a widened, modified fan model:

$$f(\zeta) = \begin{cases} \exp\left(-\beta(\zeta^2/2\mu)^\gamma\right) & \text{if } \zeta < \mu \\ \exp\left(-\beta(\zeta - \mu/2)^\gamma\right) & \text{if } \zeta > \mu \end{cases} \tag{3.24}$$

This model has been fitted to DIRBE observations, to yield the following parameters:

$$n_0 = 1.13 \times 10^{-7},\ \alpha = 1.34,\ \beta = 4.14,\ \gamma = 0.942,\ \mu = 0.189$$

Moreover, we assume that the dust close to the star sublimates at temperatures higher than 1500 K, so that there is a dust inner cut-off. Figure 3.7 shows how the dust is distributed in a plane perpendicular to the ecliptic plane.

In the following sections, we will assume that the dust distribution is the same around any main sequence star. Only a global multiplicative factor will be used to account for different dust densities. The dust density around our Sun will thus be taken as the standard unit, referred to as *zodi*. A cloud ten times denser than our own will thus be called a 10-zodi cloud.

3.3.2 Additional features

In practice, the dust density distribution is composed of multiple components in addition to the smooth component described above:

- the ring of dust trapped in mean motion resonances with the Earth,

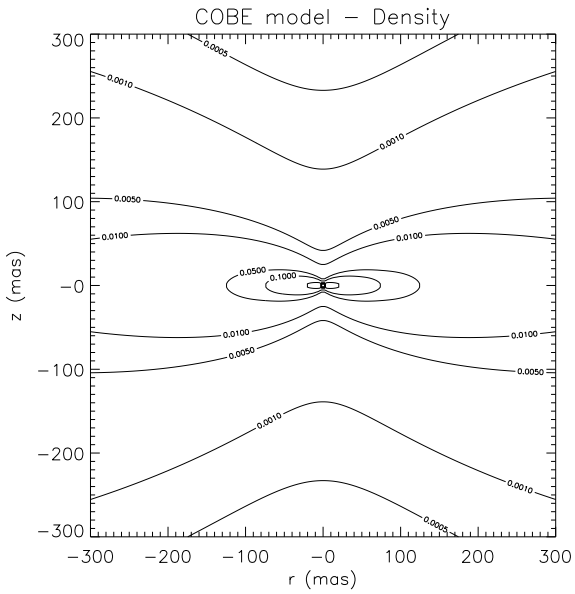

Figure 3.7: Iso-density curves for the DIRBE model of the interplanetary dust cloud around a Sun at 10 pc, seen edge-on. The maximum density has been normalized to unity. An angular distance of 100∼mas corresponds to a distance of 1 AU for this 10 pc target. The plot proves that the cloud is more or less flat, with a peak density near the star.

- the Earth's trailing blob,
- three asteroid dust bands.

All these dust components are included in the ZODIPIC package, and can be added to the smooth component with a user-specified scaling factor.

3.3.3 Thermal and reflected emissions

When computing the flux from a dust disk, there are two contributions to be considered: the thermal emission from the dust grains, supposed to behave like grey bodies, and the stellar light scattered by the grains. The first is dominant in the mid-infrared, while the latter is dominant in the visible. In the near infrared (shortward 4.2 μm), the two contributions have to be taken into account.

3.3.3.1 Thermal emission

In order to compute the thermal emission, the temperature distribution is needed. A fit to the DIRBE data provides the following dependence:

$$T = T_0 r^{-0.467} \tag{3.25}$$

where T_0 is the temperature at a distance of 1 AU from the star. In the case of the Sun, we have $T_0 = 286$ K. The only influence of the star's spectral type is a global increase or decrease of the temperature, which modifies the brightness of the cloud. The thermal emission of the cloud is expressed as an integral along the line-of-sight:

$$Z_\lambda^t = \int n_c(x,y,z)(1-A_\lambda)E_\lambda B_\lambda(T)K_\lambda(T)\mathrm{d}s \tag{3.26}$$

where A_λ is the albedo, E_λ an emissivity modification factor that measures deviations from the blackbody thermal radiance function $B_\lambda(T)$, and $K_\lambda(T)$ the DIRBE color-correction factor. The wavelength-dependent albedo and emissivity factor have been fitted in a series of wavebands by Kelsall et al. [KWF+98], using the COBE/DIRBE data.

3.3.3.2 Scattered light

In addition to its thermal emission, the zodiacal disk scatters the light from the Sun. This component of the dust brightness can be expressed as:

$$Z_\lambda^s = \int n_c(x,y,z)A_\lambda F_\lambda^\odot \Phi_\lambda(\Theta)\mathrm{d}s \tag{3.27}$$

where $F_\lambda^\odot$ is the solar flux and $\Phi_\lambda(\Theta)$ the phase function at scattering angle Θ. An expression of the phase function in the infrared has been proposed by Hong [Hon85], and is used in this model.

In fact, the contribution of the scattered stellar light to the cloud total emission turns out to be almost negligible for the GENIE wavelengths (larger than 2.0 μm). We will thus focus exclusively on the thermal emission in the following paragraphs.

3.3.3.3 Total flux

Four exozodi files have been generated by the ZODIPIC package for the four instrumental set-ups discussed in Table 2.1. The target is a 10-zodi cloud around a Sun-like star located at 10 pc. The total fluxes of the generated exozodiacal clouds are listed in Table 3.2, in units of milli-Jansky. Note that the flux is not necessarily the same for UTs and ATs because of their different fields-of-view.

	UT(8m)	AT(1.8m)
N band	0.97 mJy	1.05 mJy
L' band	0.61 mJy	0.61 mJy

Table 3.2: Total exozodiacal flux for the four default configurations, in the case of a 10-zodi disk around a Sun-like star located at 10 pc.

3.3.4 Brightness distribution

3.3.4.1 Spatial distribution

Figure 3.8 illustrates the brightness distribution in the K, L' and N bands, for a solar-like zodiacal cloud located at 10 pc. It shows a steep decrease of the brightness when moving away from the star. The right-hand plot proves that, even in the N band where we are more sensible to the cold dust, the region inside 1 AU produces more than 80% of the cloud emission. Thus the angular resolution of GENIE should be better than 100 mas in order to probe the bright inner zone of the dust disk.

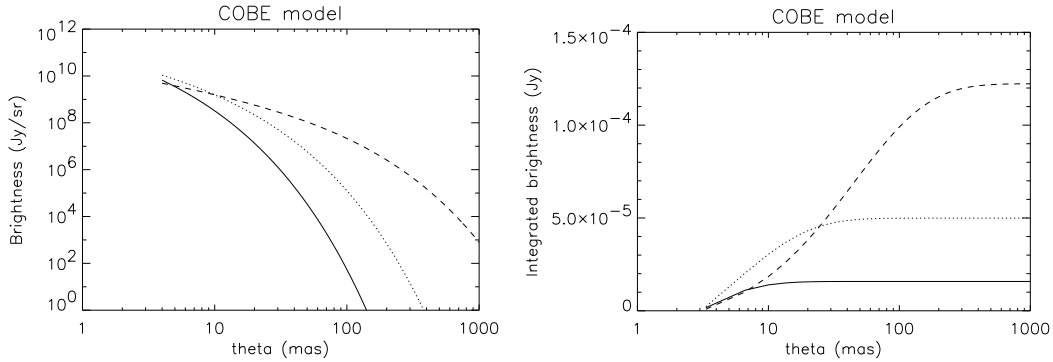

Figure 3.8: Left: Brightness distribution integrated along the z axis as a function of distance to central star, for a solar-like (1 zodi) exozodiacal cloud at 10 pc seen pole-on, plotted in the K (solid), L' (dotted) and N (dashed) bands. The inner cut-off is due to dust sublimation for temperatures higher than 1500 K. Right: Cumulative integrated brightness as a function of distance to central star. The largest part of the cloud thermal emission stems from the region inside 100 mas (equivalent to 1 AU for a target at 10 pc).

3.3.4.2 Spectral distribution

The wavelength dependence of the integrated flux of the exozodiacal disk is plotted in Figure 3.9. It shows a blackbody-like curve, with a peak around 3 μm, meaning that the mean emission temperature is about 1000 K. This is because the hot inner dust has a high density and contributes for a great part to the overall emission. The tail of the curve is wider than for a blackbody because of the contribution of the cold dust. Flux considerations tell us that both the L' and the N band are suited for cloud detection, the former because it contains the peak of the thermal spectrum, the latter because of its large bandwidth.

On the right side of the same figure, the contrast of stellar to exozodiacal fluxes is plotted as a function of wavelength. The higher the contrast, the more difficult it will be to detect the cloud against the bright star. This is the reason why the N band,

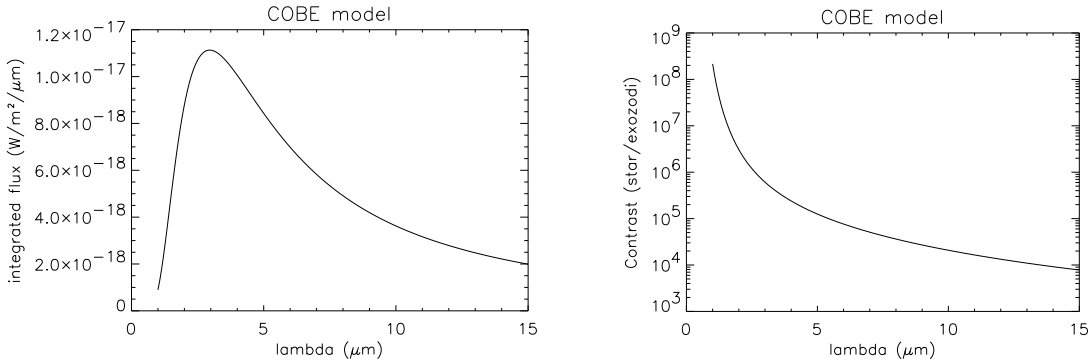

Figure 3.9: Left: Integrated flux (in W/m^2/μm) as a function of wavelength for a 1-zodi cloud. Right: Contrast between exozodiacal cloud and star, i.e., ratio of stellar flux to overall exozodiacal flux.

around 10 μm, is the most appropriate to study exozodiacal disks. Table 3.3 gives the exozodiacal flux and the contrast for different main sequence types, ranging from F0 to M0, located at 10 pc, in the case of a 10-zodi cloud. These are the spectral types that Darwin will observe, and thus also the main targets for GENIE.

	Stellar flux (Jy)			Exozodi flux (mJy)			Contrast ($\times 10^3$)		
Type	K	L'	N	K	L'	N	K	L'	N
F0	115	47.5	7.83	0.99	2.03	3.72	116	23.3	2.11
G0	42.9	18.7	3.22	0.29	0.65	1.46	146	28.9	2.23
K0	17.6	8.07	1.44	0.10	0.26	0.60	183	31.6	2.41
M0	5.76	2.99	0.59	0.014	0.064	0.16	419	46.9	3.80

Table 3.3: Contrast between stellar and exozodiacal fluxes for a 10-zodi cloud at 10 pc around various types of main sequence stars, as seen through a single-mode fiber at a UT focus (field-of-view: $\Omega = \lambda^2/S$). Based on the COBE model from [KWF$^+$98]. This table shows that the contrast increases with later spectral type (and thus cooler stars).

On top of the smooth blackbody spectrum, dust clouds should display silicate emission features in the 10-μm region. The position and width of the spectral lines depend on whether the silicates are crystalline or amorphous. The distinction between these two would be a valuable scientific by-product for the brightest disks, and requires a spectral resolution of at least 100.

3.4 Planets: hot Jupiters

Since 1995, more than 100 giant planets have been found around nearby stars by radial velocity measurements. Some of them were found very close to their parent stars. Tau Bootes b, for example, orbits at 0.05 AU of an F7 dwarf, raising its temperature to about 1500 K. The thermal emission of such a hot Jupiter is peaking around 2 μm, and is only about 10^4 times smaller than the emission from the star at that wavelength. Moreover, the angular separation between the planet and its host star is of about 3 mas, a resolution achievable with a 130 m baseline in the L' band. Thus ground-based nulling interferometry in the K or L' bands at the VLTI is well suited to the detection of such planets.

3.4.1 Candidate targets

In order to be detectable with the GENIE nulling interferometer, the planet should be warm enough ($T > 700$ K required for a star/planet contrast below 10^6 in the K band), but not too close to the star in order to be resolved (angular separations below 2 mas cannot be resolved).

A list of potential targets is presented in Table 3.4. It shows that a typical target consists in a Jupiter-sized planet orbiting at 0.1 AU from a Sun-like star located at about 20 pc. The couple is then seen under an angular separation of 5 mas. This imaginary case will be our reference target in the following paragraph. Let us immediately notice that the N band is not well suited for such a target, since the maximum angular resolution in the N band available on the VLTI site is about 10 mas (with a 100 m baseline pointing at zenith).

3.4.2 Brightness and contrast

The brightness of a hot Jupiter orbiting at various distances from a Sun-like star at 20 pc is plotted in Figure 3.10. It shows the necessity of looking at planets very close to their stars in order to have a large enough flux. The contrast between the star and the planet is plotted in the same figure, and suggests that the N band would be more appropriate to observe a hot Jupiter. However, the lower angular resolution and the higher thermal background are two major difficulties that make the N band inappropriate for hot Jupiter detection. Indeed, the most promising wavelength for hot Jupiter detection is the L' band, as will be discussed in chapter 7.

Hot Jupiters are currently implemented in GENIEsim as blackbodies. This is sufficient as a first step to assess the feasibility of hot Jupiter detection. Models for brown dwarfs and irradiated giant planets have recently been published [ABC+02], [BHLL01], including high resolution spectra for hot Jupiters. Such spectra will soon be implemented in GENIEsim. The identification of deep methane lines in the destructive output of GENIE could be the key to detect hot giant planets (see section 6.6).

	Star		Planet				
Name	Dist [pc]	Type	a [AU]	θ [mas]	T [K]	L' [mJy]	Contrast
tau Boo b	15.6	F7V	0.05	3.21	1530	4.6	3000
51 Peg b	14.7	G2IV	0.051	3.47	1220	2.7	2700
HD162060 b	31.3	K2V	0.072	2.30	870	0.16	2700
HD130322 b	31.3	K0V	0.088	2.95	790	0.11	8600
HD108147 b	38.6	G0V	0.104	2.69	990	0.18	120000
Gl86 b	10.9	K1V	0.11	10.1	670	0.36	19000
55 CnC b	13.4	G8V	0.115	8.58	740	0.41	14000
HD38529 b	42.4	G4IV	0.129	3.06	1181	0.29	15000
HD195019 b	37.4	G3V	0.14	3.74	870	0.11	16000
HD6434 b	40.3	G3IV	0.15	3.72	730	0.04	21000
Sun@20pc b	20.0	G2V	0.1	5.00	860	0.38	8200

Table 3.4: Ten potential hot Jupiter targets observable from Paranal (-24.5° latitude). The planet orbital axis a in given in AU and the angular separation θ between the star and the planet in milli-arcsec (assuming that the system is seen face-on), based on the Extrasolar Planet Encyclopedia [Sch]. The planet equilibrium temperature and the L' band flux are computed with blackbody assumption. The star/planet contrast is computed in the L' band.

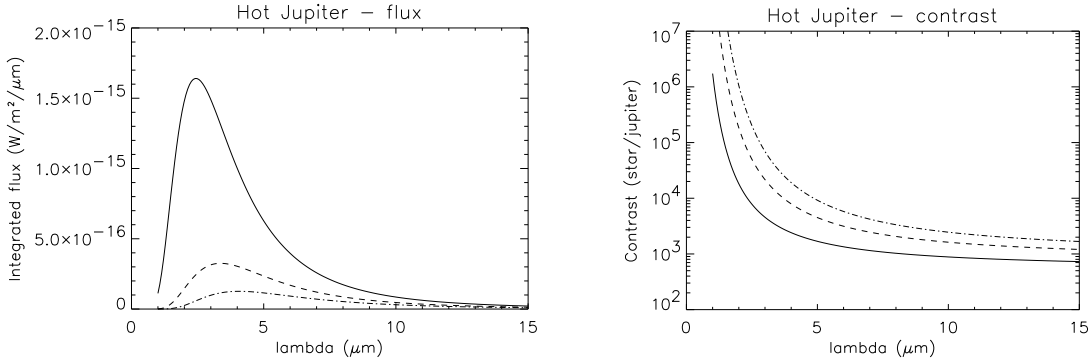

Figure 3.10: Left: Integrated flux (in W/m^2/μm) as a function of wavelength for a hot Jupiter at 0.05 AU (solid line), 0.1 AU (dashed line) and 0.2 AU (dashed-dotted line) of a 20 pc Sun-like star. Right: Contrast between the star and the hot Jupiter, i.e., ratio of stellar flux to planetary flux.

Chapter 4

GENIE and its environment

4.1 The atmosphere

4.1.1 Atmospheric windows

Most of the infrared light coming to us from the Universe is absorbed by water vapor and carbon dioxide in the Earth's atmosphere. Only in a few narrow wavelength ranges can infrared light make it through (at least partially) to a ground-based infrared telescope. Figure 4.1 shows the transmission of the atmosphere above the Mauna Kea observatory in the near- and mid-infrared. This figure shows that observations should only be done in the infrared atmospheric windows listed in Table 4.1. Among them, the preferred wavebands for GENIE are the N/N_{red} and L' bands (see [Abs02]).

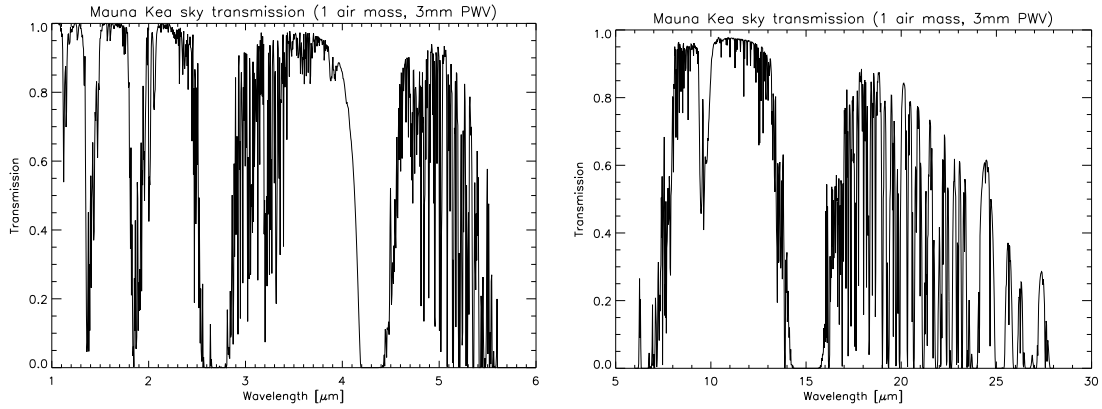

Figure 4.1: Atmospheric transmission for the Mauna Kea site (data from the Gemini web site [PR]). The 3 mm of precipitable water vapor (PWV) make these curves a little bit optimistic for the Paranal atmospheric conditions.

Spectral band	K	L'	M	N	N_{red}
Central wavelength (μm)	2.2	3.8	4.8	10.5	11.25
Bandwidth $\Delta\lambda$ (μm)	0.40	0.6	0.6	5	2.5
Mean sky transparency	93%	89%	68%	90%	96%

Table 4.1: The atmospheric windows and an estimation of their transparency, based on measurements on top of Mauna Kea (see the Gemini web site [PR] for more details). The reduced N band corresponds to the cleanest part of the 8-13 μm region.

4.1.2 Atmospheric turbulence

Atmospheric turbulence causes local variations in the temperature and in the density of air and water vapor [Rod81]. Since the refractive index is a function of both, it varies according to the same spatial spectral density. Local variations in the refractive index cause optical path differences for photons on initially parallel tracks, resulting in wavefront distortions. Atmospheric turbulence is usually described by the theory of energy cascades due to Kolmogorov which states that, in fully developed turbulence, the kinetic energy of large scale motion is transferred to smaller and smaller scale motions. For a plane wave, in the case of Kolmogorov turbulence and in the near-field approximation, the spatial power spectrum of the wavefront phase is given by [Tat71]:

$$W_\phi(\boldsymbol{\kappa}) = 0.033(2\pi)^{-2/3}(2\pi/\lambda)^2 C_N^2(h)\kappa^{-11/3}\mathrm{d}h \ , \tag{4.1}$$

where λ is the wavelength, C_N^2 the so-called structure constant of the refractive-index fluctuations in a turbulent layer of thickness dh, and κ the modulus of the spatial frequency vector $\boldsymbol{\kappa}$. The structure constant depends on local atmospheric conditions, and should therefore be measured at the site of interest. Measurements of $C_N^2(h)$ for Paranal are given in [Qui99], but an analytical approximation is more convenient. Such an approximation is given in [Goo85]. We use a slightly modified version which provides an accurate representation of the Paranal data:

$$C_N^2(h) = c_1 h^{-2/3} e^{h/h_1} + c_2 h^{10} e^{h/h_2} \tag{4.2}$$

with $c_1 = 2.0 \times 10^{-14}$ m$^{-2/3}$, $c_2 = 5.9 \times 10^{-53}$ m^{-10}, $h_1 = 3000$ m, $h_2 = 1000$ m. This function is shown in Figure 4.2.

A usual parameter to describe the strength of turbulence is the Fried parameter, which represents the atmospheric coherence length. It is related to the structure constant as follows [Rod81]:

$$r_0 = \left[0.423(2\pi/\lambda)^2(\cos z)^{-1}\int C_N^2(h)\mathrm{d}h\right]^{-3/5} . \tag{4.3}$$

This relation shows that r_0 depends on the wavelength ($r_0 \propto \lambda^{-6/5}$) and on the zenithal distance angle z. The Fried parameter is the aperture size below which (approximate) diffraction-limited imaging is possible without phase correction.

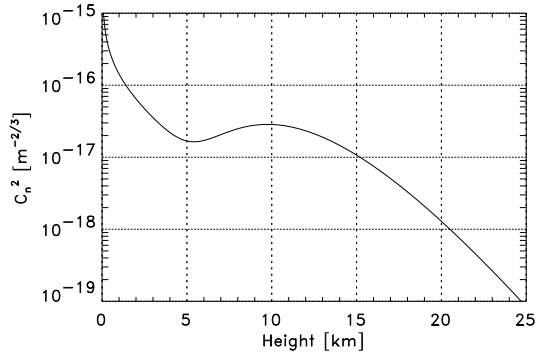

Figure 4.2: The structure constant of the Kolmogorov atmospheric turbulence spectrum, as a function of height.

A further hypothesis is needed to relate the spatial power spectrum $W_\phi(\boldsymbol{\kappa})$ to the one-dimensional temporal power spectrum $w_\phi(f)$, where f is the temporal frequency. The Taylor hypothesis states that the whole phase screen is translated at the wind velocity $\mathbf{v}$, its shape remaining unchanged (*frozen turbulence* approximation). This assumption can be written as follows:

$$\phi(\mathbf{r}, t+\tau) = \phi(\mathbf{r} - \tau\mathbf{v}, t) \tag{4.4}$$

Assuming a wind along the x axis, the temporal spectrum of phase fluctuations can be written as [CRM95]:

$$\begin{aligned} w_\phi(f) &= 0.033 \frac{C_N^2(h)\mathrm{d}h}{v}(2\pi)^{-2/3}(2\pi/\lambda)^2 \int_{-\infty}^{+\infty} \left((f/v)^2 + \kappa_y^2\right)^{-11/6} \mathrm{d}\kappa_y \\ &\propto C_N^2(h)\frac{\mathrm{d}h}{v}\left(\frac{f}{v}\right)^{-8/3} \end{aligned} \tag{4.5}$$

A $-8/3$ power law is thus found for the temporal-frequency dependence. Note that the phase variance, equal to the integral of w_ϕ over the whole frequency domain, is infinite. This is a well-known property of the Kolmogorov model. That singularity disappears with better models that take into account a turbulence outer scale L_0 such as the Von Kármán phase spectrum, which flattens the slope of the power spectrum for spatial frequencies below $\kappa_0 = 2\pi/L_0$, i.e., temporal frequencies below v/L_0.

4.1.2.1 The piston mode

The piston mode of turbulence corresponds to the fluctuations of the difference in average phase between the two apertures. In order to compute the power spectrum of piston, two phenomena must be taken into account:

- *Correlation between the two apertures.* The Kolmogorov spectrum for the phase difference between two points is a little more complicated than the bare $-8/3$

slope, because the phase difference is similar to a first derivative at low frequencies, whereas at high frequencies the phases on these two points are decorrelated and the spectrum is therefore roughly twice the phase spectrum [CRM95]. There are thus two domains in the spectrum, following $f^{-2/3}$ for frequencies below $f_{c_1} = 0.2v/b$ (with b the distance between the two points) and $f^{-8/3}$ for frequencies above f_{c_1}.

- *Pupil averaging.* The piston mode is defined by the spatial average of the phase over the pupil. It can be shown that the pupil averaging introduces another break in the power spectrum [CRM95]: for frequencies above $f_{c_2} = 0.3v/D$ (with D the telescope diameter), the slope becomes $-17/3$ instead of $-8/3$. The frequencies above this cutoff are thus dramatically attenuated due to pupil filtering.

In optical interferometry, the piston effect between the two arms of an interferometer induces an erratic movement of the fringes, linked to the optical path difference between the two beams. The power spectrum for the fringe motion is illustrated in Figure 4.3. It has been confirmed experimentally by several authors ([Lay97], [NB91], [CSS87]). In GENIEsim, the user can choose between the Kolmogorov and the von Kármán spectra, which are both implemented in the routine `psd_atm.pro`. The typical RMS fluctuation of piston is 20 μm RMS. A user-specified spectrum can also be used, provided that an analytical expression is given.

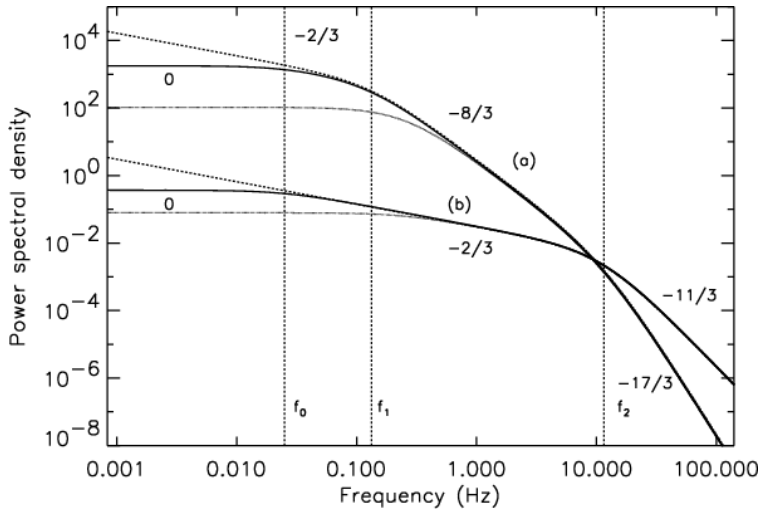

Figure 4.3: Theoretical power spectra of: (a) fringe motion (in μm^2/Hz) and (b) angle of arrival (in arcsec^2/Hz) for a pure Kolmogorov model (dashed line), for a von-Kármán model with L_0=40 m (dotted line) and L_0=400 m (solid line). Taken from Sorrente et al. 2001 (A&A 365, 301).

4.1.2.2 Longitudinal dispersion

The main contributors to the OPD difference between the arms of a ground-based interferometer are dry air and water vapor. Their reduced refractive index is defined as:

$$\hat{n}(\lambda) = \frac{n(\lambda) - 1}{c\,\rho} \tag{4.6}$$

where c is the speed of light and ρ their molar density in mole/m^3. The reduced refraction index will be expressed in units of femtoseconds per mole/m^2. According to [MLP03], water vapor typically composes 0.3% of the molar volume of air (= 31.5 mole/m^3) at Paranal. The molar density of water vapor is therefore of about 0.095 mole/m^3, which translates to a number density of 0.6×10^{17}cm^{-3}.

The reduced refractive indexes of dry air and water vapor are plotted as a function of wavelength in Figure 4.4. The left-hand plot shows that dry air produces very little dispersion in the infrared: its refraction index is almost constant. On the other hand, water vapor is highly dispersive, and adds wavelength dependence to the OPD.

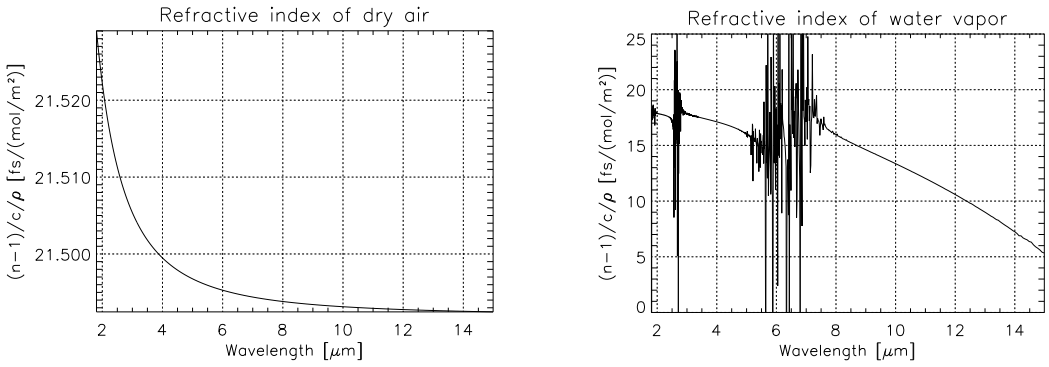

Figure 4.4: Normalized refractive indexes of dry air and water vapor in units of fs/(mole/m^2). These plots have been produced by the routines `n_air.pro` and `n_h2o.pro`.

Since they are produced by the same turbulent atmosphere, column density fluctuations of dry air and water vapor are assumed to follow the same PSD. The power spectrum of column density fluctuations is thus the classical Kolmogorov (or von Kármán) spectrum of Figure 4.3. A useful concept to describe the column density fluctuations of water vapor is the concept of "Water-vapor Displacing Air" (WDA), introduced by Meisner [MLP03]. Because a column density fluctuation of water vapor induces an opposite variation in the dry air column density, we can define a mole of WDA as one mole of water vapor plus one *negative* mole of dry air. Consequently, it has a reduced refraction index $\hat{n}_{\rm WDA}$ given by $\hat{n}_{\rm water} - \hat{n}_{\rm air}$. At our wavelengths, the reduced refraction index of WDA is negative, as shown in Figure 4.5. Employing the concept of WDA,

we can view a quantity of air as consisting of an amount of dry air given solely by the ambient temperature and pressure *plus* a quantity of WDA representing the humidity.

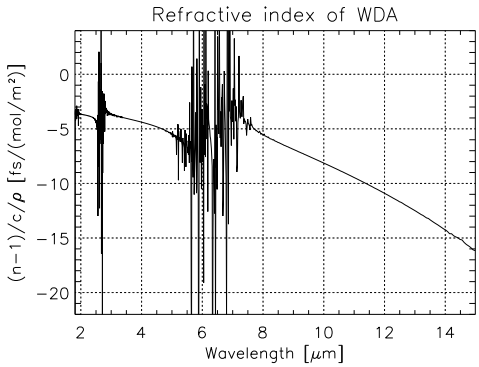

Figure 4.5: Reduced refraction index of WDA at infrared wavelengths. This plot has been produced by the routine `n_h2o.pro`.

The power spectrum of water seeing has been measured in the sub-millimeter domain by Masson at Mauna Kea [Mas94] over integration periods of 15 minutes. The measured variance of the column number density is $4 \times 10^{19}\text{cm}^{-2}$. This corresponds to $\sigma_{\Sigma,15\text{min}} = 0.67$ mole/m^2. The power spectrum for typical conditions follows a broken power law, with the power proportional to $(f/f_c)^{-0.5}$ for $f > f_c$, and to $(f/f_c)^{-2.5}$ for higher frequencies, and the corner frequency $f_c = 0.01$ Hz. This measured power-law does not differ much from the theoretical Kolmogorov spectrum, with slopes of $-2/3$ and $-8/3$. Similar measurements have been carried out at Paranal. The estimates given by [MLP03] for the RMS fluctuation of water vapor are much larger than those given by Masson: $\sigma_{\Sigma,100\text{s}} \simeq 1.5$ mole/m^2 for a 66-m baseline and an integration time of 100 sec. Similar values have been measured by [Lay97] in the sub-mm domain at Mauna Kea. This RMS value is used in the GENIE simulator. The RMS phase offset produced by an RMS water column number density $\sigma_{\Sigma,100\text{s}}$ at wavelength λ is given by:

$$\sigma_{\Delta\phi,100\text{s}}(\lambda) = \frac{2\pi c}{\lambda}\hat{n}_{\text{WDA}}(\lambda)\,\sigma_{\Sigma,100\text{s}} \tag{4.7}$$

The typical RMS phase fluctuations for the Paranal atmospheric conditions are given in Table 4.2 as a function of wavelength.

Figure 4.6 shows the amount of dispersion and differential OPD induced by typical column density fluctuations of dry air and WDA. In the infrared, the dispersion induced by dry air fluctuations is negligible as compared to water vapor-induced dispersion (left columns in Figure 4.6). The only effect of dry air fluctuations is thus wavelength-independent OPD fluctuations at each telescope (referred to as *piston*). According to this figure, only WDA should be included in the random dispersion generator `rndm_disp.pro`.

	K	L'	M	N
$\hat{n}_{\mathrm{WDA}}$ [fs/(mole/m^2)]	-3.772	-4.241	-5.161	-8.392
RMS phase [rad]	4.84	3.16	3.04	2.32
RMS phase [μm]	1.70	1.91	2.32	3.77

Table 4.2: RMS phase in radians and microns as a function of wavelength produced by an RMS column density fluctuation of WDA of 1.5 mole/m^2. The refractive index of WDA is computed for typical Paranal atmospheric conditions.

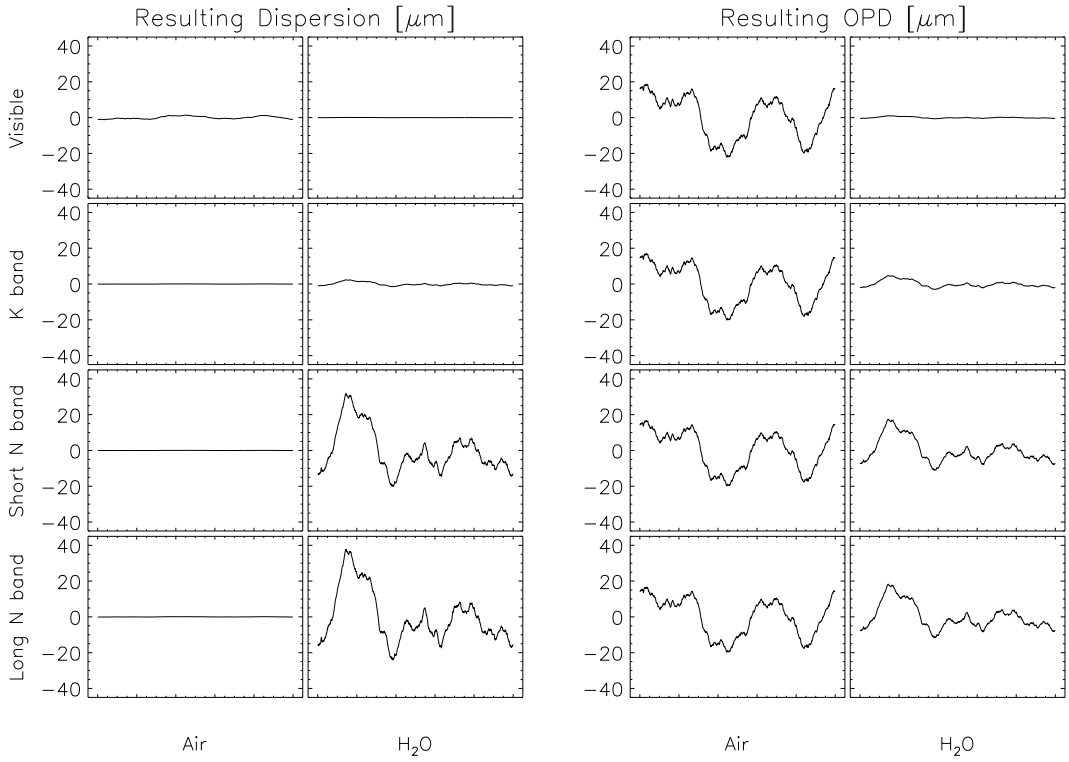

Figure 4.6: Time series for differential OPD and dispersion induced by typical column density fluctuations of dry air and WDA (water vapor displacing air), adapted from [MLP03]. Short N-band centered at 8 μm, long N band at 14 μm. The dispersion induced by dry air is negligible in the infrared (the dry-air induced OPD is the same at all wavelengths). This figure has been produced by the routine `rndm_disp.pro`.

4.1.2.3 The Strehl ratio

The quality of a wavefront is generally measured by its Strehl ratio, defined as the ratio of the on-axis intensity to that for a diffraction limited image. A phase aberration $\phi(\boldsymbol{\theta})$

will result in a Strehl ratio of:

$$S = \frac{\left| \int \int_{\Omega} e^{i\phi(\boldsymbol{\theta})} d\boldsymbol{\theta} \right|^2}{\left| \int \int_{\Omega} d\boldsymbol{\theta} \right|^2} \, . \tag{4.8}$$

For small phase aberrations ($\sigma_\phi < 2$ rad), the expression of the Strehl ratio reduces to:

$$S \simeq e^{-\sigma_\phi^2} \, , \tag{4.9}$$

where σ_ϕ^2 is the phase variance over the pupil. The purpose of adaptive optics is to increase the value of the Strehl ratio towards unity, to get a nearly-diffraction limited image (see paragraph 4.2.1.3). We will see in section 4.3.1 that the Strehl ratio determines the amount of light coupled into the single-mode fibers at the focus of the telescopes. The Strehl ratio strongly depends on the wavelength since $\sigma_\phi = 2\pi\sigma_{\rm WFE}/\lambda$ (with $\sigma_{\rm WFE}$ the wavefront error expressed in meters): it rapidly gets close to unity in the mid-infrared domain as a function of increasing wavelength. In the absence of adaptive optics, an approximate value for the Strehl ratio can be obtained using the Kolmogorov theory [Nol76]:

$$S \simeq \exp\left(-1.0039(D/r_0)^{5/3}\right) \tag{4.10}$$

with D the telescope diameter and r_0 the Fried parameter. Table 4.3 gives the theoretical Strehl ratio for a UT and an AT in the K, L', M and N bands for a typical Fried parameter $r_0 = 10$ cm in the visible (500 nm).

	K	L'	M	N
r_0	60 cm	1.1 m	1.5 m	3.9 m
Strehl - UT	4×10^{-9}	0.0016	0.018	0.43
Strehl - AT	0.013	0.23	0.40	0.83

Table 4.3: Typical Fried parameter values in the infrared atmospheric windows for Cerro Paranal, and associated Strehl ratios for an 8-m UT and a 1.8-m AT. This table shows that an advanced AO system is probably not needed when operating with ATs in the mid-infrared.

4.1.2.4 Scintillation

Scintillation is the effect of rapid intensity fluctuations of a small (point-like) source as a result of the interference of light rays which are diffracted by turbulent cells. It is therefore highly chromatic. The condition for scintillation to take place is that the light propagates through the atmosphere over distances longer than the Fresnel propagation length, $d_{\rm F} = r_0^2/\lambda$, where r_0 is the Fried scale. In other words, the Fresnel scale $r_{\rm F} = (\lambda\, h \sec z)^{1/2}$ must be larger than r_0, where h is the height of the turbulent layer and z the zenithal distance [Qui99]. In Figure 4.7, $r_{\rm F}$ and r_0 are compared as a function

of wavelength. It shows that in the relevant IR bands, r_0 is always at least equal to, or larger than r_F, even for high turbulent layers and rather poor seeing conditions ($r_0 = 0.05$ m at 500 nm) and a zenith distance of 45°. This is because $r_0 \propto \lambda^{6/5}$, while $r_\mathrm{F} \propto \lambda^{1/2}$. So, in general, conditions are at worst at the limit of where scintillation is expected. Nevertheless, for completeness, we included the option to calculate the effects of scintillation.

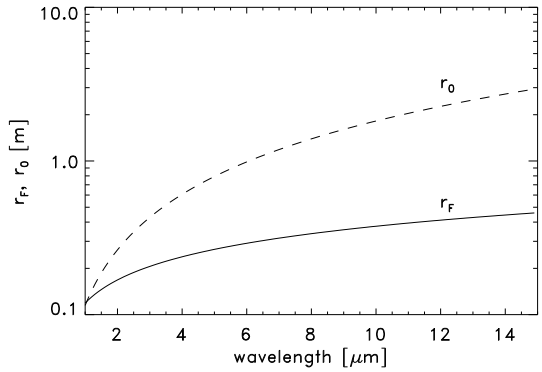

Figure 4.7: Comparison of the Fresnel and Fried scales as a function of wavelength.

Atmospheric scintillation creates a rapidly variable imbalance between two beams in the interferometer. The effects of scintillation can be quantified by determining the relative intensity fluctuations $\mathrm{d}I/I$, which can be written as $\mathrm{d}\ln I$ in the case of small intensity fluctuations. For a Kolmogorov turbulence model the variance of the log intensity fluctuations is given by [Qui99]:

$$\sigma^2_{\ln I} = 2.24k^{7/6}(\sec z)^{11/6} \int C_N^2(h)h^{5/6}\mathrm{d}h \tag{4.11}$$

where $k = 2\pi/\lambda$ is the wavenumber and $C_N^2(h)$ the structure constant that determines the structure function of the Kolmogorov turbulence. Equation (4.11) is actually only valid for small apertures ($D \ll r_\mathrm{F}$). The scintillation pattern varies spatially on the Fresnel scale, so for telescopes larger than r_F the effect of scintillation is reduced by averaging over multiple independent sub-apertures when a spatial filter is used in the interferometer. This is because only variations of the average intensity couple efficiently into a single-mode fiber [Qui03]. According to [Rya02], the aperture averaging can be approximately described by applying a correction factor $A(h)$ to the right-hand side of equation (4.11):

$$A(h) = \left(1 + 1.1\left(\frac{D}{r_\mathrm{F}(h)}\right)^{14/6}\right)^{-1} \tag{4.12}$$

Since r_F is a function of h this term has to be taken inside the integral. Figure 4.8 shows a comparison of the resulting PSD for scintillation with the PSD for residual Strehl ratio

fluctuations at a UT, running MACAO adaptive optics, under typical conditions. From this comparison it is clear that scintillation is negligible compared to the residual Strehl ratio fluctuations.

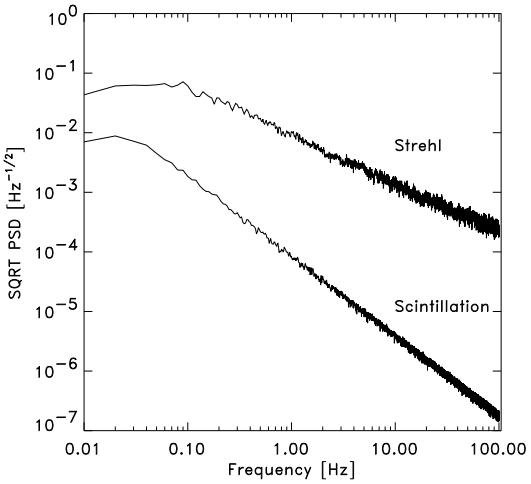

Figure 4.8: Comparison of the PSDs for scintillation and Strehl ratio fluctuations after the adaptive optics, but before the intensity matching loops.

4.1.3 Atmospheric refraction

Photons of different wavelengths, which are initially on coinciding paths, are transversely dispersed, i.e., they end up on different tracks through the atmosphere. The phase fluctuations for different wavelengths may thus become partially or completely decorrelated. This would be a serious problem if K-band photons had to be used to correct for N-band turbulence. To assess this problem, let us look at the differential refraction of K- and N-band light through a smooth, but realistic atmosphere. This process is well described by Green [Gre85] and at the "ESO - La Silla Astroclimatology" web-site [ESO]. Here we have used the IDL code `diff_atm_refr.pro` by Enrico Marchetti which can be obtained from the ESO web-site. It computes the atmospheric differential refraction for Paranal as a function of zenith distance, temperature, pressure and relative humidity of the air, based on an empirical parameterization of the refraction by moist air. For typical Paranal conditions: $T = 284$ K, $P = 743$ mbar and a relative humidity of 14.5%, the differential refraction between the N and K bands, at a maximum zenith distance of 70°, is 126 mas. This is equivalent to 6 mm over a distance of 10 km, barely the size of the smallest turbulent cells. This result indicates that beams of different wavelengths do not strongly diverge. Because the size of the smallest cells is orders of magnitude larger than the wavelength of the light, there is no reason to suspect that this conclusion will change much for a realistic atmosphere. Therefore we expect that optical path

fluctuations in the K band are strongly correlated with N-band fluctuations, which is very important for OPD control.

4.1.4 The infrared sky brightness

The infrared sky brightness can be directly deduced from the sky transmission (Figure 4.1) and from the effective temperature of the atmosphere, by multiplying the Planck function for blackbody emission by the sky emissivity. According to the Kirchhoff's law, the sky emissivity is the complementary of its transmission. The sky brightness is plotted in Figure 4.9 for an atmosphere at 284 K, typical for the Paranal sky conditions.

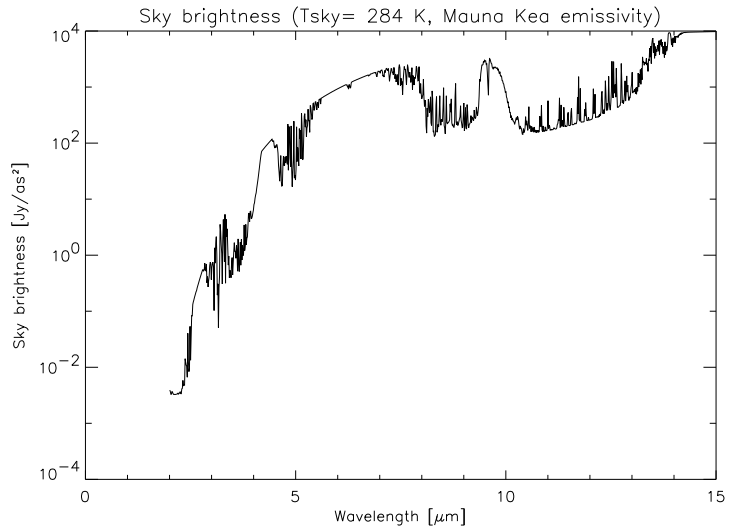

Figure 4.9: Sky brightness for the Paranal site, assuming an emissivity similar to that of Mauna Kea (data from the Gemini web site [PR]). Curve produced by the routine `sky_trans.pro`.

At wavelengths shorter than 2.4 μm, the thermal emission from the atmosphere is superseded by the brightness of the OH atmospheric lines, which are not well reproduced in GENIEsim (a constant value is added below 2.5 μm to account for the mean OH brightness). This is not really a problem since high-resolution measurements will not be carried out in the K band: this band is only devoted to feed the control subsystems.

The mean sky brightness in the infrared atmospheric windows has been computed for typical Paranal atmospheric conditions (284 K, 3 mm PWV), and is given together with the instrumental emission in Table 4.7 (see page 62). This table shows that, due to the large number of relay optics in the VLTI, the infrared emission associated to the instrument itself is almost 10 times larger than the infrared emission of the atmosphere!

4.2 The Very Large Telescope Interferometer

The ESO Very Large Telescope (VLT) at the Cerro Paranal Observatory (Chile) is one of the world's largest and most advanced optical telescope. It presently comprises four 8-m reflecting Unit Telescopes (UTs), soon complemented by four moving 1.8-m Auxiliary Telescopes (ATs), the light beams of which can be combined in the VLT Interferometer (VLTI). The layout of the VLTI is shown in Figure 4.10. The minimum and maximum distances between two UTs are respectively 46.65 m (UT2-UT3) and 130.2 m (UT1-UT4). The distance between two ATs on the main east-west track varies between 8 m and 144 m by steps of 8 m. The maximum baseline is 202 m.

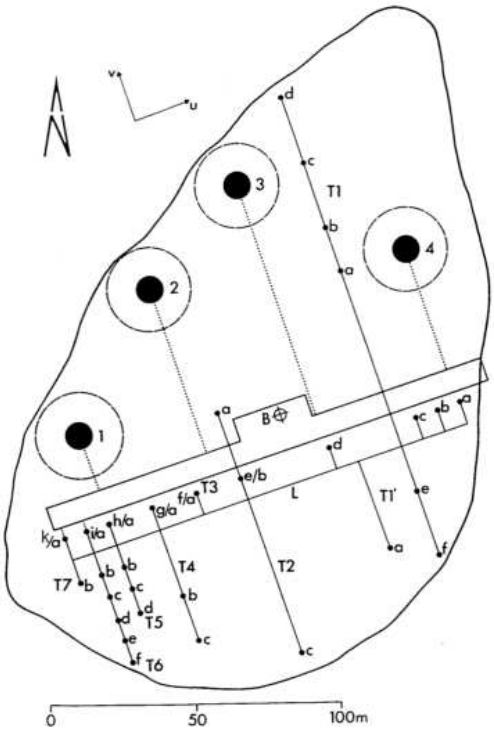

Figure 4.10: Layout of the individual VLTI elements. Unit Telescopes are shown as large, filled circles, and the possible locations of ATs indicated by small, filled circles. These circles represent the diameters of the primary mirrors when pointed at the zenith. Solid lines show the location of tracks for transporting ATs between stations.

4.2.1 Facilities and subsystems

By 2007, when GENIE is supposed to come on-line, the VLTI will offer the following facilities [WG03]:

- Four UTs equipped with adaptive optics (MACAO),

- Two ATs equipped with single-feed relay optics and tip/tilt correction (STRAP),
- Two ATs equipped with dual-feed (PRIMA) relay optics and tip/tilt correction (STRAP),
- Six Delay Lines (DLs) equipped with Variable Curvature Mirrors for pupil re-imaging,
- The dual-feed facility PRIMA with two fringe sensor units, laser metrology and star separator on two ATs (PRIMA "Phase 1"),
- Closed-loop optical path difference control ("fringe tracking") with FINITO or PRIMA FSU A/B as Fringe Sensor Units (FSU).

4.2.1.1 Delay Lines

The function of the Delay Lines (DLs) is to compensate for the external delay due to the position of the star in the sky and to the interferometer geometry, and for OPD fluctuations due to atmospheric turbulence. The DL is characterized by its transfer function (Figure 4.11), which has a bandwidth of about 200 Hz. Above this frequency, the DL cannot compensate efficiently for OPD fluctuations. The Variable Curvature Mirror inside the DL has the function to re-image the pupil at a desired location in the interferometric lab, with an accuracy of ±125 mm [KG01]. If the Beam Compressors are used, the position precision is improved to ±6.4 mm.

A digital model for the DL, directly derived from measurements taken on the real system, is available at ESO, and is currently being implemented in the GENIE simulator.

4.2.1.2 Fringe Sensing Unit

Fast compensation of OPD variations is very important for a successful operation of GENIE. Figure 4.12 shows the block diagram for OPD control at the VLTI. The components of the loop are the Fringe Sensing Unit (FSU), the OPD Controller (OPDC) and the DL. The function of the FSU is to measure the phase delay between two (or more) beams. The measured signal is sent to the OPDC which computes and sends a correction signal to the DL. By 2007, there will be two types of FSUs available [WG03]:

- FINITO (Fringe Tracking Instrument of Nice and Torino) will measure the OPD between up to three beams in the H band,
- PRIMA-FSU (Phase-Referenced Imaging and Microarcsecond Astrometry) will measure the OPD between two beams in the K band, with a better sensitivity than FINITO.

Estimated OPD control performance has been computed by R. Wilhelm [WG03] using the VLTI Integrated Model. The fringe tracking system is characterized by the output Power Spectral Density (PSD) of residual OPD, which contains contributions

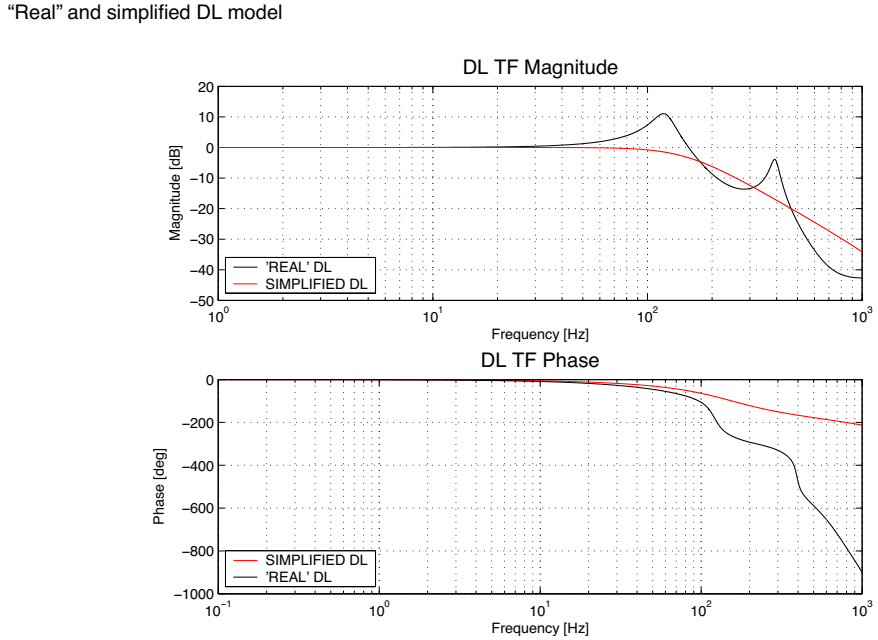

Figure 4.11: Transfer function of the VLTI Delay Lines in magnitude and phase (courtesy of R. Wilhelm). There are two resonance frequencies, at 120 Hz and 400 Hz, respectively due to the carriage and to the piezo-translators. The transfer function strongly decreases for frequencies above 120 Hz due to the finite bandwidth of the mechanical system.

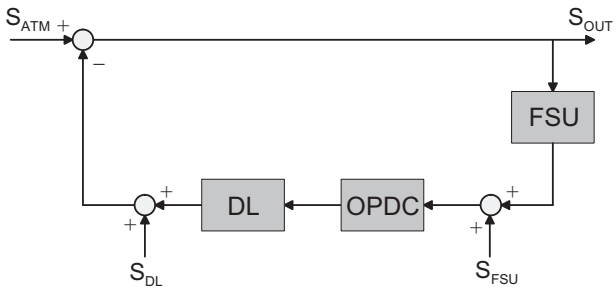

Figure 4.12: Block-diagram of the VLTI fringe tracking system. The OPD power spectra associated with the atmosphere, the fringe sensing unit and with the delay line are respectively written S_{ATM}, S_{FSU} and S_{DL}, while the total output power spectrum is S_{OUT}.

from the atmospheric piston, the FSU noise and the DL noise (see Figure 4.13). Table 4.4 lists the standard deviations of the residual OPD for different loop sampling frequencies f_s = 2 kHz, 4 kHz and 8 kHz. Currently the DL electronics imposes an upper limit of 2 kHz. GENIEsim can reproduce similar figures by simulating close-loop OPD control

for the VLTI.

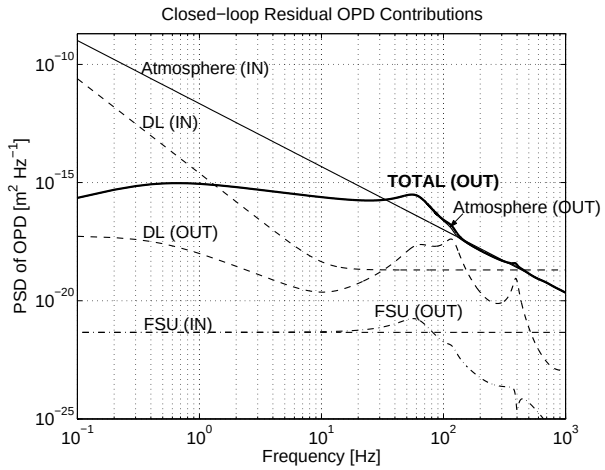

Figure 4.13: PSDs of residual OPD contributions (after closed-loop control) for the three OPD noise sources in the fringe tracking loop. Simulation parameters as listed in Table 4.4 with $f_s = 2$ kHz. Figure taken from [WG03].

f_s	2 kHz	4 kHz	8 kHz
σ_{FSU}	0.3 nm	0.3 nm	0.3 nm
σ_{DL}	15.5 nm	17.0 nm	18.3 nm
σ_{ATM}	157.3 nm	146.3 nm	136.2 nm
σ_{OUT}	158.0 nm	147.3 nm	137.5 nm

Table 4.4: Simulated standard deviation of the contributions to the residual OPD for an exposure time of 2 sec and different control loop sampling frequencies f_s. The simulation assumed the usage of a PRIMA FSU as fringe sensor. Simulation parameters: baseline $b = 100$ m, magnitude $m_K = 2$, Strehl ratio $\bar{S}_K = 0.36$, FSU integration time $T_i = 0.5$ msec, FSU read-out noise of 20 electrons, FSU fringe visibility of 75%, Fried parameter $r_0 = 60$ cm in the K band, mean wind speed of 11.6 m/sec. Taken from [WG03].

4.2.1.3 Adaptive optics system

The use of adaptive optics is very important for interferometers using spatial filtering, in order to optimize and, even more important for GENIE, equalize the flux from different beams coupled into the single-mode fibers. GENIE will benefit from the existing VLTI closed-loop wavefront correction systems [WG03]:

- MACAO, the Multi Application Curvature Adaptive Optics system, is an ESO in-house developed 60-element curvature adaptive optics system. Four of these

systems will be installed on the four UTs, feeding the VLTI delay lines with a corrected IR beam from 1 to 13 μm with up to 60% Strehl in K band for bright stars. The first MACAO system has just been installed at UT2, and successfully achieved its "First Light".

- STRAP is a System for Tip-tilt Removal with Avalanche Photodiodes, currently installed on the UTs. By 2007, STRAP will equip all the ATs and will be replaced by MACAO on the UTs.

Both systems sense the wavefront at visible wavelengths, and both use neutral density filters for stars brighter than magnitude $m_V = 9$. Physically, the measurement of the wavefront aberrations is performed at the level of the UT's or AT's Coudé focus. In the case of STRAP, the tip/tilt correction signal is applied to the M6 mirror located in a pupil plane of the ATs, while MACAO uses a deformable mirror mounted on a tip/tilt stage situated in a UT pupil plane at the location of the so-called M8 mirror. An additional closed-loop system called IRIS (InfraRed Image Sensor) could be installed in the interferometric laboratory to compensate for the additional tip/tilt introduced by air turbulence in the underground light path through the delay lines [WG03].

MACAO Simulated performances of the MACAO system are presented in Figure 4.14 for the K band. According to these simulations, the residual tip/tilt error on sky in 2 s of exposure time is 13 mas RMS. The mean Strehl ratio in the K band is 0.36, with an RMS fluctuation of 0.063 for an exposure time of 2 s. Table 4.5 translates these values into the L' and N bands. In GENIEsim, the Strehl ratio at the output of the AO system is specified by its mean value, its RMS fluctuation and by the slope of its PSD. According to Figure 4.14, this slope is of about -2, so that the energy is infinite at $f = 0$. In practice, the power spectrum flattens at frequencies below $2\pi v/L_0$, with v the mean wind speed and L_0 the outer scale of turbulence. The residual tip-tilt is treated separately from the Strehl ratio, using the same slope for its PSD.

	K	L'	N
$\langle S \rangle$	0.36	0.70	0.95
σ_S	0.063	0.044	0.008

Table 4.5: Mean value and standard deviation over 2 sec of the Strehl ratio after correction by MACAO on UT (taken from [WG03]). The seeing angle is $\alpha = 1$ arcsec.

STRAP Figure 4.15 shows the PSDs of the residual tip/tilt errors obtained using STRAP on UTs [WG03]. The data were collected during a commissioning run in early 2002. The seeing was 0.85 arcsec, the guide star magnitude $m_V = 11.2$, and the M2

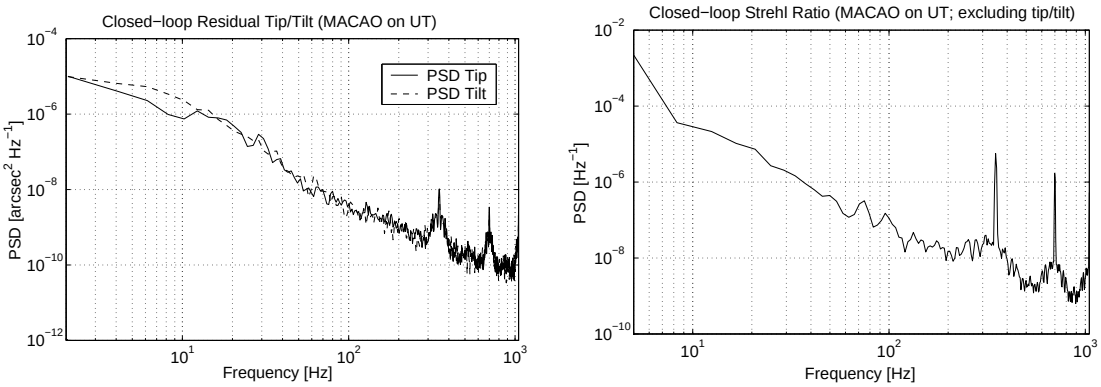

Figure 4.14: Left: PSD of the simulated residual tip/tilt on sky after closed-loop correction by MACAO. Right: PSD of the simulated Strehl ratio in the K band, excluding tip/tilt, after closed-loop correction by MACAO. Both simulations considered a bright star case ($m_V = 9$) and a typical Paranal seeing $\alpha = 1$ arcsec.

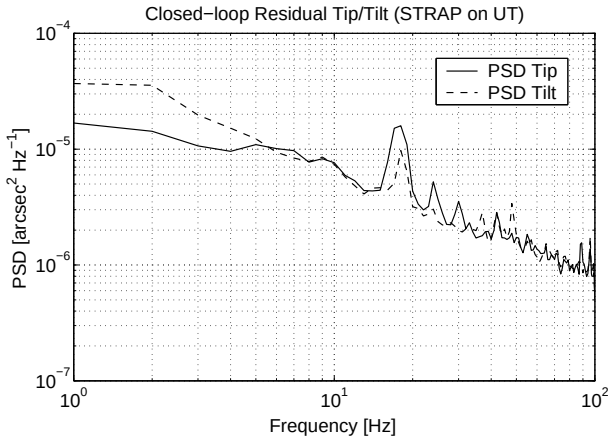

Figure 4.15: PSD of the measured residual tip/tilt (on sky) after closed-loop correction by STRAP on UT3. The seeing and guide star magnitude are $\alpha = 0.85$ arcsec and $m_V = 11.2$ respectively. Taken from [WG03].

update frequency 100 Hz. The standard deviations of the residual tip/tilt (on sky) for an exposure time of 2 sec are $\mathrm{RMS_{tip}} = 17.9$ mas and $\mathrm{RMS_{tilt}} = 18.6$ mas.

Data for STRAP on the ATs are not yet available. The actuation will probably be faster due to the smaller size of the tip/tilt mirror, but the accuracy of tip/tilt measurements coarser because of smaller focal length. Moreover, due to the smaller aperture of the ATs, the tip/tilt caused by atmospheric turbulence (prior to correction by STRAP) will be larger than for the UTs. This is because wavefront distortions tend to have larger slope changes over small scales. It is thus expected that the performances of STRAP on the ATs will be somewhat degraded with respect to UTs.

An approximate expression for the Strehl ratio after perfect correction of the tip-tilt can be found in [Nol76]:

$$S \simeq \exp\left(-0.134(D/r_0)^{5/3}\right) \ , \tag{4.13}$$

with D the telescope diameter and r_0 the Fried parameter defined in equation (4.3). Table 4.6 gives the highest Strehl ratios that can be achieved with STRAP for an AT in the K, L' and N bands and for a typical Fried parameter $r_0 = 10$ cm in the visible (500 nm).

	K	L'	N
r_0	60 cm	1.1 m	3.9 m
Strehl - AT	0.43	0.74	0.96

Table 4.6: Highest achievable Strehl ratio with STRAP, assuming perfect tip/tilt correction, under typical atmospheric conditions for Cerro Paranal.

4.2.2 The instrumental background emission

All optical surfaces in the optical train of the VLTI emit at infrared wavelengths, with a total emissivity equal to the complementary of the VLTI transmission. According to Figure 4.16, the VLTI emissivity is about 60-65% at infrared wavelengths. In practice, the emissivity has been measured for a single UT (from M1 to M3) and is about 1.4 times larger than expected (R. Wilhelm, personal communication). This discrepancy could be due to the settling of emissive dust particles on the mirrors. If the same ratio holds for the other mirrors in the optical train, the total emissivity of the VLTI should be about 90%. In the GENIE simulator, we assume a pessimistic value of 100% for the VLTI emissivity to be on the safe side.

With a mean temperature of 15°C in the VLTI delay line tunnel, we have computed the brightness of the VLTI optical train, measured at the entrance of the GENIE instrument (see Table 4.7).

4.3 Preliminary design of the GENIE instrument

4.3.1 Modal filtering with single-mode fibers

It has been shown by Ollivier and Mariotti [OM97] that high spatial frequency defects of the incoming wavefronts of a nulling interferometer would be efficiently corrected by spatial filtering, e.g. using simple pinholes. The effect of pinholes will however be less dramatic on large-scale defects such as pointing errors and low order optical aberrations.

As shown by Mennesson et al. [MOR02], the use of modal filtering (e.g. using single-mode fibers) would allow to correct for both high and low order spatial frequencies,

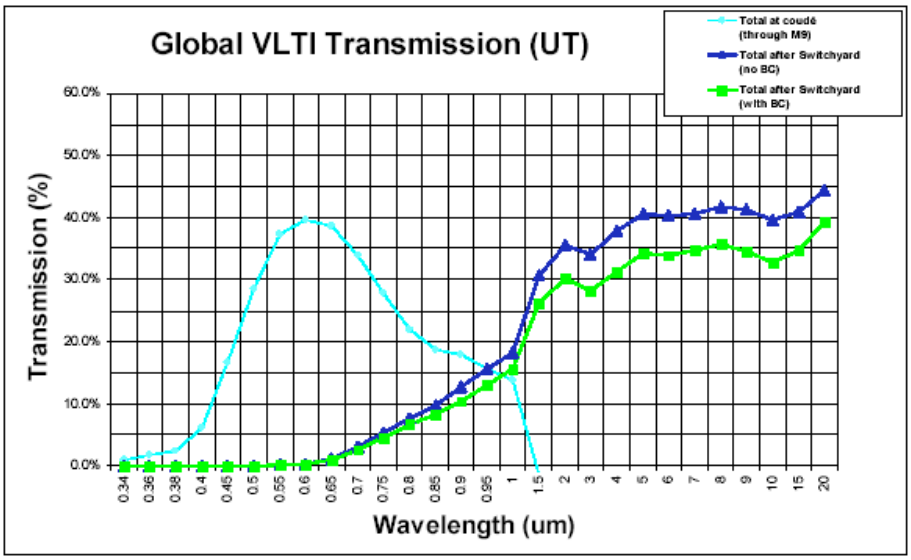

Figure 4.16: Global VLTI transmission with UTs, taken from [KG01]. The third curve (with filled squares) is relevant for GENIE.

	K	L'	M	N	N_{red}
Sky bright. [Jy/as^2]	0.004	4.2	69	599	303
VLTI bright. [Jy/as^2]	0.012	33.2	255	6985	7824
Total background [ph/s]	9.1×10^3	5.5×10^7	6.0×10^8	2.6×10^{11}	1.5×10^{11}

Table 4.7: Infrared flux of the sky computed at the entrance of the telescopes, and flux from the VLTI optical train computed at the entrance of GENIE. The fluxes are computed in Jy/as^2 at the central wavelength of the infrared atmospheric windows. The total background is given in number of photons per second at the entrance of GENIE, integrated over the field-of-view defined by the single-mode fiber. These figures are both valid for the UTs and the ATs.

thereby ensuring a perfect matching of the amplitude profiles coming from the various beams over a broad bandpass (typically an octave). The shape of the initial wavefront only affects the amount of energy coupled into the guide. The modal filter thus converts phase defects into amplitude defects, which are less severe for a nulling interferometer (see section 5.4.4). The use of single-mode fibers to filter the beams at the focus of the telescopes would therefore strongly relax the constraints on pointing accuracy and low order aberrations, and thus improve the capability to achieve deep rejection ratios. This is the reason why the preliminary design of the GENIE instrument includes infrared single-mode fibers. Such fibers are already available in the L' band, but solutions for the N band are still being investigated. Recent results obtained by Bordé and Perrin [BP03] and other teams are very encouraging.

Let us see what is the effect of atmospheric turbulence on the amount of light coupled into the waveguides. With a single-mode fiber optic placed on-axis in the focal plane of a telescope, the fraction of light injected into the fiber assuming negligible reflections is given by [SR88]:

$$\begin{aligned} \eta &= \left[\frac{1}{2}\int \left(\tilde{\mathbf{E}}_x(\mathbf{r}/\lambda f) \times \mathbf{H}_y^*(\mathbf{r}/a)\right) \cdot \hat{z}\, \mathrm{d}\mathbf{r}\right]^2 \\ &\simeq \left[\frac{1}{2}\int \tilde{E}_x(\mathbf{r}/\lambda f) H_y^*(\mathbf{r}/a)\, \mathrm{d}\mathbf{r}\right]^2 \end{aligned} \tag{4.14}$$

where $\tilde{\mathbf{E}}_x$ is the electric field transmitted by the pupil, expressed in the focal plane of the telescope, $\mathbf{H}_y$ the magnetic field vector of the LP_{01} mode of the fiber, $\hat{z}$ the direction of the wavefront, $\mathbf{r}$ the pupil coordinate, a the core radius of the fiber and f the focal length of the telescope.

An approximate expression for coupling efficiency is given by Ruilier and Cassaing [RC01]:

$$\eta \simeq \eta_0 \exp\left(-\sigma_\phi^2|_{LP_{01}}\right) , \tag{4.15}$$

where $\sigma_\phi^2|_{LP_{01}}$ is the phase variance over the pupil projected onto the LP_{01} mode of the fiber and η_0 the theoretical coupling efficiency in absence of wavefront distortion, equal to 81% for a telescope without central obstruction. In the special case of an infinitely small focal-plane filter, this approximation turns into the well-known Strehl ratio approximation with the spatial phase variance over the unweighted pupil:

$$\eta \simeq \eta_0 \exp\left(-\sigma_\phi^2\right) = \eta_0 S \tag{4.16}$$

In practice, the Strehl ratio is a pessimistic estimator of the energy coupled into the fiber [RC01].

4.3.2 GENIE end-to-end model

We will see in chapter 5 that the control subsystems available at the VLTI are generally not sufficient to meet the GENIE requirements in terms of null depth and stability. This is the reason why additional control loops will be implemented inside the GENIE instrument. In order to reduce the thermal background associated with the instrument, it is foreseen that all GENIE subsystems will be included in a cryostat as is done for MIDI, the 10-μm instrument for the VLTI [LGWP98]. A possible design for an N-band GENIE instrument is given in Figure 4.17 (the design of an L'-band GENIE would not differ much). Subsystems have been included to control for residual OPD, dispersion and intensity mismatches. In this sketch, the two movable pairs of prisms perform both the phase shifting and the real-time compensation of longitudinal dispersion due to water vapor.

Based on this preliminary design, the total transmission of the instrument can be estimated. The cryogenic GENIE optics could include the components listed in Table 4.8

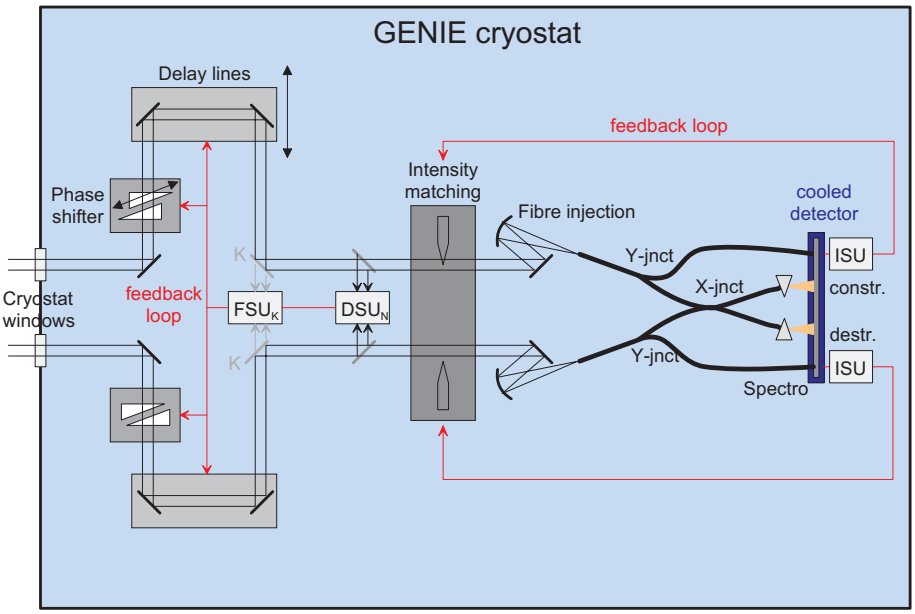

Figure 4.17: A possible design for the GENIE instrument. This scheme illustrates the operation of additional sensing units (SU) and correction systems for OPD, dispersion and intensity that could be implemented within GENIE itself. Fiber optics have been used for the clarity of the sketch. It is not proven yet that such fiber-based beam-combiners will be available in the mid-infrared at the time GENIE comes online.

(per interferometric arms up to the beam combiner). A rough guess of the range of transmission efficiency is given below for each subsystem. Assuming that both polarizations will be used, a realistic estimate of the GENIE efficiency is around 5%. This estimate is currently used in the GENIE simulator. It will be updated at the end of Phase A with the input of the industrial contractors.

Component	min	max
Entrance window	0.95	0.98
Shutter	1.00	1.00
Cold aperture stop	1.00	1.00
Parabolic mirror	0.95	0.98
Intermediate focus with cold field stop	1.00	1.00
Parabolic mirror	0.95	0.98
Polarization matching	0.45	0.90
Folding mirror	0.95	0.98
Phase shifter	0.70	0.96
Delay line	0.90	0.96
OPD control: K-band dichroïc	0.95	0.98
Dispersion control: N-band dichroïc	0.80	0.95
Intensity control system	0.90	0.99
Off-axis parabola	0.95	0.98
Coupling into modal filter	0.50	0.80
Photometric channel	0.80	0.95
Beam combiner	0.40	0.48
Spectrometer collimator mirror	0.95	0.98
Filters	0.95	0.98
Spectrometer prism, grism or grating	0.70	0.95
Spectrometer camera optics	0.70	0.90
Detector	0.60	0.80
Total efficiency	0.0064	0.17

Table 4.8: Estimation of the transmission efficiency of all components of the GENIE instrument (N-band design). All these components are assumed to stand in the GENIE cryostat to reduce the thermal background. A realistic transmission of 5% is assumed in GENIEsim.

Chapter 5

Noise sources

5.1 Shot noise

For infrared observations, the dominant source of photons is generally the huge thermal emission from the atmosphere and from the instrument itself. For example, the equivalent background flux in the interferometric field-of-view of a Unit Telescope is respectively 1 Jy and 1700 Jy in the L' and N bands, while a Sun-like star at 10 pc has a flux of 15 Jy and 2.7 Jy in these bands. The rejection rate for stellar light being generally larger than 100, the background is the dominant contributor to the detected flux. The infrared background is thus in most cases the main contributor to the shot noise associated with the Poisson statistics of incoming photons.

Let us investigate the influence of shot noise by computing the time needed to achieve a signal-to-noise ratio (SNR) of 3 on stellar leakage measurements for Sun-like stars, as a function of their distance. The expression of the stellar leakage per wavelength unit is the following (see equation (2.6)):

$$F_{\lambda,\mathrm{leak}} = A_{\mathrm{tel}} B_{\lambda,*} \frac{\pi^3 b^2 \theta_*^4}{2\lambda^2} \tag{5.1}$$

where $B_{\lambda,*}$ is the stellar brightness expressed in units of W/m^2/μm/sr. If one considers the shot noise of the background as the only noise contribution, the SNR is expressed as follows:

$$\mathrm{SNR}_{\mathrm{max}} = \frac{F_{\lambda,\mathrm{leak}} \Delta\lambda\, \Delta t}{\sqrt{F_{\lambda,\mathrm{bckg}}\, \Delta\lambda\, \Delta t}} = F_{\lambda,\mathrm{leak}} \sqrt{\frac{\Delta\lambda\, \Delta t}{F_{\lambda,\mathrm{bckg}}}} \tag{5.2}$$

where $\Delta\lambda$, Δt and $F_{\lambda,\mathrm{bckg}}$ are respectively the spectral width, integration time and background level in W/μm for the relevant spectral band. Table 5.1 gives the maximum measurable rejection rate with GENIE at 3σ level in the L' and N bands as a function of the star distance. A rejection rate of 1000 can be measured in about 10 s (resp. 20 s) in the L' band (resp. N band) on a G2 V star located at 10 pc (resp. 5 pc). To measure a rejection rate of about 4000, a G2 V star 20 pc (resp. 10 pc) away is needed in the L' band (resp. N band) and the integration time has to be longer than 35 min (resp.

85 min). This simulation assumes that the shot noise associated with the background is the only noise source. In practice, due to instrumental errors, the null depth will be degraded and the residual stellar signal larger.

	L' band - ATs (32 m)			N band - UTs (46.6 m)		
Dist.	Sig. [e^-/s]	Rej. rate	$\Delta t_{SNR=3}$ [s]	Sig. [e^-/s]	Rej. rate	$\Delta t_{SNR=3}$ [s]
5 pc	6.0×10^4	280	0.037	1.5×10^5	997	21
10 pc	3.8×10^3	1107	9.2	9.5×10^3	3848	5100
20 pc	2.5×10^2	4256	2170	6.8×10^2	13484	1.0×10^6
30 pc	5.2×10^1	8989	49000	1.6×10^2	25146	1.8×10^7

Table 5.1: Maximum measurable rejection rate with GENIE at 3σ level in the L' and N bands as a function of the star distance, for a G2V star. A Bracewell interferometer formed of two ATs (resp. UTs) is used in the L' band (resp. N band) with a baseline of 32 m (resp. 46.6 m). The thermal IR background level in the detector is 7.3×10^6 and 2.6×10^{10} e^-/s respectively in the L' and N bands.

5.2 Detector noise

In this section, we show that the detector read-out noise can also affect the performance of the instrument since a huge number of frames have to be read-out in order to recover the tiny exozodiacal dust or planetary signal from the overwhelming background contribution, especially in the N band. In order to minimize this effect, the background signal will be dispersed and the on-chip integration time increased as much as possible by operating the detector close to saturation.

5.2.1 Influence of detector noise

Assuming that the CCD electronics system is perfect and neglecting contribution related to the stellar leakage and background fluctuations, the signal-to-noise ratio that is obtained on the exozodiacal cloud when reading a single detector frame can be expressed as follows:

$$\mathrm{SNR}(1\,\mathrm{frame}) = \frac{F_{\mathrm{exo}} t_{\mathrm{f}}}{\sqrt{F_{\mathrm{tot}} t_{\mathrm{f}} + D_{\mathrm{k}} t_{\mathrm{f}} + \sigma_{\mathrm{RON}}^2}} \,, \tag{5.3}$$

where the only sources of noise that have been taken into account during the frame integration time t_{f} are:

- the shot noise associated to the total detected flux F_{tot} expressed in e^-/s,
- the read-out noise of the detector σ_{RON} expressed in RMS e^-,
- the noise on the dark current signal D_{k} expressed in e^-/s.

Among these noise sources, the photon noise associated to the thermal IR background emission B_g from the sky, the telescope and the instrument dominate all the other source of noise, including the detector dark current. The flux from the dust cloud itself is much lower than the background contribution. Therefore, equation (5.3) becomes:

$$\mathrm{SNR}(1\,\mathrm{frame}) = \frac{\sqrt{F_{\mathrm{exo}} t_{\mathrm{f}}}}{\sqrt{1 + \frac{\sigma^2_{\mathrm{RON}}}{F_{\mathrm{bckg}} t_{\mathrm{f}}}}} \tag{5.4}$$

The SNR obtained after adding n detector frames is then:

$$\mathrm{SNR}(n\,\mathrm{frames}) = \frac{\sqrt{n F_{\mathrm{exo}} t_{\mathrm{f}}}}{\sqrt{1 + \frac{\sigma^2_{\mathrm{RON}}}{F_{\mathrm{bckg}} t_{\mathrm{f}}}}} \tag{5.5}$$

Assuming that the frame read-out time is much shorter than the frame integration time (i.e., $n t_{\mathrm{f}} = T_{\mathrm{exp}} - n t_{\mathrm{RO}} \simeq T_{\mathrm{exp}}$), we find:

$$\mathrm{SNR}(n\,\mathrm{frames}) = \frac{\mathrm{SNR}_{\mathrm{shot}}}{\sqrt{1 + \frac{\sigma^2_{\mathrm{RON}}}{F_{\mathrm{bckg}} t_{\mathrm{f}}}}} \tag{5.6}$$

Hence, in order to minimize the effect of the detector read-out noise and to approach the background limited SNR, the infrared CCD detector has to operate close to saturation: $F_{\mathrm{bckg}} t_{\mathrm{f}} \simeq W$, with W the well capacity. The SNR including shot noise and detector noise then writes:

$$\mathrm{SNR}(n\,\mathrm{frames}) = \frac{\mathrm{SNR}_{\mathrm{shot}}}{\sqrt{1 + \frac{\sigma^2_{\mathrm{RON}}}{W}}} \tag{5.7}$$

The effect of detector noise thus depends on the factor $\sqrt{1 + \frac{\sigma^2_{\mathrm{RON}}}{W}}$, which divides the background-limited SNR. The effect of detector noise will thus be important only if the variance of read-out noise is of the same order than the well capacity. The characteristics of typical IR CCD detectors are presented in the next sections.

5.2.2 Infrared CCD detectors for the N band

A typical mid-IR CCD detector optimized for high-background operation is the Raytheon 320×240 Si:As Impurity Band Conduction (IBC). It has a well capacity $W = 10^7$ e$^-$ and a read-out noise $\sigma_{\mathrm{RON}} = 1000$ e$^-$ RMS, so that $(1 + \frac{\sigma^2_{\mathrm{RON}}}{W})^{1/2} \simeq 1.045$. Detector noise thus reduces the maximum achievable SNR by 5%. Here are a few other key characteristics of this detector:

- Dark current: 100 e$^-$/s
- Quantum efficiency: ∼40% in the N band

- Maximum read-out frequency: 160 Hz.

Assuming individual integration times of 100 msec[1], the background generates about 2.6×10^9 electrons in both the constructive and destructive outputs, while the well depth is only 10^7 electrons. In order not to saturate the detector, the signal has to be dispersed on at least 260 pixels, i.e., using a spectral resolution $260\lambda/\Delta\lambda = 546$. Assuming that the signal of each spectral bin is collected by a single pixel, the exozodi generates only about 30 electrons per pixel in 100 msec, while the read-out noise itself amounts to 1000 electrons.

5.2.3 Infrared CCD detectors for the L' band

Our model IR CCD detector for the L' band is the Raytheon Aladdin 1024×1024 pixel InSb array, developed for ground-based astronomy at Santa Barbara Research Center. It has a full well capacity of 3×10^5 e^- and a read-out noise of about 25 e^- RMS, so that $(1+\frac{\sigma^2_{\rm RON}}{W})^{1/2} \simeq 1.001$. The effect of read-out noise is thus negligible in the L' band. Other key characteristics are:

- Dark current: < 0.1 e^-/s
- Quantum efficiency: ∼85% in the L' band
- Maximum read-out frequency: 200 Hz

Assuming individual integration times of 100 msec, the background generates about 7.3×10^4 electrons while the well depth is of 3×10^5 electrons. It is thus not necessary to disperse the signal on several pixels with this frame rate of 10 Hz. Note that a possible problem associated with the operation of this detector in the L' band is that the same integration time and/or spectral resolution cannot be used in the constructive and destructive output at the same time. This is due to the fact that, in the constructive output, the stellar signal is about 10 times larger than the background signal. The detector full-well capacity is thus reached more rapidly in the constructive than in the destructive output. This could be a limitation to the calibration issues discussed in section 6.6.

5.3 Background fluctuations

In the N band, the infrared background flux in the interferometric FoV is almost 1000 times larger than the flux from a Sun-like star located at 10 pc. If we want to measure a null depth of one thousand on this star, the background flux has to be subtracted with an accuracy better than 1×10^{-6} in order to reveal the faint stellar leakage. In the L' band a calibration accuracy better than one percent is sufficient to measure the

[1]In practice, the choice of integration time is related to the chopping frequency.

same null depth, because in this band, the background flux is 10 times *smaller* than the stellar flux. A major limitation to achieve such calibration accuracies is the fluctuation of the background emission. Fluctuations are present in the sky emission as well as in the instrumental background, and are discussed in the two following sections.

5.3.1 Fluctuations of the sky emission

The fluctuation of the infrared background radiation produced by the atmosphere (or *sky noise*) is not well understood so far. Sky noise measurements have been carried out in the N band with the ESO 2.2-m telescope at La Silla [KBvDW01] and on top of Mauna Kea with the MICS instrument on the UKIRT [MKO$^+$00]. L'-band measurements have also been carried out at Siding Springs, Australia [AB81]. All of them conclude that the sky noise is dominant at low frequencies, increasing as a power-law of decreasing frequencies. Because of the different sites and instruments, these experiments have lead to different conclusions, presented hereafter.

5.3.1.1 N-band measurements at La Silla

According to Käufl et al. [KBvDW01], the infrared sky noise in the N band is mainly due to invisible aerosols and cirrus clouds, confined to the Earth's troposphere. Its power spectrum is proportional to $1/f$ at low frequencies. This power-law had already been measured by several authors (see [KBvDW01]). It is proven that this power spectrum does not much depend on the telescope diameter. The $1/f$ component of the sky noise reaches the level of the white shot noise component associated with the background emission for a frequency of about 5-8 Hz (see Figure 5.1). Käufl thus recommends to use a chopping frequency of 8 Hz in order to reach background-limited performances[2]. He also recommends to use a chopping throw < 10 arcsec so that the shape of the amplitude spectrum does not change during chopping. For larger chopping throws, the spatial correlation of the background fluctuations is not ensured.

5.3.1.2 N-band measurements at Mauna Kea

Miyata et al. [MKO$^+$00] have used the Mid-Infrared Camera and Spectrometer on the UKIRT to measure the sky noise under good sky conditions, and concluded that the power-law index varies between -1 and -2.5 across the whole N band, with a mean of about -1.8. The frequency at which the sky noise reaches the level of shot noise is about 0.5 Hz according to their measurements. The spectroscopic capability of the instrument also allowed them to conclude that sky noise has a strong excess at the positions of atmospheric water vapor lines (7.882, 8.170, 11.722 and 12.522 μm). A chopper throw of 10.8 arcsec was used. Based on these measurements, Miyata recommends a chopping

[2]The background-limited performance (BLIP) regime is reached when the chopping frequency is high enough so that the residual noise due to imperfect background subtraction is smaller than the shot noise associated with the background flux.

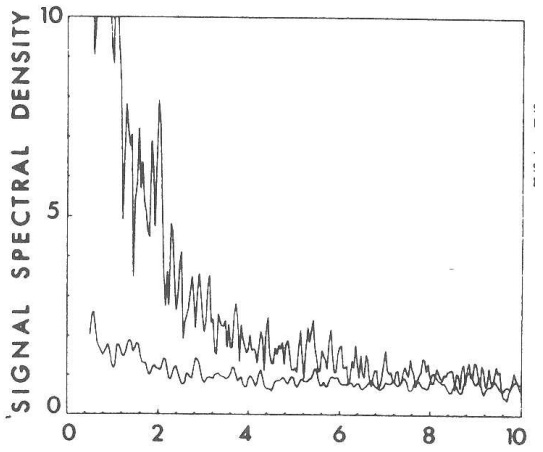

Figure 5.1: Average of amplitude spectrum of the sky radiance fluctuations as a function of frequency (in Hz) observed at zenith in the 10 μm atmospheric window at La Silla, with the ESO 2.2-m telescope [KBvDW01]. The upper trace is the actual sky spectrum, the lower trace the reference measurement of the bolometer noise (measured with mirror cover closed). Only above 5-8 Hz the sky noise approaches the bolometer shot noise.

frequency higher than 0.5 Hz. This value, about 10 times smaller than that measured by Käufl, may be attributed to the better sky conditions, to the higher altitude of the observing site or to a larger instrumental noise (the shot noise level might be higher than in Käufl's measurements).

5.3.1.3 L'-band measurements at Siding Springs

Measurements have been carried out in the L' band by Allen et al. [AB81] with the 3.9-m Anglo-Australian Telescope at Siding Spring Mountain. This site is moist by infrared standards, and experiences large variations in precipitable water vapor content. In these data, about 75% of the background flux is due to the telescope, which is expected to be more thermally stable than the atmosphere. The measurements, displayed in Figure 5.2, show that the sky noise reaches the shot noise level for a chopping frequency of about 0.3 Hz. The slope of the square root power spectrum is about -1.3.

5.3.1.4 Conclusions

Based on all these measurements, it is obvious that the infrared emission greatly depends on the astronomical site (altitude, humidity, ...), on the sky conditions at the moment of the observation and on the instrument itself, because it contributes to a great extent to the infrared background. Measurements of the sky noise at Cerro Paranal are thus the only way to build a reliable model for the sky fluctuation spectrum. A measurement campaign is currently undertaken at the VLTI with the MIDI instrument, in order to

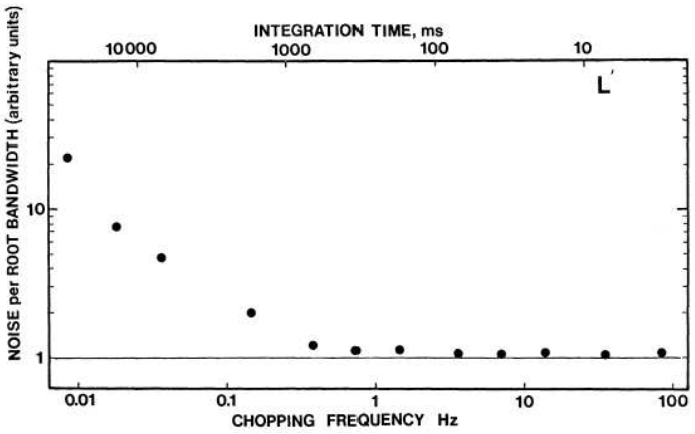

Figure 5.2: Sky noise diagram in the L' band. The straight line indicates the level of shot noise. Taken from [AB81].

characterize the thermal background fluctuations for both the sky and the VLTI. In order to record the fluctuations of the sky and the instrument separately, a series of experiments has been planned, including observations of a black screen source on the MIDI table, of a blackbody source through the delay line, of the closed dome through a UT and of the sky with various instrumental set-ups. Preliminary results obtained in photometric mode (with only one UT) show a power-law behaviour similar to previous measurements. Data are currently being processed.

5.3.2 Fluctuations of the instrumental emission

The main contributors to fluctuations of the instrumental emission are temporal as well as spatial variations of temperature and vibrations in mechanical systems (especially in closed-cycle coolers, folding mirrors and in the delay lines). With respect to these two criteria, the VLTI is probably the best-designed interferometer currently in activity:

- The thermal environment of the VLTI has been designed to stay as stable as possible. The heat dissipated inside the interferometric lab by each instrument does not exceed 10 W, while the convected cooling load does not exceed −20 W. The mean temperature is 15.5°C, with a diurnal variation less than 0.1°C peak-to-valley and a spatial homogeneity over the whole lab better than 0.22°C peak-to-valley. Moreover, access to the lab is avoided 2 hours before an observation to maintain adequate environmental conditions.

- All instruments, including cryo-coolers, have been designed to reduce mechanical vibrations as much as possible. Indeed, the preliminary data on background fluctuations discussed in section 5.3.1.4 still show some peaks in the power spectral densities associated with the closed cycle cooler (1 Hz), with the STRAP tip/tilt

corrector (18 Hz) and with the electrical network (50 Hz), whose influence on the background stability has to be assessed (E. Bakker, personal communication).

The current assumption used in GENIEsim is that the instrumental fluctuations are negligible as compared to the sky fluctuations. This assumption will be revised as soon as data become available.

5.4 Stellar transmission noise

5.4.1 Physical and instrumental leakage

The stellar leakage can be divided into two components:

- The *physical leakage*, which is only due to the finite extent of the stellar disk. This is also the smallest possible leakage that GENIE would reach if there were no instrumental error.
- The *instrumental leakage*, which adds to the physical leakage, is due the instrumental imperfections including residual OPD, longitudinal dispersion, intensity mismatches, polarization errors, ...

The predominance of one or the other leakage source depends on the target star and on the observation parameters. We may expect that, for a nearby star observed in the N band with a rather large baseline, stellar leakage will be dominated by the physical leakage, while being dominated by instrumental leakage for a distant star observed in the L' band with a small baseline. We have seen in Tables 2.2 and 2.3 (page 20) that the physical rejection rate is of the order of 500 in the L' band and of 3000 in the N band for our reference target (Sun-like star at 10 pc). On the other hand, the flux ratio for typical circumstellar disks and hot Jupiters is of the order of 10000 in the L' band and of 1000 in the N band. The physical leakage will thus be an important contributor to the signal detected at the destructive output of the beam-combiner, especially in the L' band. In order to detect and characterize faint circumstellar environments, a precise calibration of the physical stellar leakage is thus needed. Methods for precise stellar leakage calibration are presented in section 6.6. The residual stellar leakage after calibration will be an important source of noise for GENIE.

In GENIEsim, stellar leakage is computed as a 2-D integral of the transmission map over the stellar disk. All instrumental errors are computed at the milli-second level and included analytically in the expression of the interferometric response (see equation (2.2)):

$$R(\theta,\phi) = \left| \sum_{k=1}^{n} (A_k + \Delta A_k) e^{j2\pi(L_k\theta/\lambda)\cos(\delta_k-\phi)}\, e^{j(\phi_k+\Delta\phi_k)} \right|^2 , \tag{5.8}$$

where A_k and $A_k + \Delta A_k$ are respectively the mean and instantaneous beam amplitudes for telescope k, and $\Delta\phi_k$ the instantaneous error on the phase of beam k. Due to the

fluctuations of instrumental errors, stellar leakage varies with time in an erratic way, leading to an important noise contribution called transmission noise.

5.4.2 Transmission noise

In addition to the noise associated with imperfect calibration, stellar leakage also contributes to the total noise through its fluctuations. This noise can be divided into two parts: the photon noise associated with the mean stellar leakage, and the so-called transmission noise associated with the rapid fluctuations of the stellar transmission τ due to random instrumental errors. Stellar leakage can be considered as a doubly stochastic Poisson process since the photon arrival rate (proportional to τ) is itself a random variable. Goodman [Goo85] fully discusses the statistics of doubly stochastic Poisson processes. Letting $\langle K \rangle$ be the mean number of photo-events detected during the integration time t_{int}, and $W = \int_{t_{int}} I(\zeta) \mathrm{d}\zeta$ the integrated intensity during t_{int}, the mean and variance of K are found to be

$$\langle K \rangle = \alpha \langle W \rangle \quad \text{and} \quad \sigma_K = \alpha \langle W \rangle + \alpha^2 \sigma_W^2 \,, \tag{5.9}$$

where $\alpha \propto 1/h\nu$ is a constant relating the mean number of photo-counts $\langle K \rangle$ at the detector to the mean incoming energy $\langle W \rangle$. The variance σ_K^2 of K thus consists of two distinct terms, each of which has a physical interpretation. The first one, which is proportional to the total energy incident during the measurement, can be interpreted as pure Poisson noise. The second one, because it is proportional to σ_W^2 (variance of the incident intensity between successive integration times), is the classically expected result in the absence of shot noise. This expression proves that the transmission noise can be computed separately from the photon noise associated with the stellar leakage.

An analytical expression relating transmission noise to the RMS instrumental errors cannot be found if one does not make restrictive assumptions. Such an expression has been derived by Ph. Gondoin [Gon02] in the case of a Bracewell interferometer, and seems to generally give satisfactory results. The only way to compute transmission noise accurately is the numerical way. In GENIEsim, transmission noise is computed in real-time, through the analytical expression of the transmission map which takes into account all instrumental errors. We will see in chapter 6 that transmission noise has an important contribution in the L' band, while it is generally surpassed by shot noise in the N band.

5.4.3 Influence of OPD errors

The effect of differential OPD between the beams is to make the dark fringe move around its central position. The fringe motion is illustrated in Figure 5.3. Its effect is two-fold: it increases the mean stellar transmission (as shown on the right-hand side of Figure 5.3) and introduces transmission noise.

In order to evaluate the influence of OPD errors on the mean stellar leakage, we will derive an analytical expression of the stellar transmission as a function of OPD error

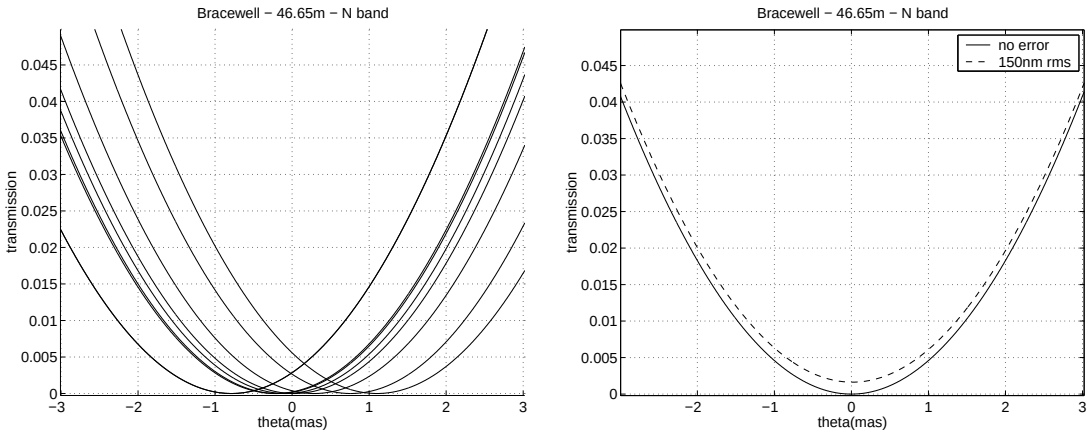

Figure 5.3: Left: The central fringe moves around the centre of the field-of-view as a result of OPD fluctuations. The size of the stellar disk is about 0.5 mas in radius for a 10 pc Sun-like star. Right: Mean transmission, averaged on 100 random values of the differential OPD (with RMS = 150 nm).

for a Bracewell interferometer. Denoting ε_φ the phase error between the two beams, equation (2.1) becomes:

$$T(\theta,\phi) = \frac{1}{2}\left(\frac{2J_1(\pi\theta D/\lambda)}{\pi\theta D/\lambda}\right)^2 \left|\exp\left(j\pi\tfrac{b\theta}{\lambda}\cos\phi + j\varepsilon_\varphi\right) - \exp\left(-j\pi\tfrac{b\theta}{\lambda}\cos\phi\right)\right|^2 \qquad (5.10)$$

For small values of $b\theta/\lambda$ (i.e., close to the optical axis), the transmission map writes:

$$\begin{aligned} T(\theta,\phi) &\simeq 2\sin^2\left(\pi\frac{b\theta}{\lambda}\cos\phi + \frac{\varepsilon_\varphi}{2}\right) \\ &\simeq 2\pi^2\frac{b^2\theta^2}{\lambda^2}\cos^2\phi + 2\pi\varepsilon_\varphi\frac{b\theta}{\lambda}\cos\phi + \frac{\varepsilon_\varphi^2}{2} \end{aligned} \qquad (5.11)$$

Integrating this expression on θ and ϕ and using the same reasoning as in section 2.2, one gets the following expression for the stellar transmission:

$$\tau = \frac{\pi b^2\theta_*^2}{4\lambda^2} + \frac{\varepsilon_\varphi^2}{4}\,, \qquad (5.12)$$

where the first term is the theoretical stellar transmission (see equation (2.8)) and the second term the additional transmission due to the phase error. Atmospheric turbulence induces phase errors between the beams of an interferometer because of piston and longitudinal dispersion. The adaptive optics system and the fiber-coupling process can also produce fluctuations in the OPD. Let us evaluate the influence of these effects on the stellar transmission.

5.4.3.1 Atmospheric piston

Piston is highly variable with time, with a zero mean and a typical standard deviation of 20 μm RMS for a 40 m baseline. In the N band, an OPD variation of 5 μm would be sufficient to get a constructive interference instead of a destructive one, and therefore, the differential OPD must be controlled. Thanks to the fringe tracking facility of the VLTI (PRIMA/FINITO), this OPD error will be reduced to about 150 nm RMS at the entrance of GENIE. This corresponds to 0.25 radians RMS in the L' band, or 0.09 radians RMS in the N band. According to Table 5.2, the associated instrumental transmission is at least 10 times larger than the theoretical transmission for a Sun-like star at 10 pc! The rejection rate reduces to about 60 in the L' band and 500 in the N band, which is not acceptable.

	L' band	N band
σ_{piston}	150 nm	150 nm
τ_{inst}	0.015	0.002
τ_{phys}	5.4×10^{-4}	2.8×10^{-4}
Rej. rate	60	500

Table 5.2: Instrumental and theoretical stellar transmission for the observation of a Sun-like star at 10 pc with a 25 m baseline in the L' band and a 50 m baseline in the N band respectively, assuming an OPD error of 150 nm RMS. The rejection rate is completely dominated by instrumental errors, especially in the L' band.

In order to reduce the instrumental transmission to the level of the theoretical one, an OPD error of less than 28 nm RMS in the L' band and 56 nm RMS in the N band is required. This level of OPD stability is challenging, but certainly not impossible (see section 6.2) with a fast delay line. Indeed, the main limitation to the performance of the VLTI fringe tracking system is the limited bandwidth of the delay line response which drops from 200 Hz onwards (Figure 4.11). A fast delay line with associated fringe sensing unit could be integrated within GENIE to overcome this problem.

5.4.3.2 Longitudinal dispersion

Longitudinal dispersion has two potentially disastrous consequences for GENIE (Figure 5.4). First, it induces a wavelength dependence of the optical path difference across the observational band (*intra-band* dispersion) because the refractive index of water vapor itself depends on the wavelength (see Figure 4.4). Second, *inter-band* dispersion is an even more serious problem. In IR interferometry, OPD control is most likely limited to the K band because fringe tracking requires sufficient photons per millisecond. This means that an L'-band or N-band null should be maintained with K-band fringe tracking, which is not possible because fringe motions in the K band underestimate phase

offsets due to longitudinal dispersion in the N band, as shown in Figure 4.6. Let us evaluate the influence of these two effects on the achievable rejection rate.

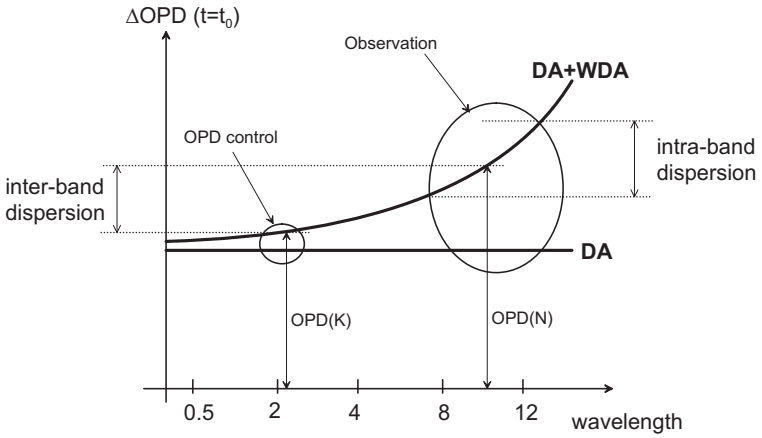

Figure 5.4: Illustration of inter- and intra-band dispersion in the case of N-band observations.

Intra-band dispersion The expression of the dispersion induced by water-vapor across the observation waveband (denoted X) is derived from equation (4.7):

$$\sigma_{\mathrm{disp,100s}}(\text{X band}) = \frac{2\pi c}{\lambda_{\mathrm{X,cen}}} \left(\hat{n}_{\mathrm{WDA}}(\lambda_{\mathrm{X,min}}) - \hat{n}_{\mathrm{WDA}}(\lambda_{\mathrm{X,max}})\right) \sigma_{\Sigma,\mathrm{100s}} \,, \tag{5.13}$$

where $\lambda_{\mathrm{X,min}}$, $\lambda_{\mathrm{X,cen}}$ and $\lambda_{\mathrm{X,max}}$ are respectively the minimum, center and maximum wavelengths in band X. Table 5.3 summarizes the amount of water vapor-induced dispersion across the possible wavebands of GENIE, together with their influence on the stellar transmission and null depth. The OPD error is supposed to be zero at the center of the observation waveband. This table shows that a subsystem dedicated to intra-band dispersion control is mandatory for GENIE. In order to reduce the instrumental transmission to 10^{-4}, intra-band dispersion must be reduced to 0.04 rad RMS.

Inter-band dispersion In order to compute the effect of inter-band dispersion, let us assume that the K-band fringes are perfectly locked at zero OPD by the VLTI fringe tracking system. The additional OPD induced in other bands by inter-band dispersion can then be computed as:

$$\sigma_{\mathrm{disp,100s}}(\lambda - \lambda_{\mathrm{K}}) = \frac{2\pi c}{\lambda} \left(\hat{n}_{\mathrm{WDA}}(\lambda) - \hat{n}_{\mathrm{WDA}}(\lambda_{\mathrm{K}})\right) \sigma_{\Sigma,\mathrm{100s}} \,, \tag{5.14}$$

where λ_{K} is the center wavelength of the K band. The effect of inter-band dispersion on the rejection rate is summarized in Table 5.4. This table shows that a subsystem

	L' band	N band	N_{red} band
$\sigma_{disp,100s}$(band)	0.31 rad	1.9 rad	0.89 rad
τ_{inst}	0.006	0.23	0.05
τ_{phys}	5.4×10^{-4}	2.8×10^{-4}	2.5×10^{-4}
Rej. rate	166	4.4	20

Table 5.3: Instrumental and theoretical stellar transmission for the observation of a Sun-like star at 10 pc with a 25 m baseline in the L' band and a 50 m baseline in the N band respectively, taking intra-band dispersion into account. The rejection rate is completely dominated by instrumental errors, especially in the N band which has a large bandwidth and experiences large variations of the water-vapor refractive index (see Figure 4.4).

dedicated to inter-band dispersion control is mandatory for GENIE. In order to reduce the instrumental transmission to 10^{-4}, intra-band dispersion must be reduced to 0.02 rad RMS.

	L' band	N band	N_{red} band
$\sigma_{disp,100s}(\lambda - \lambda_K)$	0.35 rad	1.3 rad	1.5 rad
τ_{inst}	0.03	0.42	0.56
τ_{phys}	5.4×10^{-4}	2.8×10^{-4}	2.5×10^{-4}
Rej. rate	32	2.3	1.8

Table 5.4: Instrumental and theoretical stellar transmission for the observation of a Sun-like star at 10 pc with a 25 m baseline in the L' band and a 50 m baseline in the N band respectively, taking inter-band dispersion into account. The rejection rate is completely dominated by instrumental errors, especially in the N band where water-vapor dispersion is large (see Figure 4.4).

5.4.3.3 Additional piston due to AO and fiber coupling

When using adaptive optics in stellar interferometry, the control of the piston mode of the deformable mirror (DM) is a critical issue (see [VC01]). Indeed, the DM could add high-frequency OPD fluctuations to the atmospheric piston, which are difficult to correct with the VLTI fringe sensing unit because of its limited bandwidth. However, filtering of the piston mode can be achieved by the AO system without any significant additional computing time [VC01]. In the current implementation of GENIEsim, we assume that both MACAO and STRAP can be tuned to deliver a piston-free AO correction, so that AO-induced OPD fluctuations can be neglected. This assumption will be revised when real data become available. In any case, the possible influence of AO-induced OPD reinforces the need for high-frequency OPD control within GENIE.

In addition to the OPD induced by the adaptive optics system, the coupling into the fiber itself may produce an additional OPD through the effect of high-order optical aberrations [RC01]. In particular, defocus and spherical aberrations contribute to OPD errors, with a typical RMS of 10 nm according to Ruilier [RC01]. In order to remove this small (but non negligible) contribution, the fringe tracker should measure the same piston as the scientific instrument, and therefore use similar spatial filtering. This could be achieved with an L' band GENIE and K band fringe tracking, provided that coupling-induced piston is not too chromatic, since single-mode fibers can be used simultaneously in the K and L' band. On the other hand, if GENIE operates in the N band, correction of coupling-induced OPD seems a priori impossible. However, operation in the N band can afford an OPD error of 10 nm.

5.4.4 Influence of intensity mismatches

The effect of unequal intensities in the two arms of the interferometer is to induce a non-null transmission on the axis. In fact, the whole transmission curve is raised, as shown in Figure 5.5. To produce this figure, we have only taken Strehl fluctuations into account, using the simulated performances of the MACAO-VLTI simulator, i.e., a Strehl of 0.36 in the K band with an RMS of 0.063 (see Table 4.5).

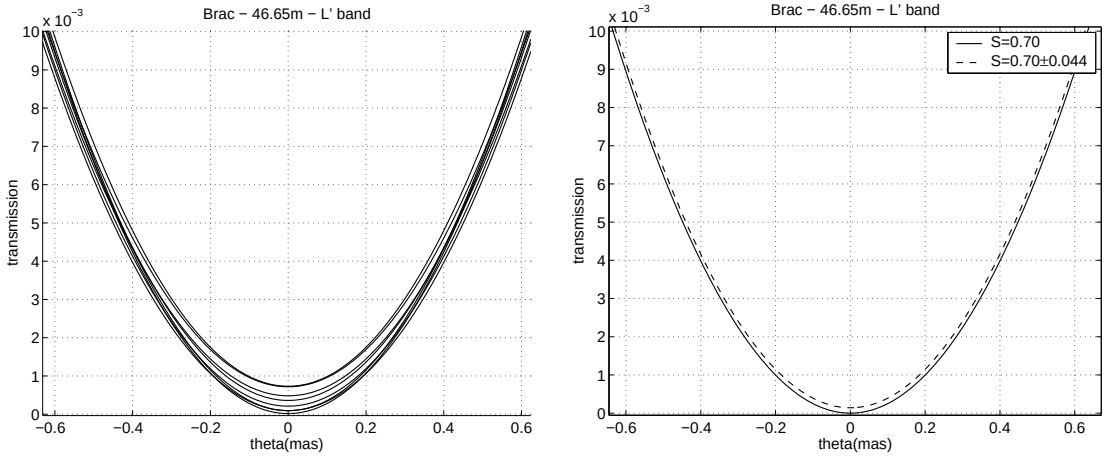

Figure 5.5: Left: Movement of the central fringe as a result of Strehl fluctuations. The size of the stellar disk is about 0.5 mas in radius for a 10 pc Sun-like star. Right: Mean transmission, averaged over 100 random values of the Strehl, compared to the "ideal" transmission curve obtained with the average Strehl in the two arms. The specified K-band Strehl of 0.36 with an RMS of 0.063 is equivalent to an L'-band Strehl of 0.70 with an RMS of 0.044.

In order to evaluate the influence of intensity mismatches on the mean stellar transmission, let us write the signal at the output of a two-telescope interferometer under the

following form:

$$I = \frac{1}{2}\left(I_1 + I_2 + 2\sqrt{I_1 I_2}\cos(\varphi_2 - \varphi_1)\right) \tag{5.15}$$

with I_1 and I_2 the intensities of the two beams and with $\varphi_2 - \varphi_1 = \pi$ for a nulling interferometer as GENIE. The factor 1/2 is due to the fact that only one half of the intensity is sent to one particular output of the beam-combiner. Letting $I_1 = I_0$ and $I_2 = I_0(1+\varepsilon)$ with ε the relative intensity error, a development in series of ε to the 2^{nd} order gives:

$$I_{\text{null}} = I_0(1 + \frac{\varepsilon}{2}) - I_0(1+\varepsilon)^{1/2} = 2I_0\frac{\varepsilon^2}{16}\ . \tag{5.16}$$

Since $2I_0$ represents the total intensity collected by the two telescopes, the on-axis transmission is equal to $\varepsilon^2/16$. Intensity mismatches in the arms of the interferometer are due to two main sources: Strehl fluctuations (including tip/tilt) at the output of the adaptive optics system (MACAO or STRAP) and scintillation. Let us evaluate their influence on the achievable rejection rate.

5.4.4.1 Fluctuations of the coupling efficiency

If scintillation is neglected, the intensities in the two arms of the interferometer are both equal to I_0 before the injection into the fibers. We have seen in section 4.3.1 that the intensity coupled into single-mode fibers is approximately proportional to the Strehl ratio (including tip/tilt). The relative intensity mismatches between the two beams will thus be of the order $2\sigma_S/\langle S\rangle$, because fluctuations of the Strehl with an RMS of σ_S are present in the two beams. This expression assumes that there is no correlation between the fluctuations of the Strehl ratio in the two beams, which is probably not the case in practice. This is thus a pessimistic assumption that will be refined when data become available with STRAP and MACAO.

MACAO Both the tip/tilt error and the Strehl ratio excluding tip/tilt have an influence on the amount of light coupled into the single-mode fiber. We have an approximate relation between the Strehl and the coupling fluctuations thanks to equation (4.16). On the other hand, an analytical relation between the tip/tilt and the coupling fluctuations is not easy to derive. We have computed numerically the coupling efficiency as a function of tip/tilt error to derive the figures of Table 5.5. This table shows that, in the N band, the instrumental stellar transmission is smaller than the theoretical transmission, suggesting that intensity matching is not required. On the other hand, intensity matching is recommended in the L' band because the instrumental leakage exceeds the theoretical leakage.

STRAP The wavefront correction achieved by STRAP only concerns the tip/tilt error. All high-order aberrations are left unaffected. Assuming that the tip/tilt is perfectly

	L' band		N band	
	tip/tilt	Strehl	tip/tilt	Strehl
RMS	15 mas	0.044	15 mas	0.008
$2\sigma_I/I$	0.105	0.126	0.015	0.017
τ_{inst}	6.9×10^{-4}	9.9×10^{-4}	1.4×10^{-5}	1.8×10^{-5}
τ_{phys}	5.4×10^{-4}	5.4×10^{-4}	2.8×10^{-4}	2.8×10^{-4}
Rej. rate	813	655	3350	3305

Table 5.5: Instrumental and theoretical stellar transmission for the observation of a Sun-like star at 10 pc with a 25 m baseline in the L' band and a 50 m baseline in the N band respectively, taking into account intensity mismatches produced by tip/tilt and "Strehl-excluding-tip/tilt" fluctuations in the case of a UT+MACAO. The RMS intensity fluctuation is computed numerically by GENIEsim for tip/tilt errors, and using the approximation of equation (4.16) for Strehl fluctuations.

corrected, an expression of the fluctuations of the coupling efficiency η has been derived by [RC01]:

$$\frac{\sigma_\eta}{\langle\eta\rangle} \simeq 0.408\,\sigma_\phi^2\,, \tag{5.17}$$

with the residual wavefront error given by:

$$\sigma_\phi^2 \simeq 0.145\left(\frac{D}{r_0}\right)^{5/3}\,. \tag{5.18}$$

In addition to these fluctuations of coupling efficiency, the residual tip/tilt after correction by STRAP must be added. Data is not yet available for the ATs, but the RMS tip/tilt is expected to be of the order of 18 mas, as is the case for STRAP on the UTs. The resulting instrumental transmissions are given in Table 5.6 for an AT in the L' and N bands, showing that intensity matching is required. Note that tip/tilt errors have a much less severe effect on ATs than on UTs, because the acceptance cone of the fiber is larger. However, it is not proven yet that STRAP can reach a residual tip/tilt of 18 mas with the ATs (the residual tip/tilt is expected to be larger, see section 4.2.1.3).

5.4.4.2 Scintillation

We have proven is section 4.1.2.4 that scintillation is completely dominated by Strehl fluctuations, at low as well as high frequencies. Therefore, scintillation will not degrade the nulling ratio nor increase transmission noise significantly.

5.4.5 Influence of polarization errors

The polarization errors that GENIE will encounter are of two types: differential phase shift between the two polarization components s and p, and differential rotation between

	L' band		N band	
	tip/tilt	Strehl	tip/tilt	Strehl
RMS	18 mas	0.099	18 mas	0.016
$2\sigma_I/I$	0.008	0.27	0.001	0.033
τ_{inst}	4.1×10^{-6}	4.5×10^{-3}	6.7×10^{-8}	6.6×10^{-5}
τ_{phys}	5.4×10^{-4}	5.4×10^{-4}	2.8×10^{-4}	2.8×10^{-4}
Rej. rate	1826	198	3512	2847

Table 5.6: Instrumental and theoretical stellar transmission for the observation of a Sun-like star at 10 pc with a 25 m baseline in the L' band and a 50 m baseline in the N band respectively, taking into account intensity mismatches produced by tip/tilt and "Strehl-excluding-tip/tilt" fluctuations in the case of an AT+STRAP. The RMS intensity fluctuation is computed numerically by GENIEsim for tip/tilt errors, and using the approximation of equation (4.16) for Strehl fluctuations.

the two beams for an individual polarization component. These effects can be translated into OPD and intensity errors, as shown in the following sections. But unlike OPD and intensity errors due to turbulence, these errors are assumed to be static, or slow functions of time. It is thus expected that a precise tuning of the instrument during its commissioning phase, possibly repeated a few times during the instrument lifetime, could be sufficient to make polarization errors negligible. GENIEsim currently assumes that polarization errors are negligible. Let us compute the polarization errors that can be tolerated to validate this assumption.

5.4.5.1 Differential phase shift

A differential phase shift between the two components of unpolarized light has the effect to shift the two fringe patterns with respect to each other. If the phase shift between the two arms of the interferometer is π for the first polarization, it is $\pi + \varepsilon_\varphi$ for the other one. According to equation (5.12), the instrumental transmission associated with this effect is $\varepsilon_\varphi^2/8$, since it is null for the first polarization and equal to $\varepsilon_\varphi^2/4$ for the second one. In order to keep the instrumental transmission smaller than 10^{-4}, the differential phase shift between the two polarizations must be smaller than 0.028 radian (equivalent to 17 nm in the L' band or 47 nm in the N band).

For the VLTI, the differential polarization effects are limited by the use of a symmetrical design, which means the same succession of incidence angles and the same coating type in every beam. The remaining source of differential effect is differential coating characteristics due to manufacturing errors and due to aging. These are also limited by the choice of simple coatings (except for M9 dichroïc) and by performing (as far as possible) the coating of the various pairs of mirrors simultaneously in the same coating chamber. The current estimates for differential linear retardation between the two polarizations is < 0.087 radian in the N band and < 0.17 radian in the K band [KG01],

which translate into instrumental transmissions of $< 9.5 \times 10^{-4}$ and $< 3.8 \times 10^{-3}$ respectively. It is expected that fine tuning of the GENIE instrument during commissioning could be sufficient to reduce these values down to the required accuracy of 0.028 radian.

5.4.5.2 Differential rotation

Differential rotation between the two beams of the interferometer may happen for a polarization component of natural light. Let us consider only one polarization component in the following reasoning. The destructive recombination of the two non-coplanar polarized waves can be seen as the recombination of a first wave with amplitude A and a second one with amplitude $A \cos \varepsilon_\theta$, ε_θ being the differential rotation between the two beams (see Olliver [Oll99]). Differential rotation thus translates into an intensity mismatch. Assuming ε_θ to be a small quantity, the instrumental transmission is equal to ε_θ^4 as proven by Ollivier [Oll99]. In order to keep the instrumental transmission below 10^{-4}, the differential rotation should be smaller than 0.1 radian. The effect of rotation of the polarization frame of reference will be completely negligible in the case of the VLTI thanks to its highly symmetric design [KG01].

Chapter 6

Correction of atmospheric effects

We have shown in the previous chapter that the performances of the VLTI subsystems generally do not meet the GENIE requirements. This is especially the case for OPD and dispersion control, and to a lesser extent for intensity control. It is thus mandatory to add dedicated control systems within the GENIE instrument. Their objective is twofold: decrease the mean instrumental transmission down to the required 10^{-3} (goal: 10^{-4}), and reduce transmission noise as much as possible (goal: below the unavoidable shot noise associated with the background). In this chapter, we investigate the preliminary design of optimized control systems and evaluate their expected performance.

6.1 General scheme for a control loop

Figure 6.1 represents the block-diagram of a general control loop. The input signal that has to be corrected is characterized by its Power Spectral Density (PSD) $S_{\rm in}$. A Sensing Unit (SU) measures the signal during an integration time T_i. A certain amount of noise is produced by the detection: photon noise and detector read-out noise are the major contributions to the PSD $S_{\rm SU}$ of the detection noise. The value measured by the Sensing Unit is then fed into a Controller, which computes the correction to be applied. This process is supposed to be noise-free. The Actuator finally applies the relevant correction to the input signal in order to compensate for the error. The actuation is not perfect; this is the reason why an amount of noise is added to the correction signal. The PSD of this noise source depends on the design of the actuator and will be neglected in the following discussion because data are not yet available. It is not expected to be the dominant noise source (as in the case of VLTI fringe tracking, see Table 4.4).

6.1.1 Closed loop transfer function

We denote respectively by $H_{\rm SU}$, $H_{\rm C}$ and $H_{\rm A}$ the transfer functions of the Sensing Unit, the Controller and the Actuator. The global transfer function of the control loop

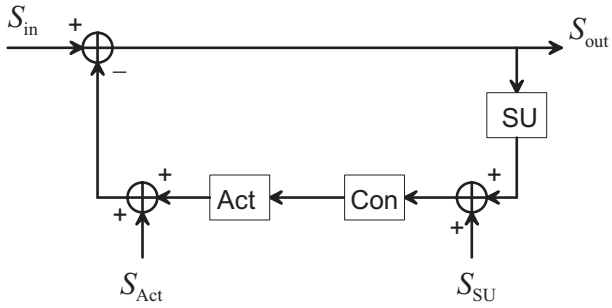

Figure 6.1: General scheme for a control loop.

writes [MG01]:

$$H(s) = \frac{1}{1 + H_{\rm SU}(s)H_{\rm C}(s)H_{\rm A}(s)} \tag{6.1}$$

where s denotes the Laplace variable. The Sensing Unit is modeled by assuming that it averages the input signal over the integration time T_i, and holds the value during the next T_i time interval. The SU transfer function then writes [MG01]:

$$H_{\rm SU}(s) = \frac{1 - e^{sT_i}}{sT_i} \Rightarrow H_{\rm SU}(j2\pi f) = \mathrm{sinc}(fT_i)e^{-j2\pi T_i} \tag{6.2}$$

In the following discussion, the Controller is assumed to be a simple integrator ($H_{\rm C} = K/s$) and the Actuator to be an ideal transducer[1] ($H_{\rm A} = 1$). The close loop transfer function thus writes:

$$H(s) = \frac{s}{s + Ke^{-sT_i/2}} \tag{6.3}$$

The only remaining unknowns in Figure 6.1 are $S_{\rm SU}$ and $S_{\rm A}$. As mentioned above, we will not try to compute $S_{\rm A}$, unless data are already available (as for the VLT delay lines). Let us show how to evaluate the PSD of the Sensing Unit noise (detection noise).

6.1.2 Detection noise

In order to retrieve the relevant physical quantity (OPD, intensity, dispersion, ...), a flux is measured by the Sensing Unit an appropriate number of times using an appropriate instrumental set-up. For example, intensity measurements only need a single detection of the flux in the whole spectral band, while OPD measurements by means of the ABCD method (see below) require the measurement of the flux at four different phases in the fringe pattern (offset by $\pi/2$). The variance σ of the desired physical quantity depends on the noise encountered during the measurement. In our case, the main contributors are

[1]This assumption implies that the cut-off frequency in the actuator's transfer function is well above the maximum repetition frequency of the control loop. This is a rather crude assumption, which should be revised as soon as a preliminary design of the actuator is available.

photon noise and read-out noise. These noise sources have white spectra, respectively denoted S_{phn} and S_{ron}, so that the output noise power of the Sensing Unit writes [MG01]:

$$S_{\text{SU}}(f) = S_0 \text{sinc}^2(fT_i) \tag{6.4}$$

where $S_0 = S_{\text{phn}} + S_{\text{ron}}$ is the sum of the photon noise and read-out noise PSDs. In order to determine the value of S_0, we use the fact that the integral of the noise PSD amounts to the variance of the physical quantity:

$$\int_{-\infty}^{+\infty} S_{\text{SU}}(f)\,\mathrm{d}f = \sigma^2 \ , \tag{6.5}$$

which implies that

$$S_0 = \sigma^2 \frac{1}{\int_{-\infty}^{+\infty} \text{sinc}^2(fT_i)\,\mathrm{d}f} = \sigma^2 T_i \ . \tag{6.6}$$

This equation shows that the PSD of detection noise is directly related to the variance σ^2 of the noise produced by the detection process. The value of σ^2 depends on the physical quantity that is measured. The repetition frequency of the control loop is generally chosen so as to minimize detection noise. Indeed, as the repetition frequency increases, shot noise decreases (because there are less photons) while detection noise increases (because there are more and more read-outs per second). In GENIEsim, the routine `loop_calib.pro` automatically computes the optimum repetition frequency for all control loops in order to minimize their noise. In the following sections, we discuss in detail the operation and expected performance of OPD, dispersion and intensity control loops.

6.2 OPD control

In order to control the optical path difference between two beams, we have to use an algorithm for phase measurement, which relies on the fringes that are formed when the light beams interfere. The most popular algorithm is the ABCD method.

6.2.1 The ABCD and AC algorithms

The ABCD method uses path length modulation and synchronous demodulation. A piezoelectrically controlled mirror is modulated in one arm of the interferometer with a triangle wave, in order to scan the fringes across one period. During one sweep of the piezo-actuator, the detected photons are grouped into four bins denoted A, B, C and D (see Figure 6.2). The amplitude and phase estimators are the following [SCH+88]:

$$\text{Amp} = \sqrt{(A-C)^2 + (B-D)^2} \ \text{ and } \ \phi = \tan^{-1}\left(\frac{A-C}{B-D}\right) \tag{6.7}$$

In practice, a slightly better signal-to-noise ratio (SNR) on the phase measurement can be obtained by using a discrete modulation scheme instead of a continuous one. The discrete ABCD algorithm relies on four modulation phases $\phi_k = k\pi/2$ with $k = 0, 1, 2, 3$. It uses the same phase estimator as the continuous method.

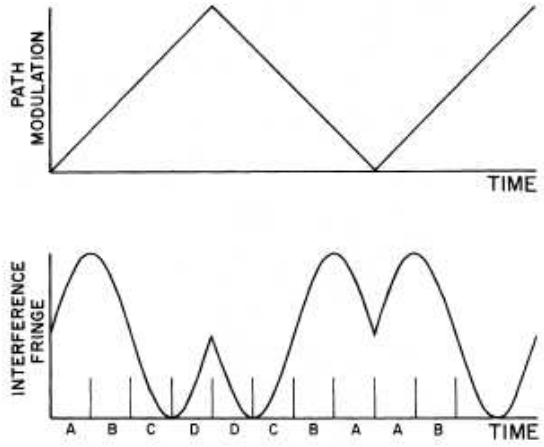

Figure 6.2: Principle of the ABCD algorithm, taken from [SCH+88]). The OPD is continuously swept using a piezo-actuated mirror and the detected photons are grouped into four bins denoted A, B, C and D.

The AC algorithm is an improved version of the discrete ABCD [Cas01]. It uses only two modulation phases: $\phi_k = 0$ and $\phi_k = \pi$. Since the two outputs of a beam-combiner are exactly in phase opposition, a piezo-translator is not needed any more: the two outputs of a beam-combiner are sufficient to use this algorithm! Moreover, the AC algorithm provides a larger SNR than the ABCD [Cas01]. However, most fringe sensing devices (including PRIMA-FSU) use the ABCD algorithm, which is considered to be more robust. For the GENIE instrument, the OPD errors are already partially corrected by the VLTI fringe tracking system, so that the robustness of the algorithm to phase jumps is not crucial. Moreover, a very high control accuracy is required. The AC algorithm is therefore implemented in GENIEsim for the OPD control loop.

6.2.2 Control loop noise

The physical quantity measured by the Fringe Sensing Unit is the phase of the fringe packet. If N_e denotes the number of available photons and σ_e the detector read-out noise, the variance in the phase measurement for a discrete ABCD algorithm is given by [MG01]:

$$\sigma_\phi = \frac{\sqrt{2(N_e + 4\sigma_e^2)}}{\mathcal{V}\, N_e} \tag{6.8}$$

where $\mathcal{V}$ denotes the fringe visibility. The factor 4 multiplying σ_e^2 accounts for the four detector read-outs of the ABCD method, while the factor 2 is related to the demodula-

tion method. A smaller phase variance can be obtained with the AC algorithm, which measures the two outputs of a beam-combiner during each time period. According to Cassaing [Cas01], the phase variance reduces to:

$$\sigma_\phi = \frac{\sqrt{N_e + 2\sigma_e^2}}{\mathcal{V}\, N_e} \ . \tag{6.9}$$

Assuming that the star is the main contributor to the total photon flux[2], the number of electrons writes:

$$N_e = F_* T_i \ , \tag{6.10}$$

F_* being the stellar flux expressed in photo-electrons per second.

6.2.3 Expected performance

The operation of the GENIE OPD control loop has been simulated with GENIEsim in the case of a Sun-like star located at 10 pc for an observation time of 10 sec. A Bracewell interferometer composed of UT2-UT3 (46.6 m baseline) is used. The time series for residual OPD is given in Figure 6.3 together with its associated PSD. The RMS OPD in 10 sec is only 21 nm. This performance meets the requirements given in section 5.4.3.1 in order to reduce the instrumental transmission below the physical transmission. The associated instrumental transmission amounts to 3×10^{-4} in the L' band and 4×10^{-5} in the N band. Note that the goal transmission of 10^{-4} is not reached yet in the L' band. The transfer function of the fast GENIE Delay Line and its associated noise are assumed to be negligible in this simulation. It is the task of the industrial contractors to design DLs to fulfill this assumption as much as possible. Preliminary results obtained with the fast DL of the nulling breadboards in the context of the Darwin TRP are encouraging in this respect (M. Barillot, personal communication).

The contribution of OPD-induced transmission noise to the total noise is shown in Figure 6.4. Using the UT2-UT3 configuration, we see that in the N band transmission noise is far below the shot noise associated with the huge background emission, while in the L' band they have comparable values. If ATs were used in the L' band, the background flux would have been much larger compared to the stellar signal, so that background noise would be dominant. Note the large difference in SNR for the two wavebands: the SNR evaluates to 90 in the L' band while it barely reaches 0.1 in the N band! Using a 24 m AT baseline in the L' band, the SNR would still be equal to 4 in 10 sec.

In conclusion, this simulation shows that OPD control with an accuracy of 21 nm RMS is possible with an optimized control loop, allowing to:

- reduce the instrumental leakage below the physical leakage both in the L' and the N band (the goal of 10^{-4} transmission being only achieved in the N band),
- reduce transmission noise below the unavoidable shot noise due to the background.

[2]This will generally be the case in the K band, where OPD control is performed.

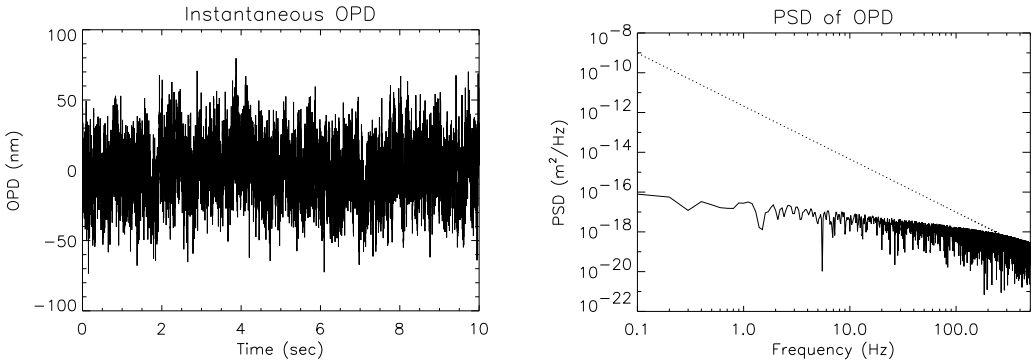

Figure 6.3: Simulation of the GENIE OPD control loop. Left: Time series for the residual OPD (RMS = 21 nm). Right: PSD of uncorrected (dotted) and corrected (solid) piston.

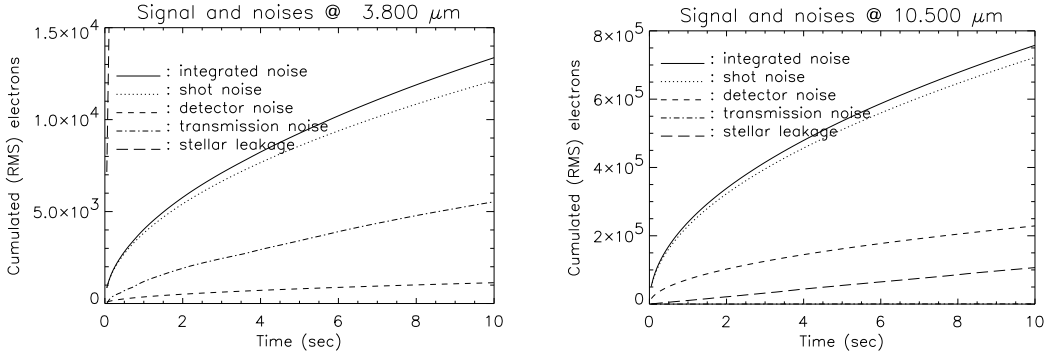

Figure 6.4: Simulation of the evolution of noise contributions with respect to time. The stellar leakage signal which has to be detected is also plotted for comparison. In the L' band, shot noise and transmission noise are comparable, and both are much smaller than the stellar leakage signal. In the N band, shot noise dominates both the transmission noise and the stellar leakage signal, due to the high background level.

6.3 Dispersion control

6.3.1 The challenges of dispersion control

There are two different sources of dispersion to be corrected: the slowly varying differential phase due to unequal paths through wet air in the delay lines, and on top of that the rapid phase fluctuations due to column density fluctuations of dispersive components in the atmosphere. The first one is deterministic and easy to correct provided that the atmospheric conditions in the tunnel are monitored with a sufficiently high accuracy,

while the second one is the real problem and has a main origin: water vapor.

6.3.1.1 Correction of inter-band dispersion

OPD fluctuations are corrected in the K band by the VLTI fringe tracking system to within a given accuracy (about 150 nm RMS on bright sources). Since dry air has very little dispersion in the infrared, the K-band fringe tracker also corrects for dry-air induced OPD fluctuations in the L' and N bands. On the other hand, the wavelength-dependent contribution to the OPD produced by water vapor will not be corrected in the L' and N bands if OPD control is performed in the K band. The random fluctuations due to dispersion have to be dealt with either by periodically measuring the fringe position in the observation waveband, or by monitoring the changing differential water column.

6.3.1.2 Correction of intra-band dispersion

Water vapor does not only induce dispersion between two wavebands: within a given waveband, the differential OPD (or differential phase) between the two beams depends on the wavelength, so that a correction with an additional path through air is not sufficient: it only corrects the phase difference at a given wavelength. As proposed by Koresko [KSC+03], longitudinal dispersion (deterministic and random components) can be corrected by introducing a variable amount of dispersive material (e.g. ZnSe in the N band) in the two arms of the interferometer. A pair of wedges is a good way to tune the path length through dispersive material while keeping constant the direction of the beams.

6.3.2 Preliminary design of the dispersion corrector

When entering the GENIE cryostat, the two beams are almost in phase in the K band thanks to the fringe tracking system. The co-phasing is even better after the dedicated GENIE OPD control system. What remains to be corrected is

- inter-band dispersion: cancel the phase difference between the two beams at the center of the observation wavelength (L' or N band),
- intra-band dispersion: cancel the first derivative of the phase with respect to wavelength in the observation waveband.

In order to correct for dispersion, we will introduce a variable amount of dispersive material (e.g. ZnSe) in the two arms[3] of the interferometer, and adjust the paths through dry air and ZnSe in real time within the GENIE cryostat. These paths have to be adjusted to compensate for both inter-band and intra-band dispersion at the same time. Let us compute the thickness of ZnSe to be added to correct for dispersion under typical Paranal conditions and the additional path through dry air to be introduced by the

[3] in order to preserve symmetry

GENIE DL to compensate for inter-band dispersion. We only present the case of the N band, which is of course the worst case for dispersion correction, to evaluate the most severe design constraints.

6.3.2.1 ZnSe thickness for intra-band dispersion

In the VLTI delay lines tunnel, water vapor has a typical molar density of 0.095 mole/m^3, so that the differential column density to be compensated is about 5.7 mole/m^2. Adding to that the contribution of water vapor fluctuations (1.5 mole/m^2 RMS), the ZnSe wedges should be able to compensate for a differential column density of about 10 mole/m^2. The optical path delay Δ created by a thickness e_{ZnSe} of ZnSe writes:

$$\Delta(\lambda) = n_{\mathrm{ZnSe}}(\lambda) e_{\mathrm{ZnSe}} \ , \tag{6.11}$$

so that the derivative of the OPD with respect to wavelength is:

$$\frac{\mathrm{d}\Delta}{\mathrm{d}\lambda} = \frac{\mathrm{d}n_{\mathrm{ZnSe}}}{\mathrm{d}\lambda}\, e_{\mathrm{ZnSe}} \tag{6.12}$$

with $\frac{\mathrm{d}n_{\mathrm{ZnSe}}}{\mathrm{d}\lambda} \simeq -0.0072\ \mu\mathrm{m}^{-1}$ in the N band. The first derivative with respect to wavelength of the OPD produced by a differential column density $\Delta\Sigma$ of water vapor writes:

$$\left.\frac{\mathrm{d}\Delta}{d\lambda}\right|_{10\mu m} = 10^{-15} c\, \Delta\Sigma\, \left.\frac{\mathrm{d}\hat{n}_{\mathrm{H_2O}}}{\mathrm{d}\lambda}\right|_{10\mu m} \tag{6.13}$$

where c is the speed of light and where $\left.\frac{\mathrm{d}\hat{n}_{\mathrm{H_2O}}}{\mathrm{d}\lambda}\right|_{10\mu m}$ is about -1.5 fs/(mole/m^2)/μm (see Figure 4.4), so that $\left.\frac{\mathrm{d}\Delta}{\mathrm{d}\lambda}\right|_{10\mu m} \simeq -4.5$. The thickness of ZnSe needed to correct for this amount of dispersion is 625 μm.

6.3.2.2 Additional path through dry air for inter-band dispersion

The difference in the refraction index of water vapor between the K and N band is $\Delta\hat{n}_{\mathrm{H_2O}} \simeq 4$ fs/(mole/m^2). Using the same values as in the previous paragraph, the differential OPD created in the middle of the N band by 60 m of wet air is thus 6.8 μm, while the fluctuations of water vapor column density produce a typical differential OPD of 1.8 μm. These sources of differential OPD require the GENIE DL to have a stroke of about 10 μm. However, the additional optical path through ZnSe that has been introduced in one arm of the interferometer also has to be compensated by an amount of dry air to preserve the co-phasing of the beams. An additional amount $n_{\mathrm{ZnSe}}(\lambda_{\mathrm{cen}}) \cdot e_{\mathrm{ZnSe}}$ of dry air has thus to be added in the other arm of the interferometer. For a typical ZnSe thickness of 625 μm, the additional path length through air must be as long as 1.5 mm. So, the stroke of the GENIE DL must be much larger than first anticipated: a few millimetres are required.

6.3.2.3 Phase residuals due to H_2O lines

In order to cancel intra-band dispersion across the whole observation bandwidth, the phase error produced by dry air and WDA must be fitted with the dispersive solid. ZnSe is particularly well adapted for N-band operation. However, water vapor exhibits a number of absorption lines in the $10-12.5$ μm band, and these produce high-frequency structures in the phase curve which become important once the smoothly-varying component is suppressed by the dispersion corrector. This residual phase error is about 0.007 rad across the reduced N band (see Figure 6.5). The wavelength-dependence of this residual phase error is not yet included in GENIEsim.

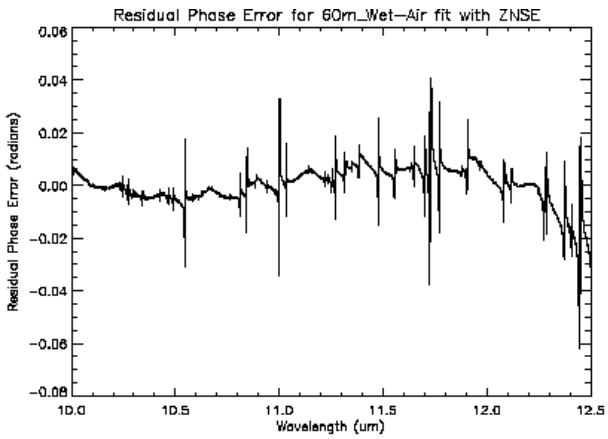

Figure 6.5: Residual phase error obtained by fitting the dispersion curve due to 60 m of wet air with ZnSe between 10 and 12.5 μm. Figure taken from [KSC+03].

6.3.3 Control strategies for N-band observations

In this paragraph, we will consider GENIE to operate in the total N band, from 8 to 13 μm. There are two main strategies for dispersion control: either a direct measurement of $\Delta\phi(\lambda)$ in the N band, or a measurement of the differential column density of water vapor $\Delta\Sigma$ at any other wavelength(s).

6.3.3.1 N-band dispersion measurement

We have shown in section 5.4.3.2 that the control loop for dispersion should have a precision of about 0.02 radian on the differential phase. Let us compute the control loop bandwidth required for typical Paranal atmospheric conditions. The fluctuations of water vapor column density $\sigma^2_{\Sigma,100s} = 1.5$ mole/m^2 measured on an integration time of 100 s produce, assuming a Kolmogorov spectrum, an RMS phase of about 0.1 radian for a 1 second time sequence in the middle of the N band. In order to have an RMS phase of about 0.02 radian, the power spectrum must be sharply cut at 10 Hz, so that in practice

the control loop repetition frequency must be about 100 Hz[4]. However, at a frequency of 100 Hz, it is not possible to measure the N-band phase with an accuracy better than 0.07 radian due to the shot noise associated with the background. Therefore, *an N-band Dispersion Sensing Unit is not suited for N-band dispersion control* under the Paranal atmospheric conditions.

6.3.3.2 K and/or L-band column density measurement

The method proposed here is to measure the WDA-induced phase fluctuations in the K band and/or L' band in order to deduce the differential WDA column density between the beams, and then the WDA-induced phase fluctuations in the N band. This is clearly not an easy task, because dry-air induced fluctuations are much larger than WDA-induced fluctuations in the K band (see Figure 4.6). However, even in the near-infrared, dry air does not induce dispersion while WDA does. Therefore, measuring the phase of the fringes at two wavelengths within the K band, or in the K and L' bands, is a good way to infer the WDA column density difference between the two beams. The phase difference between the two beams (i.e., the phase of the fringes) increases as a function of wavelength. The slope of the phase difference with respect to wavelength directly gives the WDA column density difference between the two beams provided that the dispersion curve (Figure 4.5) is known in that spectral domain. From this column density, we can theoretically compute the phase difference in any other spectral channel, especially the N band, provided that the refraction index of WDA is known with a sufficiently high accuracy in this waveband. In order to perform a precise measurement of dispersion, it is preferable to use the K and L' bands simultaneously. This increases the overall SNR and allows to measure a larger phase difference on a wider spectral domain, which should decrease the measurement error.

The main difficulty associated with K/L' band dispersion measurement is our limited knowledge on the refraction index of WDA. Although simulated data for atmospheric dispersion are available in the literature ([HL86], [Cid96], [Mat02]) and take into account most of the spectral lines in the near- and mid-infrared, these data depend on the actual atmospheric conditions, which vary from night to night and even during a single night. Analytical expressions for the water-vapor refractive index are thus maybe not sufficient to ensure a good dispersion correction. A possible solution to overcome this problem is to operate simultaneously an N-band OPD sensor at a lower frequency (about 0.1 Hz) to ensure that no systematic error is done in the inter-band dispersion correction. This is the current baseline for the GENIE dispersion control loop. In GENIEsim, we will use the K-L' band control loop, and assume that the refraction index of WDA is known with an infinite precision in the near- and mid-infrared regions. We use this simplification because we currently have no idea of how the refraction index of WDA varies on short and long timescales.

[4]There is typically an order of magnitude between the repetition frequency of the control loop and the frequency at which its transfer function significantly reduces the power contained in the PSD.

6.3.4 Control strategies for L'-band observations

Dispersion control is expected to be easier for an L'-band GENIE than for an N-band version, because the refraction index of WDA does not vary much between the K band where fringe tracking is performed and the L' band where observations are done (see Figure 4.5). Tables 5.4 and 5.3 confirm that inter-band and intra-band dispersion are less severe in the L' band than in the N band.

Dispersion control in the L' band can be carried out in the same way as in the N band: by dividing the K band in two spectral bins and measuring the phase of the fringes in these two bins, the differential column density of water vapor can be inferred and then used to derive the expected phase difference in the whole L' band. As in the N band, this method relies on a good knowledge of the refraction index of WDA ($\hat{n}_{\mathrm{WDA}}$). However, the required accuracy should be somewhat relaxed with respect to the N band because of the smaller slope of $\hat{n}_{\mathrm{WDA}}$ in the near infrared. But here also, it would be safer to collect a small part of the L' band photon to measure at a low frequency the actual differential OPD in the L' band to remove possible systematic errors in the dispersion control. Note that this additional correction can be done at a much higher frequency than in the N band thanks to the larger SNR.

6.3.5 Control loop noise

The quantity we want to measure is the water vapor column density difference between the paths followed by the two beams through the atmosphere. The measurement consists in (at least) two phase measurements at two different wavelengths in the K and/or L' bands. The analytical relation between the measured phase differences and the differential column density of WDA ($\Delta\Sigma_{\mathrm{WDA}}$) is derived in the following paragraph. Let ϕ^a be the phase of beam a and ϕ^b the phase of beam b. We have:

$$\begin{aligned}
\phi^a(\lambda) &= \frac{2\pi}{\lambda}[L^a_{\mathrm{vac}} + \Sigma^a_{\mathrm{air}}\hat{n}_{\mathrm{air}}(\lambda) + \Sigma^a_{\mathrm{WDA}}\hat{n}_{\mathrm{WDA}}(\lambda) + e^a_{\mathrm{ZnSe}}n_{\mathrm{ZnSe}}(\lambda)] \\
\phi^b(\lambda) &= \frac{2\pi}{\lambda}[L^b_{\mathrm{vac}} + \Sigma^b_{\mathrm{air}}\hat{n}_{\mathrm{air}}(\lambda) + \Sigma^b_{\mathrm{WDA}}\hat{n}_{\mathrm{WDA}}(\lambda) + e^b_{\mathrm{ZnSe}}n_{\mathrm{ZnSe}}(\lambda)]
\end{aligned}$$

In these expressions, we take into account the effect of the path length through vacuum (L_{vac}), through the humid atmosphere and delay lines (total column densities Σ_{air} for dry air and Σ_{WDA} for WDA) and through the correction device (the ZnSe wedges of total thickness e_{ZnSe}). The reduced refraction indexes $\hat{n}$ are expressed in $\mathrm{m}/(\mathrm{mole}/\mathrm{m}^2)$. The phase differences at control wavelengths λ_1 and λ_2 are respectively given by:

$$\begin{aligned}
\Delta\phi(\lambda_1) &= \frac{2\pi}{\lambda_1}[\Delta L_{\mathrm{vac}} + \Delta\Sigma_{\mathrm{air}}\hat{n}_{\mathrm{air}}(\lambda_1) + \Delta\Sigma_{\mathrm{WDA}}\hat{n}_{\mathrm{WDA}}(\lambda_1) + \Delta e_{\mathrm{ZnSe}}n_{\mathrm{ZnSe}}(\lambda_1)] \\
\Delta\phi(\lambda_2) &= \frac{2\pi}{\lambda_2}[\Delta L_{\mathrm{vac}} + \Delta\Sigma_{\mathrm{air}}\hat{n}_{\mathrm{air}}(\lambda_2) + \Delta\Sigma_{\mathrm{WDA}}\hat{n}_{\mathrm{WDA}}(\lambda_2) + \Delta e_{\mathrm{ZnSe}}n_{\mathrm{ZnSe}}(\lambda_2)]
\end{aligned}$$

The left-hand side of these expressions is measured by the Dispersion Sensing Unit, while two unknowns remain in the right-hand side: $\Delta\Sigma_{\mathrm{air}}$ and $\Delta\Sigma_{\mathrm{WDA}}$ (the differential

column densities of dry air and WDA). The differential path length through vacuum can be computed from the stellar position $\vec{\theta}$ and the baseline vector $\vec{b}$ ($\Delta L_{\rm vac} = \vec{b} \cdot \vec{\theta}$) provided that the baseline vector is known with a sufficiently high accuracy[5], while the differential thickness of ZnSe ($\Delta e_{\rm ZnSe}$) is actively controlled. The differential column density of WDA is thus given by:

$$\begin{aligned}
\Delta\Sigma_{\rm WDA} &= \frac{1}{\frac{\hat{n}_{\rm WDA}(\lambda_2)}{\hat{n}_{\rm air}(\lambda_2)} - \frac{\hat{n}_{\rm WDA}(\lambda_1)}{\hat{n}_{\rm air}(\lambda_1)}} \left(\frac{\lambda_2}{2\pi\hat{n}_{\rm air}(\lambda_2)}\Delta\phi(\lambda_2) - \frac{\lambda_1}{2\pi\hat{n}_{\rm air}(\lambda_1)}\Delta\phi(\lambda_1) \right) \\
&+ \frac{\hat{n}_{\rm air}(\lambda_1) - \hat{n}_{\rm air}(\lambda_2)}{\hat{n}_{\rm WDA}(\lambda_2)\hat{n}_{\rm air}(\lambda_1) - \hat{n}_{\rm WDA}(\lambda_1)\hat{n}_{\rm air}(\lambda_2)} \Delta L_{\rm vac} \\
&+ \frac{n_{\rm ZnSe}(\lambda_2)\hat{n}_{\rm air}(\lambda_1) - n_{\rm ZnSe}(\lambda_1)\hat{n}_{\rm air}(\lambda_2)}{\hat{n}_{\rm WDA}(\lambda_2)\hat{n}_{\rm air}(\lambda_1) - \hat{n}_{\rm WDA}(\lambda_1)\hat{n}_{\rm air}(\lambda_2)} \Delta e_{\rm ZnSe}
\end{aligned}$$

In this expression, we will assume that the refraction indexes of dry air and WDA are known with a sufficiently high accuracy, as well as $\Delta L_{\rm vac}$ and $\Delta e_{\rm ZnSe}$. The only error in the column density computation thus comes from the measurement errors on the phase differences $\Delta\phi(\lambda_1)$ and $\Delta\phi(\lambda_2)$. Assuming that the two measurements are uncorrelated, the variance on the measured column density difference can be expressed as follows:

$$\sigma^2_{\Sigma_{\rm WDA}} = \frac{1}{\left(\frac{\hat{n}_{\rm WDA}(\lambda_2)}{\hat{n}_{\rm air}(\lambda_2)} - \frac{\hat{n}_{\rm WDA}(\lambda_1)}{\hat{n}_{\rm air}(\lambda_1)} \right)^2} \left(\frac{\lambda_2^2}{4\pi^2\hat{n}^2_{\rm air}(\lambda_2)}\sigma^2_{\Delta\phi}(\lambda_2) + \frac{\lambda_1^2}{4\pi^2\hat{n}^2_{\rm air}(\lambda_1)}\sigma^2_{\Delta\phi}(\lambda_1) \right) \quad (6.14)$$

Assuming that an AC algorithm (section 6.2.1) is used to perform the phase measurements, the variance on the column density is the following:

$$\sigma^2_{\Sigma_{\rm WDA}} = \frac{\frac{\lambda_2^2}{4\pi^2\hat{n}^2_{\rm air}(\lambda_2)} \frac{N_e(\lambda_2)+2\sigma_e^2(\lambda_2)}{\mathcal{V}^2(\lambda_2)N_e^2(\lambda_2)} + \frac{\lambda_1^2}{4\pi^2\hat{n}^2_{\rm air}(\lambda_1)} \frac{N_e(\lambda_1)+2\sigma_e^2(\lambda_1)}{\mathcal{V}^2(\lambda_1)N_e^2(\lambda_1)}}{\left(\frac{\hat{n}_{\rm WDA}(\lambda_2)}{\hat{n}_{\rm air}(\lambda_2)} - \frac{\hat{n}_{\rm WDA}(\lambda_1)}{\hat{n}_{\rm air}(\lambda_1)} \right)^2} \quad (6.15)$$

Knowing that $\hat{n}_{\rm air}(\lambda_2) \simeq \hat{n}_{\rm air}(\lambda_1)$ for infrared wavelengths, this expression can be simplified:

$$\sigma^2_{\Sigma_{\rm WDA}} = \frac{\lambda_2^2 \frac{N_e(\lambda_2)+2\sigma_e^2(\lambda_2)}{V^2(\lambda_2)N_e^2(\lambda_2)} + \lambda_1^2 \frac{N_e(\lambda_1)+2\sigma_e^2(\lambda_1)}{V^2(\lambda_1)N_e^2(\lambda_1)}}{4\pi^2(\hat{n}_{\rm WDA}(\lambda_2) - \hat{n}_{\rm WDA}(\lambda_1))^2} \quad (6.16)$$

It is very interesting to notice that the imprecision on the column density measurement is large when λ_1 is close to λ_2. In that case, the denominator is close to 0, especially in the K band where the slope of the refractive index of WDA is not very steep. A better control accuracy is reached when the K and L' bands are used simultaneously.

Once the differential column density is computed, it is then used to calculate the expected phase difference between the two beams at the observation wavelength λ_3. The

[5]This may not be the case in practice. We would then be forced to make three phase measurements to determine $\Delta\Sigma_{\rm air}$, $\Delta\Sigma_{\rm WDA}$ and $\Delta L_{\rm vac}$ simultaneously.

variance on the phase difference due to measurement errors writes:

$$\sigma^2_{\Delta\phi}(\lambda_3) = \frac{4\pi^2}{\lambda_3^2}\hat{n}^2_{\mathrm{WDA}}(\lambda_3)\sigma^2_{\Sigma_{\mathrm{WDA}}} \tag{6.17}$$

The PSD of the detection noise in the dispersion control loop is given by equations (6.4) and (6.6):

$$S_{\mathrm{DSU}}(f) = \sigma^2_{\Delta\phi}(\lambda_3) T_i \,\mathrm{sinc}(fT_i) \tag{6.18}$$

Assuming that the visibility is close to 1 and that the star is the dominant source of photons, the noise PSD of Dispersion Sensing Unit is given by:

$$S_{\mathrm{DSU}}(f) = \frac{\lambda_2^2\left(\frac{1}{F_*(\lambda_2)} + \frac{2\sigma_e^2}{F_*(\lambda_2)^2 T_i}\right) + \lambda_1^2\left(\frac{1}{F_*(\lambda_1)} + \frac{2\sigma_e^2}{F_*(\lambda_1)^2 T_i}\right)}{\lambda_3^2\left(\frac{\hat{n}_{\mathrm{WDA}}(\lambda_2) - \hat{n}_{\mathrm{WDA}}(\lambda_1)}{\hat{n}_{\mathrm{WDA}}(\lambda_3)}\right)^2} \,\mathrm{sinc}(fT_i) \tag{6.19}$$

If the L' band is used for phase measurement, the background flux is not negligible any more, and must be taken into account in the expression of the photon noise. This limitation is discussed in section 6.4.3, and is taken into account in GENIEsim.

Note that the Dispersion Sensing Unit also provides a direct access to the piston error, related to the differential column density of dry air $\Delta\Sigma_{\mathrm{air}}$. It is thus expected to merge the sensing units for OPD and dispersion in a two- or three-colored Fringe Sensing Unit.

6.3.6 Expected performance

We have simulated the operation of the GENIE dispersion control loop with the GENIEsim software, using different repetition times for the closed loop. Table 6.1 gives the residual phase error obtained for inter-band and intra-band dispersion. This table shows that, in the N band, the required accuracy on the differential phase can be reached with a 1000 Hz control loop based on K-L' band fringe sensing. A higher repetition frequency does not give much better results because the detection noise of the control loop becomes dominant, so that the performance cannot be increased any more. In practice, an optimum repetition frequency of 2000 Hz is found by GENIEsim. The corresponding time sequence and PSD for residual dispersion are given in Figure 6.6. In the L' band, the dispersion control loop badly suffers from the proximity of the two wavelengths at which phase measurement is performed. If phase is measured around 2.1 and 2.3 μm, the residual phase error for the control is as high as 0.035 radian RMS for inter-band dispersion in the L' band at an optimum repetition frequency of 1200 kHz. In order to reduce this figure below the required 0.02 radian RMS, a part of the L'-band photons must be used. With 10% of the L' band flux, the residual phase error reduces to 0.018 radian RMS at an optimum frequency of 200 Hz[6]. In Table 6.1, the residual phase

[6]The optimum frequency strongly decreases when L'-band photon are used, because of lower signal-ton-noise ratio (only 10% of the L'-band photons are collected, and the background is larger than in the K band).

errors in the L' band are based on a K-band phase measurement only, showing that L'-band photon are mandatory for dispersion control. Once again, let us remind that the limitations due to the GENIE Delay Line and dispersion corrector (ZnSe wedges) are not taken into account in this simulation. It is not known whether the dispersion corrector can afford repetition frequencies as high as 2 kHz.

	L' band		N band	
	Inter	Intra	Inter	Intra
$\sigma_{\Delta\phi}$(10Hz)	0.42 rad	0.024 rad	0.28 rad	0.075 rad
$\sigma_{\Delta\phi}$(100Hz)	0.12 rad	0.012 rad	0.049 rad	0.017 rad
$\sigma_{\Delta\phi}$(1000Hz)	0.10 rad	0.011 rad	0.024 rad	0.013 rad

Table 6.1: Influence of the repetition frequency of the dispersion control loop on the residual phase shift. The simulations were carried out with a UT2-UT3 baseline pointing at a Sun-like star at 10 pc. Dispersion control is done in the K band for L' band observations and in the K-L' bands for N band observations.

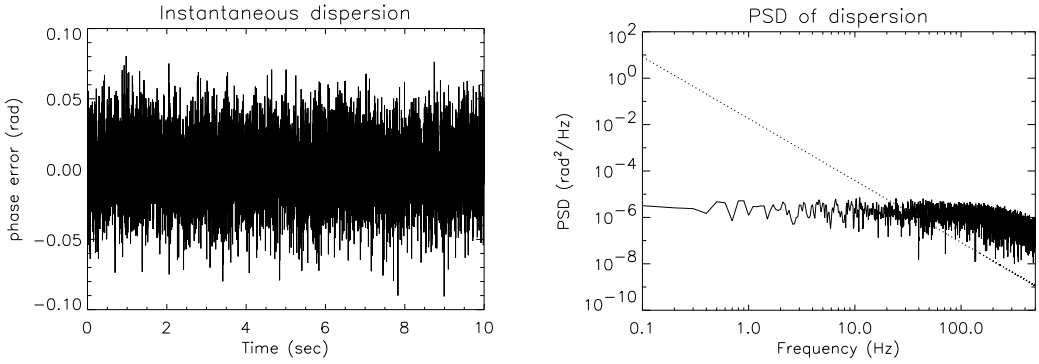

Figure 6.6: Simulation of the GENIE dispersion control loop in the N band. Left: Time series for the residual phase due to dispersion (RMS = 0.024 nm). Right: PSD of uncorrected (dotted) and corrected (solid) dispersion.

The influence of the transmission noise associated with residual dispersion fluctuations is shown in Figure 6.7. Using the UT2-UT3 configuration, we see that in the N band transmission noise is far below the shot noise associated with the huge background emission, while in the L' band transmission noise is dominant. If ATs were used in the L' band, the background flux would be much larger compared to the stellar signal, so that background noise would be dominant. Once again, there is a large difference in SNR for the two wavebands: the SNR amounts to 72 in the L' band while it barely reaches 0.13 in the N band! Using a 24 m AT baseline in the L' band, the SNR would still be equal to 11 in 10 sec.

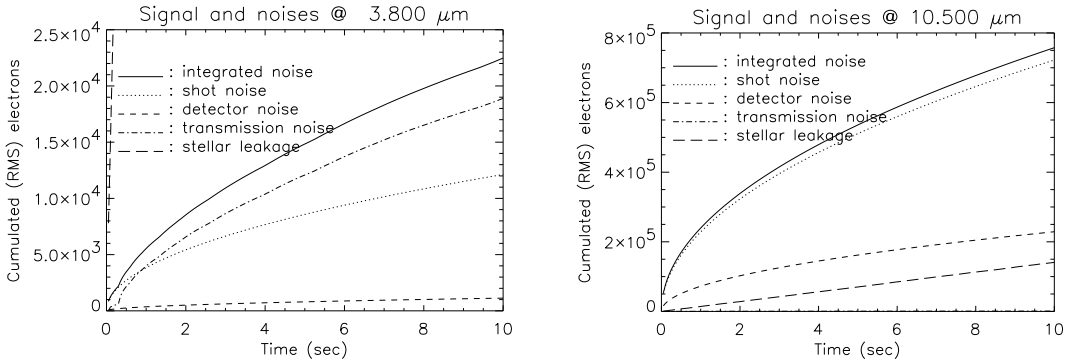

Figure 6.7: Simulation of the evolution of noise contributions with respect to time. The stellar leakage signal which has to be detected is also plotted for comparison. In the L' band, transmission noise exceeds shot noise, and both are much smaller than the stellar leakage signal. In the N band, shot noise dominates both the transmission noise and the stellar leakage signal due to the high background level.

In conclusion, this simulation shows that dispersion control with an accuracy of about 40 nm RMS on the differential phase is possible with an optimized control loop, allowing to:

- reduce the instrumental leakage below the physical leakage both in the L' and the N band (the goal of 10^{-4} transmission being only achieved in the N band),
- reduce transmission noise below the unavoidable shot noise due to the background for the N band, and to make it comparable to the shot noise in the L' band.

6.4 Intensity matching

Intensity matching aims at equalizing the fluxes in the two modal filters that carry the light towards the beam-combiner. In order to do that, a part of the flux is extracted from (or after) the modal filter, before recombination, as shown in Figure 4.17. Intensity matching is performed on the stellar signal, because this is the coherent part of the signal, which has to be cancelled by the nulling process. In order to measure the stellar signal precisely, the thermal background has to be removed. This will be done with the help of chopping (see section 6.5). If classical chopping is used, benefiting from the chopping mirrors available both on UTs and ATs, the chopping frequency is limited to 5 Hz. Intensity matching, which cannot be done more than once per chopping period, is thus limited to a repetition time of 200 msec. Worse, the possibility itself of performing intensity matching with classical chopping is not ensured: due to the movement of the chopping mirror, the position of the star image on the fiber slightly changes from one chopping period to another. Intensity fluctuations could then be completely decorrelated

between two chopping periods and their matching impossible. It is thus probable that advanced chopping schemes (discussed in section 6.5) are required to perform intensity matching. In the following developments, we will assume that such a scheme is used.

In order to maintain the instrumental transmission below 10^{-4}, the relative error on the beam intensities should be smaller than 4%, as proven in section 5.4.4. In that section, we have also seen that intensity matching is required if GENIE operates in the L' band, while an N-band GENIE could afford operation without intensity control. The performance of a control loop for accurate intensity matching is nevertheless evaluated in both bands in the following sections.

6.4.1 Intensity matching for N band observations

Performing intensity matching in the N band is a difficult task, because of the shot noise associated with the high background level. The problem is to measure the stellar flux with a sufficiently high signal-to-noise ratio within the typical time on which the intensity fluctuates. Assuming that *10% of the flux is used for intensity matching*, the expected fluxes at the intensity sensor are:

- $F_{\text{bckg}} = 2.6 \times 10^9$ e$^-$/sec for the background,
- $F_* = 3.6 \times 10^6$ e$^-$/sec for a Sun-like star at 10 pc,
- $F_{\text{exo}} = 1.6 \times 10^3$ e$^-$/sec for a 10-zodi disk.

The accuracy of intensity matching is limited by shot noise to about $F_{\text{bckg}}^{1/2}/(F_* T_i^{1/2})$ with F_{bckg} and F_* the background and stellar flux expressed in photo-electrons per second and T_i the integration time of the control loop. In order to get a sufficiently high SNR on the intensity measurement, the repetition time should be long enough, but on the other hand, control must be done at a sufficiently high frequency to compensate for intensity fluctuations. For the N band, the optimum repetition frequency is about 1 Hz: in 1 sec, we have $F_{\text{bckg}}^{1/2}/(F_* T_i^{1/2}) = 0.007$ while the Strehl fluctuations are $\sigma_S = 0.008$ (see Table 4.5). The precision on the measurement is thus of the order of the expected intensity fluctuation, which is the best compromise. At frequencies higher than 1 Hz, the intensity-matching device would not be efficient at all since the measurement error of the Sensing Unit would be larger than the Strehl fluctuations.

Note that intensity matching cannot be performed in the K or L' band when the observation is carried out in the N band because:

- N band single-mode fibers are not single-mode in the K or L' bands,
- K or L' band single-mode fibers cannot be used in the N band,
- the correction in the K or L' band would not ensure a good correction in the N band, because the Strehl ratio is wavelength-dependent.

As a conclusion, intensity matching in the N band cannot be performed at a higher frequency than 1 Hz. Such a control loop would only be required if there was a lot of energy at low frequencies in the spectrum of Strehl fluctuations. This is not expected because the outer scale of turbulence flattens the PSD for frequencies below $v/L_0 \simeq 0.1$ Hz for typical atmospheric conditions at Paranal (wind speed $v \simeq 10$ m/s, outer scale $L_0 \simeq 100$ m). Real-time intensity matching in the N band is therefore probably not necessary. A slow intensity sensor could still be added to monitor long-term drifts in the relative beam transmissions.

6.4.2 Intensity matching for L'-band observations

Intensity matching in the L' band is easier than in the N band, because the stellar flux generally exceeds the incoherent background integrated over the field-of-view. Assuming that 10% of the flux is used for intensity matching, the expected thermal background level at the detector is 7.3×10^5 e$^-$/s, while the flux of a Sun-like star at 10 pc is about 6.8×10^6 e$^-$/s. The shot-noise limited accuracy of intensity measurement is thus about $1/(F_* T_i)^{1/2}$ because in this case the star is the main contributor to shot noise. The optimum repetition frequency for the intensity control loop is about 1 kHz: a repetition time of 1 msec gives an accuracy of 0.7% on the intensity measurement, while the Strehl ratio fluctuates typically by 0.3% during that same time according to the PSD of Figure 4.14.

6.4.3 Control loop noise

The physical quantity measured by the Intensity Sensing Unit (ISU) is the number of photo-electrons collected by the two fibers during an integration time T_i. These two numbers are then compared and the correction is computed so as to equalize them by inserting a knife into the input beams, before injection into the fiber (see Figure 4.17). The variance on the intensity measurement is simply given by the ratio of noise to signal in a single fiber:

$$\sigma_I = \frac{\sqrt{N_e + \sigma_e^2}}{N_e} \tag{6.20}$$

Note that, in this expression, the detector noise depends on the number of pixels that have to be used in order not to saturate the detector. The white detection noise writes:

$$S_0 = \frac{N_e + \sigma_e^2}{N_e^2} T_i \Rightarrow \left\{ \begin{array}{l} S_{\rm phn} = 1/F_* \\ S_{\rm ron} = \sigma_e^2/(F_*^2 T_i) \end{array} \right. \tag{6.21}$$

where F_* denotes the flux of stellar photo-electrons per second. The PSD of detection noise in the intensity control loop thus writes:

$$S_{\rm ISU}(f) = \left(\frac{1}{F_*} + \frac{\sigma_e^2}{F_*^2 T_i} \right) {\rm sinc}^2(f T_i) \tag{6.22}$$

However, since GENIE operates in the mid-infrared, the stellar flux is not necessarily the main source of photons: the background can also play an important role, and act as a major noise source, by:

- increasing the photon noise,
- increasing the read-out noise if the signal has to be dispersed on two or more pixels to avoid saturation of the detector,
- adding background noise, which can only be reduced by chopping.

In GENIEsim, we assume that background noise due to imperfect subtraction of the background flux is negligible. This is not a severe restriction since intensity matching is probably only feasible with an "advanced" chopping scheme (see section 6.5) which should allow to subtract the background efficiently (BLIP conditions). In presence of background flux, the variance on the intensity measurement is given by:

$$\sigma_I = \frac{\sqrt{N_{\rm tot} + \sigma_e^2}}{N_*} \tag{6.23}$$

where $N_{\rm tot}$ is the total number of photo-electrons while N_* is the number of photo-electrons associated with the star. The PSD of detection noise then writes:

$$S_{\rm ISU}(f) = \left(\frac{F_{\rm tot}}{F_*} + \frac{\sigma_e^2}{F_*^2 T_i} \right) {\rm sinc}^2(f T_i) \tag{6.24}$$

6.4.4 Expected performance

To simulate the performance of the intensity control loop, we have used MACAO+UTs in a Bracewell configuration, because the simulated performance of STRAP on ATs is not yet available. A Sun-like star at 10 pc was chosen as usual. We have simulated a 10 sec observation with GENIEsim, using intensity control at 2 kHz for the L' band, and no intensity control in the N band. All other instrumental errors have been artificially set to zero. The instantaneous coupling efficiency in one of the two fibers is given in Figure 6.8 for the two bands. The RMS coupling efficiency in these simulations are 1.6% and 6% for the L' and the N band respectively, which are both comparable to the required 4% for a 10^{-4} instrumental transmission.

In Figure 6.9 are given the expected contributions of shot noise, detector noise and transmission noise for these two simulations. In both cases, transmission noise is negligible as compared to shot noise.

6.5 The chopping schemes

In order to extract the data from the incoherent background, modulation techniques are required. A major issue is the consistency of the modulation frequency with respect

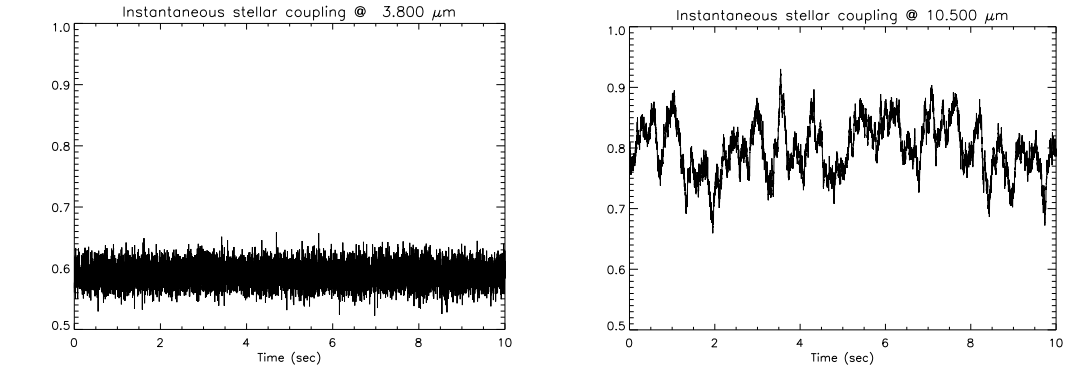

Figure 6.8: Simulation of the GENIE instantaneous coupling efficiency. Left: coupling efficiency in the L' band with intensity matching at 2000 Hz. Right: coupling efficiency in the N band with no intensity control. The absence of control loop explains the low-frequency fluctuations in the coupling efficiency.

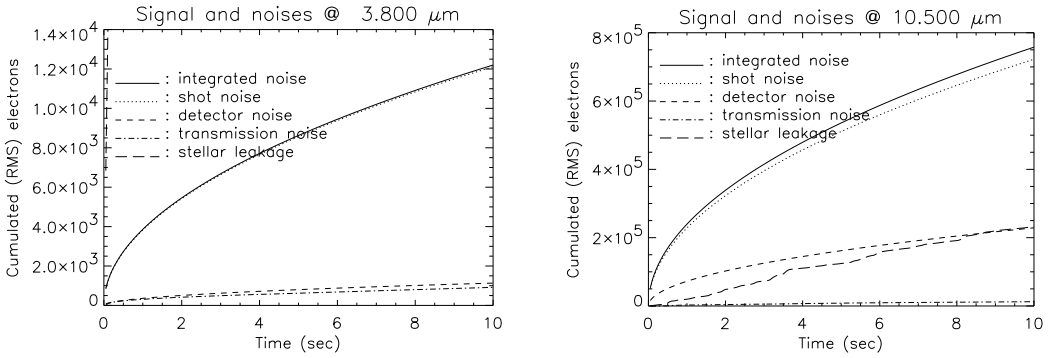

Figure 6.9: Simulation of the evolution of noise contributions with respect to time. The stellar leakage signal which has to be detected is also plotted for comparison. Transmission noise due to intensity mismatches is dominated by shot noise in both the L' and the N bands. Note the erratic behaviour of the stellar leakage signal, due to the low-frequency variations of coupling efficiency in the N band.

to the time constants of the background fluctuations, discussed in section 5.3.1. The integration time for each modulated measurement must be shorter than the drift time constant of the whole detection system (atmosphere, telescope, relay optics, detector, electronics).

6.5.1 Classical chopping - nodding

Infrared observations with single telescopes have been using the chopping-nodding technique for more than 30 years. This technique relies on the tilting of the secondary mirror of the telescope to sample an empty sky region nearby the scientific target (see Figure 6.10).

- *Chopping*: the secondary mirror of the telescope is offset by a small quantity (a few arcseconds) to measure the background nearby the source and subtract it from the source measurement. The chopping sequence is repeated at a few Hertz.

- *Nodding*: During chopping, the beam paths for the source and the background are slightly different. Chopping therefore allows to subtract the average amount of background from the image but a higher order residual remains. It is measured and subtracted by repeating the whole chopping sequence off-source. This is especially important to subtract instrumental background, which depends on the path of the light beams through the optical train.

With this sequence, 25% of the observing time is usually spent off-source. This can be improved to 50% in the nodding sequence by placing the source in the offset position of the secondary mirror (see Figure 6.10).

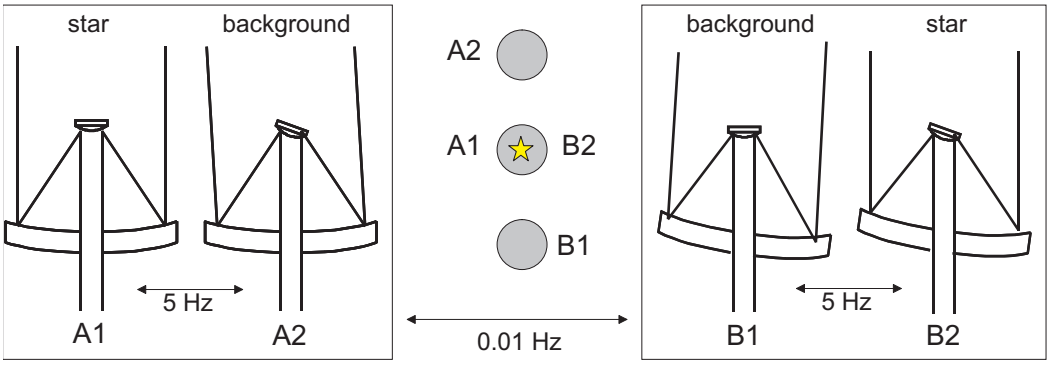

Figure 6.10: Principle of chopping/nodding. The detector alternately records the background and the target star + background. Nodding on a timescale of a few minutes allows to remove the remaining gradient in background-subtracted data.

The secondary mirrors of the VLTI Unit and Auxiliary Telescopes are designed to allow for chopping, with a frequency between 0.1 and 5 Hz. The stroke on the sky and the settling time are respectively of ±15' and 20 msec for the UTs, and of ±6' and 5 msec for the ATs. The chopping/nodding strategy has proven to be efficient for imaging. In the case of the GENIE experiment, there are three major limitations to the feasibility of this technique:

- *Low frequency*: Due to mechanical constraints, the chopping frequency is limited to 5 Hz at the VLTI. It is not clear whether this is sufficient to reach background-limited performances. Background measurements with MIDI on the VLTI are the only way to firmly answer this question.

- *Low efficiency*: When measuring the background emission, the control loops for OPD control, intensity matching and dispersion control cannot remain in closed loop because the central star is not in the field-of-view any more. Therefore, all these subsystems will re-close their loops successively before performing the next target measurement. According to current simulations [KG01], this should take about 80 msec on bright stars (including the 20 msec settling time of the chopping mirror). However, subsystems such as PRIMA are still subject to modification, so that the 80 msec time delay is still speculative. In order to reduce the loss of time during chopping, synchronized chopping is highly recommended. But even with a delay of only 80 msec in the locking of the fringes, the duty cycle would be reduced to about 42% for chopping/nodding at 5 Hz.

- *High frequency vibrations*: The RMS OPD induced by chopping has been measured on the Unit Telescopes: 185 nm RMS over 290 msec on each plateau [KG01]. The PSD of chopping-induced OPD fluctuations shows two important peaks. The first one, around 20 Hz, should be strongly reduced by the FSU. The second one, around 100 Hz, will add to the high-frequency component of the atmospheric OPD, which is not well cancelled by the FSU. In comparison, the amount of atmospheric OPD at frequencies above 100 Hz is only about 20 nm RMS. The influence of chopping-induced OPD on the GENIE performances could thus be a major inconvenience of classical chopping.

According to these remarks, classical chopping could thus be unsuited to GENIE. There are two possible ways to improve the efficiency of the chopping cycle: counter-chopping or dual feed with the PRIMA facility, which will be investigated during the definition study. But these will not correct for all effects, so that new methods for background calibration must be developed.

6.5.2 Internal chopping with phase modulation

There is a possibility to chop the signal inside GENIE using phase modulation, provided that the pupils of the two telescopes are divided into two parts. This technique has been proposed by Kuchner and Serabyn [KS01] in the context of the Keck nuller. The principle is to recombine the first (resp. second) half of telescope 1 with the first (resp. second) half of telescope 2 by means of a nulling interferometer, and to recombine the two nulled outputs with a variable phase shift $\phi(t)$ (see Figure 6.11). The result is a set of baselines of two different types: long ($\sim$ 50 m) baselines between the corresponding sub-apertures on the two UTs, and short ($\sim$ 3.4 m for UTs) baselines between the two

halves of each telescope. The two beam-combiners produce two perpendicular fringe patterns, with respective periods of $\lambda/46 \simeq 45$ mas and $\lambda/3.4 \simeq 618$ mas.

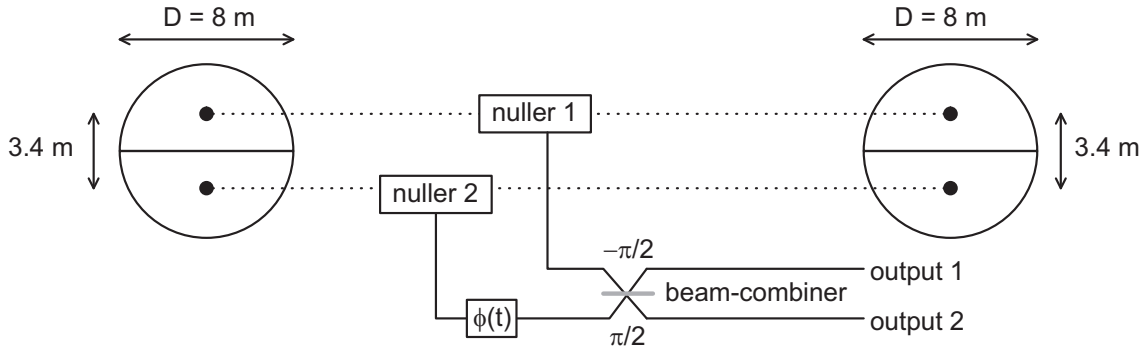

Figure 6.11: Principle of internal chopping. The two UTs are recombined half by half, and the two resulting nulled beams are combined with a time-varying phase shift.

Figure 6.12 illustrates how internal chopping can be used to remove the background contribution from the scientific data: if $\phi = \pi/2$, the final beam-combiner will give a constructive on-axis interference for the first output and a destructive on-axis interference for the other one[7]. The contribution of the exozodiacal cloud will therefore be very different in the two outputs, while the incoherent background has the same contribution in both outputs. Chopping can thus be carried out by alternately detecting these two outputs, at a sufficiently high frequency. Thanks to the two outputs, a time-varying phase shift is not needed, although the measurement at different ϕ would yield additional information on the cloud morphology. In the case of the "$\pm\pi/2$" chopping considered here, the duty cycle is 100% provided that two detectors are used to continuously monitor the two outputs. However, the pupil division, which could be realized in the interferometric lab, will degrade the overall SNR by decreasing the fiber coupling efficiency: the ellipsoidal diffraction pattern associated with a semi-circular aperture does not match the fundamental mode of the fiber any more. The use of cylindrical optics to squeeze the diffraction pattern in one direction could attenuate this drawback.

6.6 Stellar leakage calibration

One of the most stringent specification on the GENIE design is the capability to achieve deep and stable nulls, with a goal rejection rate of 10^{-4}. We have seen in section 2.2 that the physical stellar leakage associated with the finite angular diameter of the star is

[7]In the recombination process, the beam-combiner induces a $\pi/2$ phase shift between the two beams in the first output, and a $-\pi/2$ phase shift in the second output.

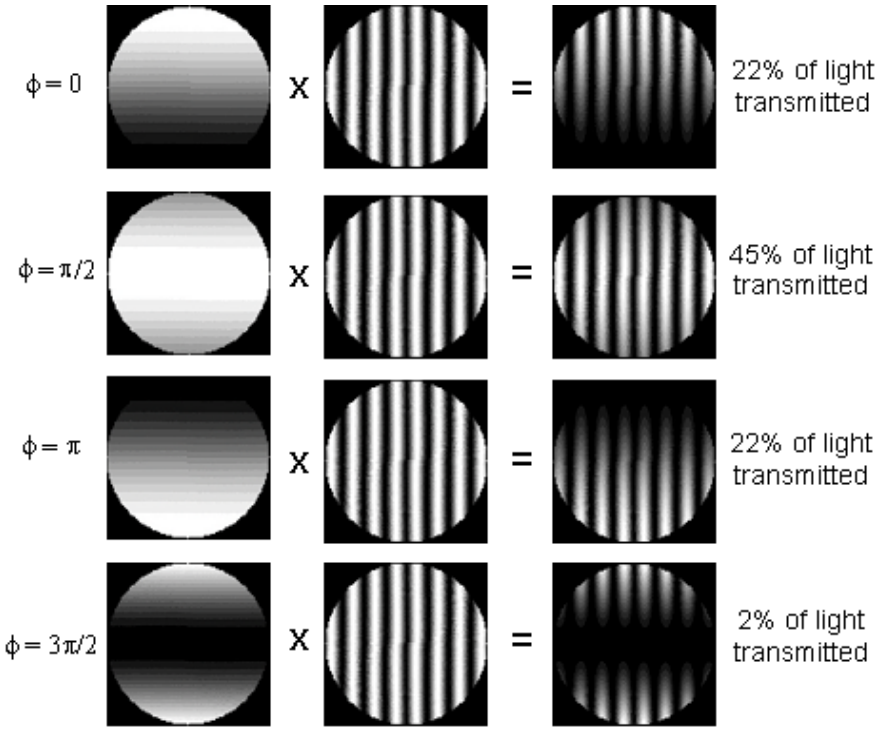

Figure 6.12: Principle of the internal chopping. The two UTs are recombined half by half, and the two resulting nulled beams are combined with a time-varying phase shift.

a first limitation to the achievement of such null depths. On top of that, we have shown in the previous sections that even with optimized control subsystems, the additional leakage due to instrumental errors will be difficult to reduce below the required 10^{-4}. Therefore, we can expect that the residual stellar signal will be an important contributor to the signal detected at the destructive output of GENIE, so that its calibration is a crucial issue. The required calibration accuracy is 1%, a value driven by the detection of hot Jupiters in the L' band (see section 7.3). Our goal will be a precision of 0.1%, especially in the L' band where stellar leakage can be very large.

One of the main goals of the GENIE simulator is to identify the required functionalities for the GENIE instrument. Preliminary simulations of scientific observations (see chapter 7) show that stellar leakage calibration is one of the most important of these functionalities. The calibration of optical interferometry data has been a continuing problem. It takes place both at hardware and data reduction level. In the next sections, we will present a few methods for stellar leakage calibration, which will be investigated with the help of the GENIE simulator in the coming months.

6.6.1 Calibration of the physical leakage

The physical leakage is given by $S_{\rm phys} = \alpha \cdot \tau_{\rm theo} \cdot F_{\lambda,*} \cdot A_{\rm tot} \cdot \Delta\lambda$, where α is the overall transmission of the interferometer, $\tau_{\rm theo}$ the theoretical stellar transmission, $F_{\lambda,*}$ the stellar flux in W/m^2/μm, $A_{\rm tot}$ the total collecting surface and $\Delta\lambda$ the waveband. The physical leakage can thus be estimated directly from the theoretical stellar transmission, provided that the interferometric transmission and the stellar flux are known (or measured with a sufficiently good precision).

6.6.1.1 Computation of the stellar transmission

The theoretical stellar transmission is given in equation 2.8:

$$\tau_{\rm theo} = \frac{\pi^2}{4} \left(\frac{b\theta_*}{\lambda} \right)^2 , \tag{6.25}$$

where b is the interferometer baseline, θ_* the stellar angular radius and λ the wavelength. The calibration precision for the physical leakage (assuming a perfect instrument) is thus equal to the precision with which the transmission $\tau_{\rm theo}$ can be computed. A good precision on the transmission requires the stellar diameter to be known with a high accuracy (the baseline and the wavelength are known with a very high accuracy). The most precise stellar diameter measurements are currently being obtained with optical/infrared interferometry. These measurements can be done at any wavelength because the apparent diameter of main sequence stars does not depend on the wavelength. Precise measurements of stellar visibilities are currently being achieved with fiber-linked instruments such as FLUOR. A routine accuracy of about 1% is reached, yielding a precision of 1 to 2% on stellar diameters for main sequence stars with an apparent diameter of about 1 mas (a Sun-like star at 10 pc has an apparent diameter of 0.93 mas). At the VLTI, the MIDI instrument will deliver a precision of about 1% on visibility measurements in the infrared N band with a spatial resolution of about 20 mas, while the AMBER instrument has a goal precision of 10^{-4} on visibility measurements in the J, H, K bands and a spatial resolution as high as 2.5 mas. AMBER is thus well adapted to measure stellar diameters as small as 0.93 mas (Sun at 10 pc) with a precision as high as 10^{-4}. Let us evaluate the precision on the physical leakage calibration that can be reached when the stellar diameter is known with a precision ε. For a stellar radius $\theta_*(1+\varepsilon)$, and assuming ε to be small compared to one, the transmission can be approximated by:

$$\tau_{\rm theo} = \frac{\pi^2}{4} \left(\frac{b\theta_*}{\lambda} \right)^2 (1 + 2\varepsilon) , \tag{6.26}$$

so that the relative error on the physical leakage is 2ε. In 2004, AMBER will deliver a precision of at least 10^{-3} on stellar diameters, so that the physical leakage can be calibrated with a precision of 2×10^{-3}.

6.6.1.2 Calibration of the interferometric transmission

In order to deduce the physical leakage from the theoretical transmission, the product $\alpha \cdot F_* \cdot A_{\rm tot} \cdot \Delta\lambda$ must be known with a sufficiently high accuracy. In practice, it can be easily measured at the constructive output of GENIE at any moment during the observation. This assumes that the optical components after the beam-combiner do not significantly contribute to the total transmission, and that the transmission and reflection coefficients of the beam-combiner are precisely known (or compensated by a double-pass architecture).

Let us estimate the accuracy with which the product $\alpha \cdot F_* \cdot A_{\rm tot} \cdot \Delta\lambda$ can be measured at the constructive output, assuming that the transmission α is the same for the constructive and the destructive output. Computations similar to those made for intensity matching in sections 6.4.1 and 6.4.2, but this time using the total amount of photons available at the constructive output, lead to the following results:

- In the N band, the stellar flux in constructive mode is about 3.6×10^7 e^-/s for a Sun-like star at 10 pc, while the background flux is about 2.6×10^{10} e^-/s. Assuming that the detector noise is negligible, the precision on the interferometric transmission is 0.45% at 1 Hz. The Strehl ratio is the only contributor to the total transmission that could vary significantly on time scales shorter than 1 s. In the N band, a Strehl fluctuation of about 0.8% is expected on a time scale of 1 s (see Table 4.5). A calibration precision of 1% is thus achievable.

- If the L' band is used, the constructive stellar flux is about 6.8×10^7 e^-/s for a Sun-like star at 10 pc, while the background flux is about 7.3×10^6 e^-/s. Assuming detector noise to be negligible, the precision on the interferometric transmission is 4×10^{-5} at 1 Hz. However, the fluctuations of the Strehl ratio are larger in the L' band than in the N band (about 5% on a time scale of 1 s), so that a higher sampling frequency is needed. A frequency of about 10 Hz is sufficient to achieve the required calibration accuracy of 1%. An optimum accuracy of 0.3% is reached at a frequency of 2 kHz.

The conclusion is that the constructive output of the beam-combiner can be used to precisely monitor the actual transmission of the interferometer, including the sky transmission, with an accuracy of 0.3% at the msec level in the L' band, and of 1% in the N band in one second.

6.6.2 Calibration of the instrumental leakage

A precise calibration of the physical leakage will generally not be sufficient to subtract the actual stellar leakage with the required accuracy of 1% because the instrumental leakage generally has an important contribution, even in the N band. Therefore, it is important to calibrate also the instrumental part of the stellar leakage. The instrumental leakage is characterized by a *mean value* which is slowly varying with time, and a *random*

component (transmission noise) due to atmospheric turbulence. The mean value of the instrumental leakage can be divided into two components:

- The *constant component* is due to the "static" imperfections of the instrument. The major contributor to this component is the effect of polarization. The amount of polarization mismatch will be estimated during the GENIE commissioning and should not change much with time. A compensator for the deterministic component could be added to GENIE during its commissioning, or at least it could be precisely characterized with internal sources. This component is thus not a major concern for stellar leakage calibration.

- The *drifting component* comes from the possible instrumental drifts (including the transmission of optical components located after the beam-combiner) and from the non-stable mean performances of the control subsystems. This component is non-deterministic because the performances of the control systems depend on the actual atmospheric conditions, and this is thus the contribution to stellar leakage that requires the most sophisticated calibration procedures.

In the following sections, three possible methods to calibrate the drifting component of stellar leakage are investigated. The first one makes use of the "traditional" calibration procedure in stellar interferometry (calibrator stars), while the last two are designed to directly measure the stellar leakage on the scientific target.

6.6.2.1 Calibrator stars

The principle of this method is very simple: the observation of the scientific target is preceded and followed by the observation of one or more calibrator stars. The instrumental stellar leakage is measured on the calibrator stars, and used to infer the instrumental leakage in the science data. A critical issue for this method is the choice (and the availability) of appropriate calibrator stars. Here are a few important points concerning this issue:

- To the first order, the instrumental leakage does not depend on stellar diameter. Indeed, we have proven that the instrumental transmission associated with a differential phase ε_φ is equal to $\varepsilon_\varphi^2/4$, while the error associated with a relative intensity mismatch ε_I is equal to $\varepsilon_I^2/16$. In principle, any kind of star could thus be chosen for calibration.

- All control subsystems use stellar photons to close their loops. Their performance thus depends on the brightness of the star. In order to be representative of the scientific target, the calibrator star should have about the same magnitude *and* spectral type[8], so that the magnitudes of the calibrator and target stars are almost

[8]Note that if the calibrator star has the same magnitude and spectral type (and luminosity class) as the target star, it also has approximately the same angular diameter.

the same from the K band up to the N band. If GENIE operates in the L' band, the constraint on stellar type is significantly relaxed.

- In order to measure the instrumental leakage on the calibrator stars, their physical leakage must be subtracted with a sufficiently high accuracy. There are two possibilities: either the physical leakage is negligible (less than 1% of the instrumental leakage) because the star is completely unresolved, or the angular radius of the calibrator star is known with a sufficiently high accuracy. In the latter case, using a calibrator star with a large angular diameter is not recommended, because the physical leakage would supersede the instrumental leakage, thereby reducing the precision on the measurement of instrumental leakage. In practice, since the physical leakage is known with a typical accuracy of 1% to 0.1% (in 2004 with AMBER), the calibrator star should be chosen so that its physical leakage is smaller than its instrumental leakage.

- The calibrator star should be in the close vicinity of the scientific target, for two obvious reasons: a long time cannot be spent in changing the telescope pointing from one star to another, and the air mass should not differ between the two measurements (because the properties of turbulence depend on the air mass).

- Of course, the environment of the star must be clean: no circumstellar dust, no giant planetary companion, and no significant infrared background source. Otherwise, leakage measurements would not be reliable.

Another key issue for calibration with nearby stars is the period that has to be chosen for the calibration measurements. With current stellar interferometers, calibration measurements are ideally performed about every 10 minutes. This ensures that instrumental characteristics do not vary significantly between target and calibrator measurements. However, the high precision needed for GENIE could make this period of time too long to reach the required calibration accuracy. This depends on the stability of the atmospheric conditions and of the control subsystem, and thus cannot be addressed before the precise design of the instrument is known. On the other hand, the integration time should be long enough to measure the instrumental leakage of the calibrator with a sufficiently high precision. Assuming that the total stellar transmission amounts to 10^{-3} as planned and taking only into account shot noise, an integration time of 20 seconds in the L' band or of 55 hours (!!) in the N band is required to reach a precision of 1% on the stellar leakage measurement in the case of a Sun-like star at 10 pc. The method thus seems *impractical in the N band*, while *well appropriate in the L' band*.

Note that the problems associated with photometric calibration generally encountered in infrared astronomy are not relevant in our case, because we measure the stellar *transmission*, i.e., the ratio of stellar flux in the destructive output to the stellar flux in the constructive output, but not the absolute stellar leakage in the destructive output.

6.6.2.2 Spectrum subtraction

This method relies on subtraction of the stellar flux from the scientific data by identifying some characteristic stellar spectral lines in the destructive output. One would for instance measure the spectrum of the star with the constructive output of the beam-combiner, and try to match the observed spectral lines to the scientific data obtained at the destructive output. In order to give a good precision, this method needs a high spectral resolution, which is probably not achievable on most targets because they are too faint. Its efficiency also depends on the stellar type, which determines the width and depth of the spectral lines in the stellar spectrum.

6.6.2.3 Real-time calibration

As for the calibration of the physical leakage, this method relies on a good knowledge of the stellar diameter. In order to compute the *actual* stellar leakage from the stellar diameter, the actual transmission map, affected by all instrumental errors, must be known. In order to achieve "real-time" calibration, the error estimates given by the sensing units of the control subsystems could be used to compute the actual transmission map and then to infer the actual stellar leakage in each detector read-out frame. The main problem with this method is that the error estimates from the control loops are generally of low accuracy. For example, in the case of OPD control, if the residual OPD is dominated by the measurement error of the FSU, the error bar on the error estimate is as large as the value itself. On the other hand, if detection noise is negligible in the control loop, the error estimates given by the FSU are accurate and can be used to compute the real-time stellar transmission. This is the case for PRIMA: Table 4.4 shows that the FSU noise σ_{FSU} is negligible compared to other contributions. This is mostly due to the fact that the VLTI Delay Lines are not fast enough to compensate for rapid fluctuations of the OPD. In the case of GENIE, where a fast Delay Line will be used, this might not be the case any more.

In conclusion, real-time calibration is a very interesting method for stellar leakage calibration, because both the instrumental and physical leakage would be calibrated at the same time, without the obligation to spend half of the time on calibration measurements. However, its feasibility strongly depends on the performances of the sensing units in the control loops and on the design of the mechanical systems for OPD, dispersion and intensity control.

Chapter 7

Observation simulations with GENIEsim

7.1 Architecture and operation of GENIEsim

The operation of GENIEsim consists in computing the real-time transmission map of the interferometer in order to deduce the total flux at the destructive output on the millisecond timescale. Since observations last typically a few minutes up to a few hours, there are five to six orders of magnitude between the smallest and the largest time scales that have to be accounted for. Practically, GENIEsim operates on Observation Blocks (OB), which are generally 100 sec long. For each OB, the simulator generates time sequences for the random variables, based on the input power spectral densities and on the transfer functions of the control loops. These sequences contain 10^5 random realizations for the wavelength-dependent phase and the intensity in the beams of the interferometer. Control loops are self-calibrated to minimize their residual errors. Taking into account all random errors, the fringe pattern is computed each millisecond, and the flux transmitted by GENIE is deduced by integration of all field sources on the transmission map. The output of GENIEsim is a time series of the fluxes recorded at each detector read-out. The operation of the GENIE simulation code is summarized in Figure 7.1.

Lacking a fancy GUI, the operation of GENIEsim is currently based on a single ASCII file where all simulation parameters are listed:

- observation parameters (date, time, ...),
- configuration (telescopes),
- chopping (external/internal, frequency, ...),
- photon parameters (wavelength, ...),
- atmospheric conditions,

- VLTI parameters (throughput, emissivity, pointing errors, ...),
- characteristics of detectors (including the detectors for the sensing units),
- description of the sources.

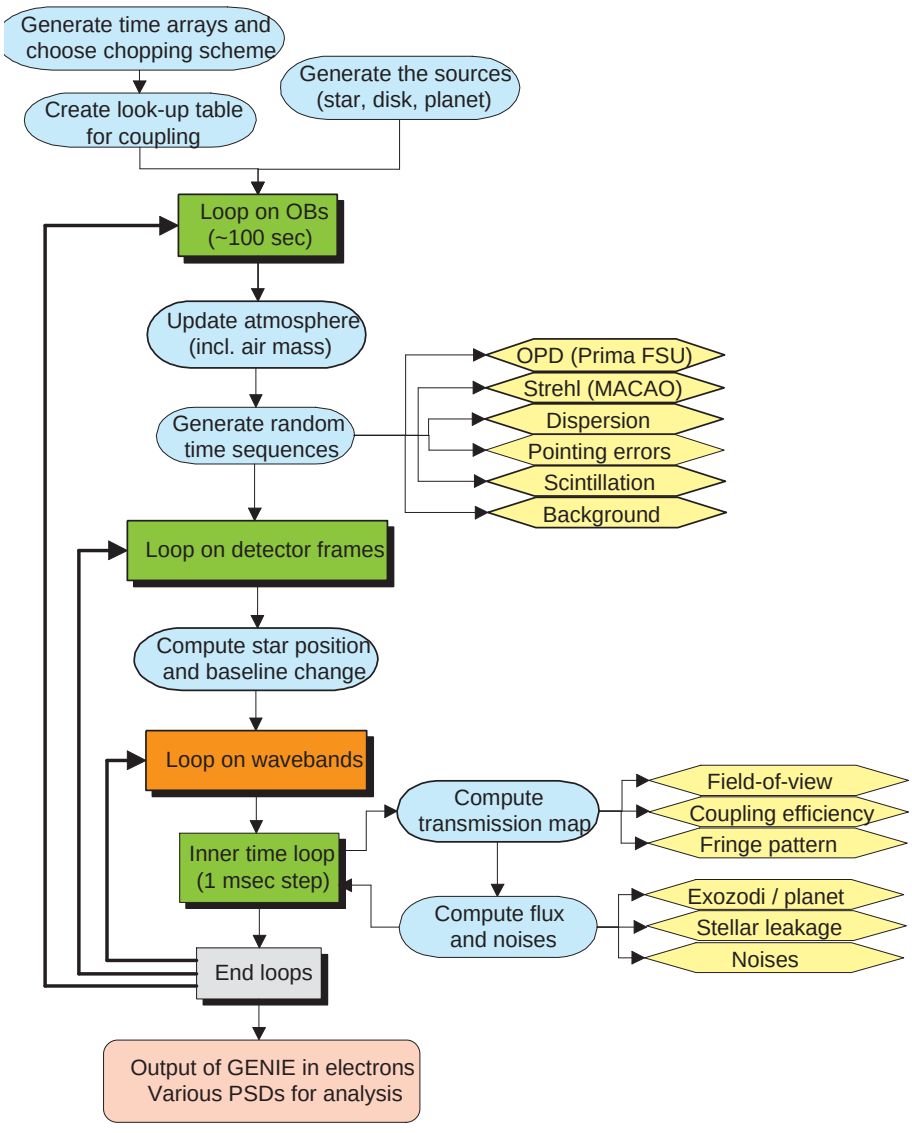

Figure 7.1: Architecture of the GENIEsim software.

7.2 Article 1: Can GENIE Characterize Debris Disks around Nearby Stars?

Observation simulations of Vega-type stars are presented in the following paper, written in collaboration with other members of the "ESA GENIE Team", and to be soon published in the proceedings of the conference: "Toward Other Earths: Darwin/TPF and the Search for Extrasolar Terrestrial Planets" (ESA Special Publication SP-539). In this paper, we show that, using GENIE with UTs in the N band or with ATs in the L' band, basic parameters of debris disks such as luminosity, inner radius or density power-law could be retrieved with a relative accuracy of 1% or better within an hour of integration. This paper also shows that, for nearby Sun-like stars, GENIE should be able to detect zodiacal disks as faint as 23 times our local zodiacal cloud.

CAN GENIE CHARACTERIZE DEBRIS DISKS AROUND NEARBY STARS?

O. Absil[1], L. Kaltenegger[2], C. Eiroa[3], R. den Hartog[2], P. Gondoin[2], R. Wilhelm[4], and M. Fridlund[2]

[1]Institut d'Astrophysique et de Géophysique, Université de Liège, Belgique (e-mail: absil@astro.ulg.ac.be)
[2]Science Payloads and Advanced Concepts Office, ESA/ESTEC, Noordwijk, The Netherlands
[3]Dpto. de Física Teórica, Facultad de Ciencias, Universidad Autónoma de Madrid, Cantoblanco, Spain
[4]European Southern Observatory, Garching bei München, Germany

ABSTRACT

The Ground-based European Nulling Interferometer Experiment will combine the light collected by two or more VLT telescopes and make them interfere in a destructive way, thereby revealing the close neighborhood of nearby stars. Operating at mid-infrared wavelengths, GENIE will be particularly sensible to warm circumstellar dust. This paper presents simulated observations of the debris disk around the nearby A2V star zeta Leporis obtained with the GENIE simulation software. Parameters such as inclination, density power-law exponent and inner radius can be retrieved with a relative precision of 1% or better using only six observations of 15 minutes. In the context of the DARWIN/TPF mission, warm circumstellar dust could be a serious limitation to the detection of Earth-like exoplanets. This paper shows that GENIE will detect disks as faint as 23 times our local zodiacal cloud around Sun-like stars at 10 pc, and will thus allow to discard unsuitable targets for DARWIN/TPF.

Key words: Debris disks; Vega-type stars: zeta Leporis; infrared; nulling interferometry; GENIE.

1. INTRODUCTION

The GENIE instrument, a common project of the European Space Agency and of the European Southern Observatory, should be installed in the interferometric laboratory of the Very Large Telescope (Cerro Paranal, Chile) in 2007. The first goals of this instrument are to validate the concept of nulling interferometry for the DARWIN/TPF mission and to perform nulling tests on single stars, with the deepest and most stable starlight rejection rate (Gondoin et al., 2003).

Besides its technological aspects, GENIE aims at surveying nearby main-sequence stars for the presence of warm dust around them, especially in their habitable zone, to prepare the science programme of the DARWIN/TPF mission by discarding unsuitable targets (i.e., those surrounded by a too large amount of dust). This survey should also bring brand new information on the inner dust component of debris disks, which is very difficult to investigate without high angular resolution.

The main-sequence stars currently known to harbor a large quantity of dust are mainly early-type stars. They were called Vega-type stars after the first discovery of an excess infrared flux around Vega by the satellite IRAS (Aumann et al., 1984). The geometrically and optically thin dust disks surrounding these stars are supposed to be continuously replenished by evaporating comets and colliding asteroids, the remnants of the proto-planetary disks being removed within a few Myr by processes such as radiation pressure, Pointing-Robertson drag or sublimation.

In this paper, we have simulated observations of a typical Vega-type star, zeta Leporis (ζ Lep hereafter), by means of the GENIEsim simulation software (Absil et al., 2003). Warm dust has already been detected around this particular star, and a model for the disk morphology is available (Fajardo-Acosta et al., 1998). Our simulated observations show that GENIE could provide an unprecedented accuracy in the modeling of the disk morphology, and thus on the physics of such disks.

2. MODELING DUST DISKS AROUND MAIN-SEQUENCE STARS

Debris disks around main sequence stars are generally modeled as flat optically thin disks, bounded by an inner radius $r_{\rm in}$ and an outer radius $r_{\rm out}$. The morphology of the dust cloud is described by the following density and temperature power-laws:

$$\rho(r_c) \quad = \quad \rho_0 \left(\frac{r_c}{r_{\rm in}} \right)^{-\alpha} \qquad (1)$$

$$T(r_c) \quad = \quad T_{\rm in}\left(\frac{r_c}{r_{\rm in}}\right)^{-\delta} \qquad (2)$$

In these two expressions, we have neglected the vertical dependence of the dust properties, and r_c represents the distance to the star projected on the ecliptic plane of the system. This is an acceptable approximation assuming that the disk is geometrically thin.

Table 1 lists the parameters with which Fajardo-Acosta et al. (1998) have modeled the hottest part of the dust disk around ζ Lep. This model reproduces 90% of the observed flux at 10.3 μm. Of particular interest is the fractional dust luminosity ($L_{\rm dust}/L_*$), the ratio of integrated excess flux emitted from the dust to integrated flux emitted from the star alone. According to Backman and Gillett (1987), this ratio is equivalent to the mean optical depth of circumstellar dust grains, and is thus an indicator of the quantity of dust around the star.

Table 1. Star and disk parameters for the Vega-type star ζ Lep.

Stellar parameters		Disk parameters	
Distance [pc]	24	$r_{\rm in}$ [AU]	0.5
V mag.	3.55	$r_{\rm out}$ [AU]	7
Type	A2V	$T_{\rm in}$ [K]	960
R_* [$R_\odot$]	2.3	$T_{\rm out}$ [K]	250
$T_{\rm eff}$ [K]	9250	α	0.6
L_* [$L_\odot$]	35	δ	0.5
		$L_{\rm dust}/L_*$	1.7e-4

3. INSTRUMENTAL CONFIGURATION

It is not currently known if GENIE will operate in the infrared L' band (3.5–4.1 μm) or N band (8–13 μm). The final choice of the operation wave band mainly depends on technological aspects and on calibration issues for background and stellar leakage (Gondoin et al., 2003). We will thus simulate observations both in the L' and N bands. Due to the huge thermal background in the mid-infrared N band, only the 8 m Unit Telescopes (UT's) will be used in this band, while in the L' band the less sensitive 1.8 m Auxiliary Telescopes (AT's) are affordable.

The simulations are done for a two-telescope Bracewell configuration. We have used the preliminary design of the GENIE instrument discussed in Absil et al. (2003), and currently implemented in the GENIEsim science simulator. This design includes control sub-systems for optical path delay, longitudinal dispersion and intensity mismatch between the two beams. The transmission map of the instrument is shown in Figure 1. The radius of the interferometric field-of-view is respectively of 277 milliarcsec (mas hereafter) for an AT in the L' band, and of 172 mas for a UT in the N band, which correspond respectively to 6.7 and 4.1 AU at the distance of ζ Lep. Thus the inner part of the cloud that we have modeled fills the field-of-view in both cases.

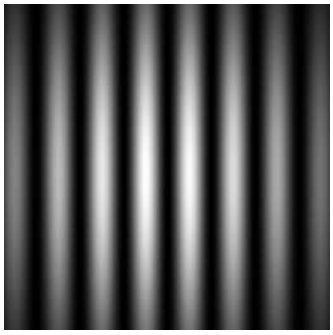

Figure 1. Transmission map of a 46 m Bracewell interferometer formed of two UT's. The spacing between two bright fringes is respectively of 17 mas and 47 mas at 3.8 μm and 10.5 μm, which correspond respectively to 0.4 AU and 1.1 AU for ζ Lep.

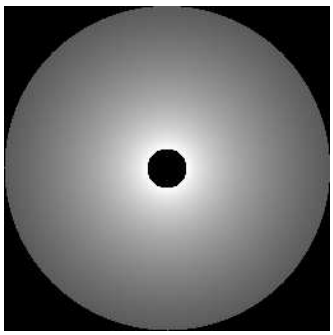

Figure 2. Simulated image of the dust disk around ζ Lep seen face-on in the N band (logarithmic scale), in the interferometric field-of-view of a UT.

4. INFLUENCE OF THE DISK PARAMETERS ON THE NULLING RATIO

Using the above model and the DISKPIC package (Absil et al., 2003), we have generated the image of the ζ Lep dust cloud within the interferometric field-of-view of AT's and UT's (see Figure 2 for a UT in the N band). A constant thickness of 0.1 AU was assumed for the dust cloud. The flux of the disk within the field-of-view is respectively of 0.18 Jy and 0.46 Jy in the L' and N bands, in agreement with the excess observed by Fajardo-Acosta et al. (1998): $<$ 0.9 Jy in the L' band, 0.43 Jy in the N band.

In the following paragraphs, we have generated images of the dust cloud with different parameters, to assess the influence of each disk parameter on the theoretical nulling ratio. The *nulling ratio* is defined as the ratio of the total flux collected in destructive

mode to the total flux in constructive mode (i.e., without the π phase shift between the arms of the interferometer). The nulling ratio is called "theoretical" because noise is not taken into account.

The simulated observations are performed when the star crosses the local meridian, at a zenithal distance of 9°48'. Such a small zenithal distance ensures that the projected baseline on the plane of the sky has approximately the same length as the actual baseline, e.g. 46.65 m for the UT2-UT3 pair. These simulations are only performed in the N band—the L' band would give the same qualitative results. The only difference between the two bands is that the *physical leakage*, i.e., the theoretical leakage from the stellar light, is negligible in the N band while not in the L' band due to higher angular resolution (especially for long baselines). If the stellar diameter is known with a high enough accuracy, the physical leakage can be removed from the nulling ratio to reveal the contribution of the disk itself. Otherwise, the stellar diameter needs to be fitted together with the disk parameters.

4.1. Influence of inclination

We have generated images of the dust cloud with different inclinations, ranging from 0° (face-on) to 90° (edge-on), and we have computed the theoretical nulling ratio for these configurations. Figure 3 shows the evolution of the nulling ratio as a function of the baseline orientation for different inclinations of the disk. The baseline angle is counted clockwise with respect to the N-S direction. A position angle of 0° was assumed for the dust cloud (i.e., major axis along the N-S direction). For low inclinations, the nulling ratio is not affected by the baseline orientation, because the disk image has nearly circular symmetry. For high inclinations, the flux in destructive mode drops dramatically when the dark fringe and the major axis of the disk are superposed (baseline angle of 90°).

4.2. Influence of the morphology

In Figures 4 and 5, we have used different values of the density power-law exponent α and of the inner radius $r_{\rm in}$ to generate the cloud images. The nulling ratio has been computed for different baseline lengths ranging from 40 m to 140 m. The influence of the inner radius on the nulling ratio is remarkable: the maxima of the curves in Figure 4 correspond to the baselines at which a bright fringe is superposed on the inner component of the dust cloud (brightest part of the cloud). On the other hand, the density power-law exponent has a smaller influence on the nulling ratio: the position of the maximum does not change any more, and the behaviour of the nulling ratio with increasing baselines is similar for all values of α. Retrieving this parameter from nulling measurements will not be easy.

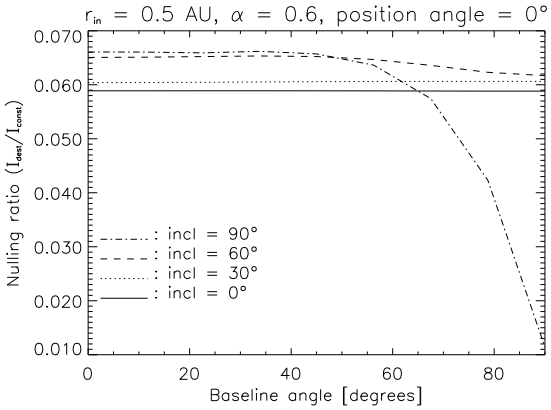

Figure 3. The evolution of the nulling ratio for different baseline orientations is remarkable for high inclinations: when seen edge-on, the disk is strongly cancelled by a dark fringe for a baseline angle of 90°.

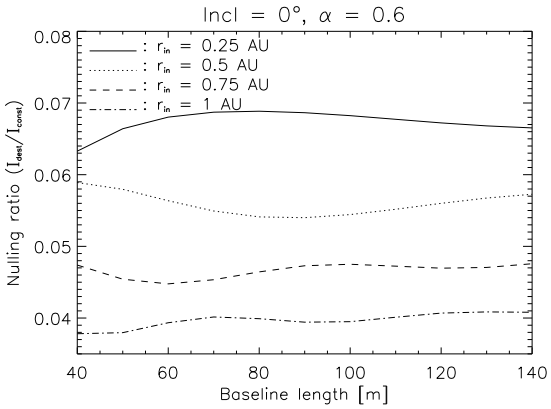

Figure 4. The influence of the dust inner radius is remarkable: the nulling ratio is maximum when a bright fringe transmits the large flux produced by the hot dust located at the inner cut-off.

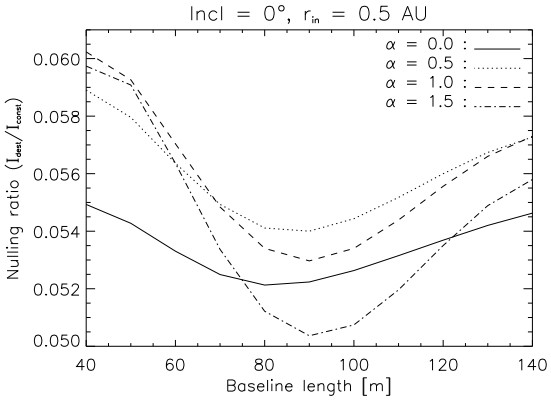

Figure 5. The behaviour of the nulling ratio for different density power-laws does not differ much. The difference would be more visible if the inner radius was not resolved (i.e., for baselines < 40 m in the N band, or baselines < 15 m in the L' band).

5. SIMULATED OBSERVATIONS

Now that we have investigated the influence of each parameter on the nulling ratio, we will simulate observations of ζ Lep with the GENIEsim software, taking into all noise sources discussed in Absil et al. (2003), and try to retrieve the disk parameters from these observations. The observations will be done with different baselines to get as much information as possible on the cloud morphology. In these simulations, we have assumed a face-on disk, so that the baseline orientation does not matter.

5.1. Calibration of the stellar leakage

When realistic simulations are carried out, a major source of signal in the destructive output of GENIE is the *instrumental leakage*, i.e., the additional stellar signal which leaks through the null because of residual OPD, dispersion, intensity mismatches, etc. Instrumental leakage can be much larger than the signal from the dust disk, especially in the L' band. Therefore, to retrieve the actual nulling ratio from the observations, one must calibrate the raw nulling ratio with a reference star.

In the following simulations, we will assume that a calibrator star, perfectly identical to the target star except for the absence of dust, is observed before and after the target star. The observation time is set to 1000 sec, so that two calibrator measurements are separated by 1000 sec. The calibration is done as follows:

1. Compute the mean stellar leakage for the two calibrator measurements,
2. Compute analytically the physical leakage associated to the calibrator, knowing its angular diameter,
3. For the calibrator star, subtract the physical leakage from the mean leakage to retrieve the instrumental leakage,
4. Compute the estimated instrumental leakage associated to the target star from the instrumental leakage associated to the calibrator,
5. Subtract the estimated instrumental leakage from the data to retrieve the actual nulling ratio.

The most critical step in this method is the second step because the angular diameter of the calibrator has to be known with a high enough accuracy. The fourth step could also be problematic because the relationship between the instrumental leakage associated to the calibrator and to the target star is not straightforward. In practice, it turns out that the instrumental leakage does not depend much on the angular diameter of the star, which is quite comprehensible. In the following simulations, we will avoid these problems by assuming that the angular radius of the calibrator is perfectly known and that the calibrator is identical to the target star. The result will be too optimistic in the L' band where stellar leakage is critical, but not in the N band where the instrumental leakage is much smaller than the signal from the dust cloud.

5.2. Calibration of the thermal background

Besides stellar leakage, the thermal background also has an important contribution to the signal detected at the destructive output of GENIE (Absil et al., 2003). In order to remove this incoherent contribution, chopping will be used by GENIE, either with the help of the VLTI chopping mirrors for which the chopping frequency is limited to 5 Hz, or by using internal chopping (e.g. with phase modulation) at a higher frequency.

In the following simulations, we will assume that the noise due to the residual background after calibration is negligible compared to other noise sources, and especially to the shot noise associated to the background. This is the "background-limited performance" regime. The resulting signal-to-noise ratio could be somewhat optimistic, especially in the N band where the thermal background is a critical issue.

5.3. L' band simulations

Ten observations of 1000 sec in the L' band, with ten different AT baselines ranging from 8 m to 112 m, have been carried out on successive nights at the moment when ζ Lep crosses the local meridian. After calibration of the instrumental leakage, a signal-to-noise ratio of 300 on the dust emission is reached for each observation. Figure 6 shows the observed nulling ratios together with their 1-σ error bars. In the top plot of Figure 6, the physical leakage has not been removed from the data, so that the nulling ratio increases with increasing baselines as the star gets more and more resolved.

Three disk parameters (luminosity ratio, inner radius and density power-law) have been fitted to the observations. The resulting parameters are very close to the theoretical ones (cf. Table 2), with a relative error of less than 1% on their values.

Table 2. Three disk parameters have been fitted to the observed nulling ratios in the L' band (Figure 6).

	Model	Fitted	Error (1σ)
$L_{\rm dust}/L_*$	1.7e-4	1.694e-4	0.003e-4
α	0.6	0.593	0.004
$r_{\rm in}$ [AU]	0.5	0.4988	0.0006

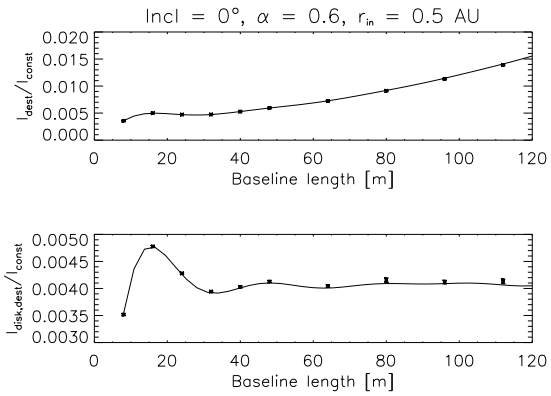

Figure 6. Solid line: theoretical nulling ratio for ζ Lep in the L' band. Data points: simulated observations of ζ Lep, with ten AT-AT baselines. Each observation of 1000 sec gives an SNR of 300 (in the whole L' band). In the bottom plot, the physical leakage from the stellar light has been removed to reveal the contribution of the disk to the nulling ratio.

5.4. N band simulations

Six observations of 1000 sec in the N band with the six different UT baselines have been carried out on successive nights at the moment when ζ Lep crosses the local meridian. Even with only 10% accuracy on the calibration of the instrumental leakage, a signal-to-noise ratio of 450 on the dust emission is reached for each observation. Figure 7 shows the observed nulling ratios together with their 1-σ error bars.

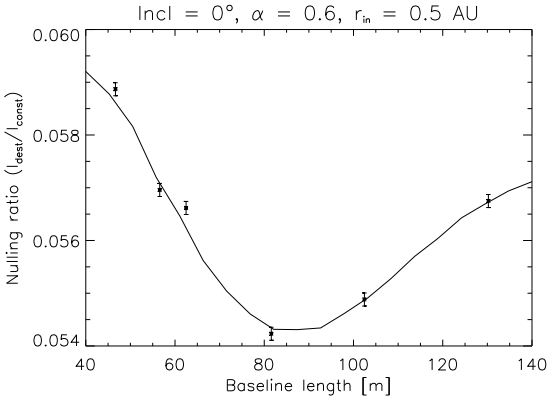

Figure 7. Solid line: theoretical nulling ratio for ζ Lep in the N band. Data points: simulated observations of ζ Lep, with the six possible UT-UT baselines. Each observation of 1000 sec gives an SNR of 450 (in the whole N band).

Three disk parameters (luminosity ratio, inner radius and density power-law) have been fitted to the observations. The resulting parameters are very close to the theoretical ones (Table 3), with a relative error of 4% or less on their values. Note that the error on the morphology parameters α and $r_{\rm in}$ is larger in the N band than in the L' band. This is due to the smaller range of baselines and to the lower angular resolution in the N band.

Table 3. Three disk parameters have been fitted to the observed nulling ratios in the N band (Figure 7).

	Model	Fitted	Error (1σ)
$L_{\rm dust}/L_*$	1.7e-4	1.7022e-4	0.0017e-4
α	0.6	0.645	0.025
$r_{\rm in}$ [AU]	0.5	0.5025	0.003

Both the L' and N bands allow to retrieve the disk parameters with a very high precision. With such a precision, the possible presence of gaps due to the formation of terrestrial planets could probably be inferred. Moreover, low spectral resolution will be available on GENIE and will bring additional information, e.g. on the size of the grains.

6. SURVEY OF NEARBY STARS

6.1. Vega-type stars

Among the nearby stars that will be surveyed by GENIE are at least 40 Vega-type stars. Figure 8 gives the distances and luminosity ratios for the known Vega-type stars within 100 pc that can be observed from Cerro Paranal. This is a non-exhaustive list, and many more debris disks could be detected by GENIE and other instruments in the coming years.

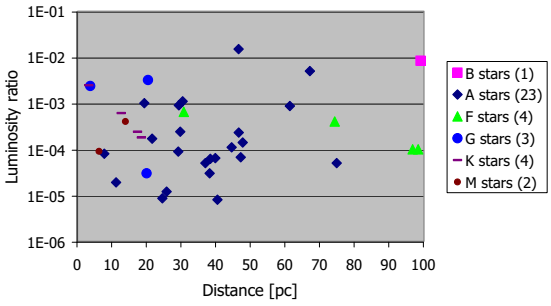

Figure 8. Known Vega-type stars within 100 pc. Debris disks are particularly frequent around A-type main sequence stars (∼10%).

6.2. Zodiacal disks

As mentioned in the introduction, the main scientific goal of the GENIE instrument is to survey the candidate DARWIN/TPF targets for the presence of circumstellar dust. Using the GENIE simulator

Table 4. Limiting number of zodis for detection of exozodiacal dust around G2V stars at different distances. The unit "zodi" corresponds to a fractional luminosity of 4×10^{-7}. The detection limit corresponds to an SNR of 3 in one hour of integration with two AT's in the L' band or two UT's in the N band.

	5 pc	10 pc	20 pc	50 pc
L' band	8	38	205	1113
N band	6	23	106	1360

and the ZODIPIC package to produce images of exozodiacal dust disks (Kuchner and Serabyn, 2001), we have computed the smallest dust fractional luminosities that can be detected with the GENIE instrument around a G2V star at different distances. In Table 4, the limiting fractional luminosity is expressed in number of "zodis", a unit corresponding to the fractional luminosity of the local zodiacal cloud $L_{\rm zodi}/L_{\odot} \simeq 4 \times 10^{-7}$.

The values in Table 4 are probably somewhat optimistic because:

- In the L' band, we have considered that a calibration accuracy of 0.1% can be reached for the instrumental leakage (this is our goal for an L'-band GENIE). This is particularly critical for the nearest stars, for which stellar leakage is huge. Assuming a more pessimistic calibration accuracy of 1%, the detection limit would increase to 80, 114, 340 and 1190 zodis for Sun-like stars at 5, 10, 20 and 50 pc respectively.

- In the N band, we have assumed background-limited performances. It is not clear yet whether chopping at a frequency of 5 Hz can fulfill this requirement. A measurement campaign is currently undertaken at the VLTI with the MIDI instrument to answer that question. If background fluctuations turns out to be the limiting factor, the use of internal chopping is a promising solution.

Table 4 has been obtained for a G2V star. Since the brightness of the dust disk increases with stellar effective temperature, the detection limit would be lower for A stars. For example, the detection limit for a dust disk around an A0V star at 20 pc is of only 10 zodis both in the L' and N bands. On the other hand, the detection limit would be much higher for M stars. For example, the detection limit for a dust disk around an M0V star at 5 pc is respectively of 150 zodis and 70 zodis in the L' and N bands. According to these limits, it turns out that almost all dust disks of Figure 8 can be detected with GENIE.

7. CONCLUSION

Vega-type stars have been detected so far solely by infrared photometry and/or sub-mm interferometry. Using infrared *nulling* interferometry, the starlight can be cancelled by a factor of 1000 or more so that the measurement of the disk emission can be performed with an unprecedented accuracy. This will allow to constraint unambiguously the morphology and the physics of warm dust, especially in the habitable zones of nearby main sequence stars. The ability to detect faint zodiacal disks around late-type stars will also allow GENIE to discard unsuitable targets for DARWIN/TPF.

ACKNOWLEDGMENTS

OA acknowledges the financial support of the Belgian National Fund for Scientific Research.

REFERENCES

Absil O., den Hartog R., Erd C., et al., 2003, these proceedings.

Aumann H., Gillett F., Beichman C., et al., 1984, ApJ 278, L23-L27

Backman D., Gillett F., 1987, in Cool Stars, Stellar Systems, and the Sun, ed. J. Linsky & R. Stencel (Berlin: Springer), 340.

Den Hartog R., Absil O., Kaltenegger L., et al., 2003, these proceedings.

Fajardo-Acosta S., Telesco C., Knacke R., 1998, AJ 115, 2101-2121.

Gondoin P., Absil O., Fridlund M., et al., 2003, Proc. SPIE 4838, 700-711.

Kaltenegger L., Absil O., Eiroa C., et al., 2003, these proceedings.

Kuchner M., Serabyn E., accepted for publication in ApJ, 2001.

7.3 Article 2: Could GENIE Detect Hot Jupiters?

The following paper, written in collaboration with other members of the "ESA GENIE Team", shows that low resolution spectra could be obtained with GENIE on a few hot Jupiters. In a L'-band single Bracewell configuration, GENIE could detect the hot Jupiter around τ Bootis in a few hours time with a signal-to-noise ratio of about 80. This paper will be published in the proceedings of the conference: "Toward Other Earths: Darwin/TPF and the Search for Extrasolar Terrestrial Planets" (ESA Special Publication SP-539).

COULD GENIE DETECT HOT JUPITERS?

Roland den Hartog[1], O. Absil[2], L. Kaltenegger[1], P. Gondoin[1], R. Wilhelm[3], M. Fridlund[1]

[1]*Science Payloads and Advanced Concepts Office, European Space Agency, ESTEC, Noordwijk,The Netherlands*
[2]*Institut d'Astrophysique et de Géophysique, Université de Liège, Belgium*
[3]*European Southern Observatory, Garching bei München, Germany*
E-mail: rdhartog@rssd.esa.int

ABSTRACT

The prime objective of GENIE (**G**round-based **E**uropean **N**ulling **I**nterferometry **E**xperiment) is to obtain experience with the design, construction and operation of an IR nulling interferometer, as a preparation for the DARWIN / TPF mission [1]. In this context, the detection of a planet orbiting another star would provide an excellent demonstration of nulling interferometry. Doing this through the atmosphere, however, is a formidable task. In this paper we assess the prospects of detecting, with nulling interferometry on ESO's VLT, a Hot Jupiter, a giant planet in a close orbit around its parent star. First we discuss the definition of the optimal target. Then we present a simulated observation of the Tau Bootis system, which suggests that GENIE, in a L′-band single Bracewell configuration, could detect the hot Jupiter in a few hours time with a signal-to-noise ratio of up to ~80. Although there are strong requirements on the control-loop performance, background subtraction and accuracy of the photometry calibration, we conclude that at present there do not seem to be fundamental problems that would prevent GENIE from detecting hot Jupiters. Hence the answer to the question in the title is **yes.**

1. INTRODUCTION

GENIE is a collaboration between ESO and ESA, and intended for commissioning on the VLTI in 2007. It is presently in its definition phase. In order to assess its performance, to assist in the requirements definition and to prepare science studies, we have developed a GENIE science simulator , GENIEsim [2]. Its inputs consists of specifications for the interferometer configuration, target source, observational scenario, atmospheric conditions, detector and control loop performance. The outputs are a series of detected photon-electron numbers (for constructive and destructive interference modes) as a function of time and wavelength, mimicking actual CCD output. The challenge we are facing is to extract from this output convincing evidence for the presence of a planet.

Even for a single Bracewell configuration, the VLTI allows quite some combinations between baseline and IR wavelength band. The 93 planetary systems identified so far with radial velocity or occultation methods, show star-planet separations ranging from 0.02 to several AU [6]. It is therefore a priori not obvious which combination between baseline, wavelength band and target will provide the best detection opportunity and a careful selection of the target is part of the preparation of the simulation.

2. TARGET SELECTION

The strategy we apply here is to first define the best possible target in terms of distance, spectral type, and orbital period, and then to see if there is a candidate on the list of stars with planetary systems that fits the description. The optimal target for a nulling interferometry experiment is close by, has a bright planet around a relatively dim star, with a contrast that is maximum for the chosen wavelength band, and with a separation that is matched to the interferometric pattern. There is some internal conflict in these requirements: a bright planet requires either a hot, bright star, which diminishes the contrast, or an as small as possible separation, which may put the planet inside the nulled part of the interferometric pattern. Moreover, massive, hot, bright stars are generally at greater distances than light, cool, dim stars. Also, while nulling interferometry at longer wavelengths relieves the requirements on the stability of the null, the atmospheric background noise is more severe. For an optimal target, these conflicting requirements are traded off against each other. Table 1 shows the results of such an exercise. As the figure of merit, we have chosen the signal-to-noise ratio for the detection of a planet, which is defined as:

$$\frac{S}{N} = \frac{S_p}{\sqrt{S_p + \sigma_{bg}^2 + \sigma_{leak}^2 + \sigma_{RON}^2}} \propto \sqrt{t} \qquad (1)$$

where S_p is the planetary signal, σ^2_{bg} is the variance of the background due to atmosphere and instruments,

σ^2_{leak} is the variance of the star light that is transmitted (leaked) by the nuller, and σ_{RON} is the rms read-out noise of the CCD detector. The variances σ^2_{bg} and σ^2_{leak} actually consist of the sum of two terms, one representing the pure Poissonian noise and equaling the average signal level, while the other is associated with the fluctuations of the detected intensity due to, in this case, fluctuating atmospheric and instrumental conditions [3].

The S/N ratio was evaluated for a single Bracewell configuration consisting of two UT telescopes, and varying the wavelength band, the baseline, the stellar temperature, the distance and the orbital period of the planet. In order to streamline this search through a five-dimensional parameter space, some simplifying assumptions were necessary. Instead of using the full GENIEsim code, we used analytical approximations to obtain values for the stellar leakage and associated noise [4]. The non-Poissonian fluctuations of the background noise are neglected in this particular approach (see below). Additional assumptions are: the planet is assumed to be in thermal equilibrium with the star; the size of the planet is equal to Jupiter (cf. [5]); the minimum orbital period is 3 days; and the minimum distance at which main-sequence M, K, G, F and A stars can be found are respectively 4, 10, 12, 14 and 25 pc (based on the statistics of stars accessible from Paranal).

From Table 1 it becomes clear that the best S/N ratio is to be expected for an L' band observation with a fairly long baseline of 89.4 m. This table also shows several trends, related to the trade-offs discussed before. The rms leakage, σ_{leak}, is (approximately) proportional to $\alpha=\pi\theta_* B/\lambda$, where θ_* is the angular size of the stellar disk and B the baseline projected onto the sky. As a consequence, σ_{leak} decreases with increasing λ, which explains the difference in obtainable S/N ratio between K and L′ band. Inside the K-band the loss of signal is traded against decrease in leakage when the star is further away. For the longer baselines the S/N ratio will not improve for A stars, because the increase in planetary flux (due to higher temperatures) does not compensate the extra leakage due to a larger stellar disk. In the M and N′ band advantage of lower leakage is undone by the increased noise from the background, which completely dominates the N′ band results.

Table 1. Estimated best signal-to-noise ratio for the detection of hot Jupiters (bold face), as a function of baseline and wavelength band, obtainable in 10^4 s. Next line, null depth, defined as the total stellar flux divided by the flux transmitted through the nulling interferometer, and modulation is defined as the ratio of maximum and minimum transmission. Then, stellar temperature in K, and spectral type. Finally, distance in pc and orbital period of the hot Jupiter, in days. All planets are one Jupiter radius in size, cf. [5].

S/N ratio in 10^4 sec null depth / modulation T_{star} / spectral type distance [pc] / period [d]			Baseline					
			UT 1–4 130.2 m	UT 1–3 102.4 m	UT 2–4 89.4 m	UT 3–4 62.5 m	UT 1–2 56.6 m	UT 2–3 46.6 m
Band	λ_{cen} [μm]	$\Delta\lambda$ [μm]						
K	2.2	0.4	**20.1** 283 / 239 7400 / F0 37.5 / 3.0	**20.1** 283 / 239 7400 / F0 29.5 / 3.0	**20.1** 288 / 241 7400 / F0 26.0 / 3.0	**20.1** 283 / 240 7400 / F0 18.0 / 3.0	**20.1** 289 / 242 7400 / F0 16.5 / 3.0	**20.0** 321 / 250 7400 / F0 14.5 / 3.0
L′	3.8	0.6	**82.0** 284 / 277 5700 / G3 15.0 / 3.0	**87.8** 329 / 308 5600 / G4 12.5 / 3.0	**88.1** 402 / 339 5700 / G3 10.5 / 3	**76.4** 662 / 396 6000 / G0 12.5 / 3.3	**71.8** 778 / 432 6000 / G0 12.5 / 3.5	**62.5** 1047 / 528 6000 / G0 12.5 / 4.3
M	4.8	0.6	**67.1** 227 / 219 7400 / F0 14.5 / 3.0	**60.1** 354 / 295 7400 / F0 14.5 / 3.3	**54.3** 452 / 377 7400 / F0 14.5 / 4	**51.0** 477 / 454 3400 / M1 4.5 / 3	**47.9** 569 / 502 3400 / M1 4.5 / 3	**39.6** 791 / 566 3400 / M1 4.5 / 3
N′	11.25	2.5	**8.7** 612 / 532 3400 / M1 4.5 / 3.0	**6.7** 939 / 743 3400 / M1 4.5 / 3.8	**5.7** 1187 / 923 3400 / M1 4.5 / 3.8	**3.7** 2124 / 1483 3400 / M1 4.5 / 6.8	**3.2** 2468 / 1657 3400 / M1 4.5 / 7.5	**2.5** 3243 / 2024 3400 / M1 4.5 / 9.3

Table 2. Properties of the currently most promising, spectroscopically confirmed, Hot Jupiter targets [5, 6].

	Star								Planet					
Name	Spectr type	Temp. [K]	dist. [pc]	Mass [$M_\odot$]	Rad. [$R_\odot$]	Lum. [$L_\odot$]	α	δ	M sin*i* [M_J]	period [d]	e	a [AU]	T_{eff} [K]	Radius [R_J]
Tau Boo b	F7V	6276	17	1.42	1.22	3.2	13:47:15.7	+17:27:25	4.14	3.313	0.016	0.045	1600	1
HD179949 b	F8V	6194	27	1.24	1.18	2.18	19:15:33.2	–24:10:46	0.93	3.092	0.00	0.047	1540	1
Gliese 86 b	K1V	5070	13	0.79	0.82	0.50	02:10:25.9	–50:49:25	4.9	15.8	0.04	0.117	660	1

The jump from M1 dwarf to F0 star in the M band is again a result of the trade-off between stellar radius and planetary flux, which are both larger for hotter stars. The general trend for the nulling depth and modulation ratio to improve with decreasing baseline, is due to the fact that both these ratios have a denominator proportional to the leakage signal, which is itself (approximately) proportional to α^2. Table 1 clearly demonstrates that there is no relation between the nulling depth or modulation ratio and the actual S/N ratio for planetary detection.

We have attempted to find a matching target from the list of stars with confirmed planets [6], and found that Tau Bootis matches best the properties for the highest S/N detection in Table 1, and is accessible from Paranal in Chile. Its properties are summarized in Table 2, together with two other likely candidates. A detailed simulation of its detection with GENIEsim is discussed in the next section.

3. PERFORMANCE OF A SINGLE-BRACEWELL CONFIGURATION

Fig. 1a illustrates the output of a simulation of a one-hour Tau Boo b observation with GENIEsim for a single Bracewell formed by UT's 2 and 4. For five different wavelengths in the L′-band range the total detected output signal in detected electrons is shown. Note that the signal is boxcar averaged over a 60 sec. bin. The decline of the signal is due to the motion of the source across the sky. In Fig. 1b the S/N ratio for the different wavelengths is shown as a function of time. After one hour integration, the S/N ratios lie in the range from 51 to 77, which is in good agreement with the preliminary estimates in Table 1. Fig. 1c compares the different noise sources to the planetary signal, showing that the noise due to stellar leakage and IR background are comparable, and dominate the S/N ratio.

One of the main tasks of GENIE is to correct for optical path differences (OPD) between the two arms of the interferometer, which enhance the stellar leakage. In GENIEsim we currently distinguish four main sources: *a.* static, due to a small phase error in the achromatic phase shifter, (~7 mrad [9]); *b.* wavelength-independent OPD fluctuations, due to the atmospheric piston effect, with a rms value of about 24 nm / 40 mrad (after correction by the VLTI and additional GENIE OPD control loops); *c.* wavelength-dependent OPD fluctuations, due to water-vapour dispersion [7, 8], with a rms value of 21 nm / 34 mrad after the GENIE control loop; *d.* intensity fluctuations between the two arms, due to Strehl ratio and scintillation fluctuations, with a rms value of 0.014 after the VLTI MACAO and GENIE control loops. Although the precise values of these errors remain debatable, it is clear that technical solutions do exist and can be implemented for these effects.

More fundamental is the problem of the IR background fluctuations. While the instrumental background stems from a thermally stabilized environment, the atmospheric background is uncontrollable. The average background can be instantaneously subtracted from the signal, e.g. by placing two additional fibers on either side of the science fiber in the focal plane. Assuming that the background is highly correlated over a few arcsec., this method can even deal with a fluctuating background. This is done in the current runs of GENIEsim. However, the photon noise from the background cannot be calibrated away and will reduce the S/N ratio (see Fig. 1c).

Comparing the signal with and without the planetary contribution shows that in order to actually disentangle the planetary signal from the other contributions, accurate photometry is required. Moreover, the photometry has to be stable over hours to days, as the modulation of the planetary signal takes place on these timescales. Fig. 1a shows that in order to detect the planet, this calibration should have a (relative) accuracy better than 1%. We have several options to accomplish this.

- Calibration of the signal with an (unresolved) star of same spectral type is a first step. This will reduce the problem from absolute to relative calibration.
- Next the comparison of the constructive and destructive spectrally resolved signals will tell us whether the nulled signal contains spectral features indicative of the presence of a planet.
- Thirdly, modulation of the OPD might indicate whether the stellar leakage is due to bad nulling or the presence of a planet.
- And finally, if everything else fails, we could consider calibrating the stellar leakage with a double Bracewell configuration. This would imply a major complication, because in order to combine the signals from four telescopes, not one, but actually three GENIEs are required.

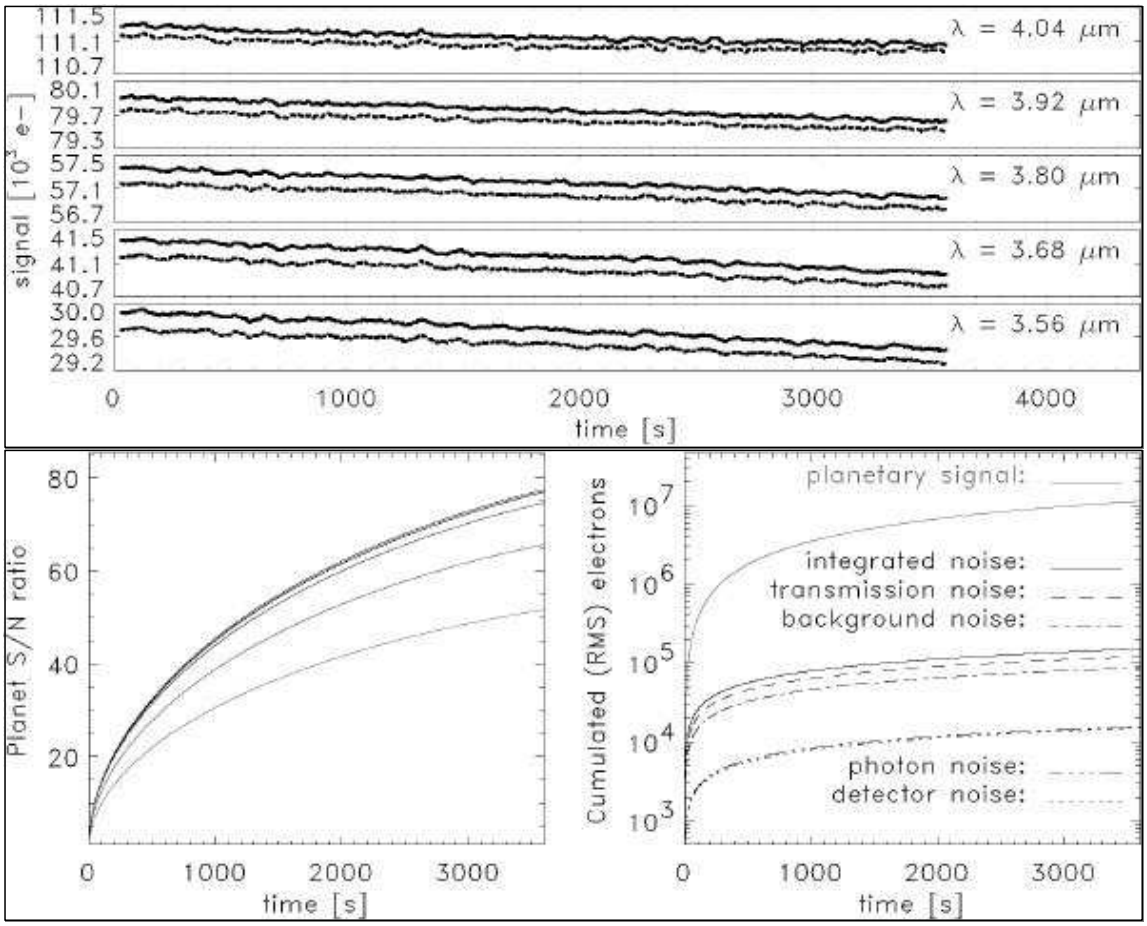

Fig. 1 ***a.*** Simulated total detected signals, for different wavelengths, with (solid) and without (dotted) the planetary light. Time series were boxcar averaged over 60 sec. ***b.*** Expected signal-to-noise ratio's for the planetary detection, for different wavelengths (dark: 4.04 mm, light: 3.56 mm). ***c.*** Various noise sources compared to the planetary signal. Note that background noise includes the background photon noise.

4. CONCLUSIONS

In this paper we discuss the simulated observation of Tau Bootis, a nearby star for which the presence of a massive planet in close orbit has been inferred spectroscopically. These simulations suggest that GENIE, in a L'-band single Bracewell configuration, could detect the hot Jupiter in a few hours time with a signal-to-noise ratio of about 80. There are, however, several provisions. The first is that the proposed control loop performances and background subtraction are feasible in reality. The second is that the nulled signal photometry can be calibrated to within a per cent accuracy, in order to infer the presence of the planet from the light-curve modulation. In a second stage, spectral features can be used to perform planetary spectroscopy. At present there do not seem to be fundamental problems that would prevent GENIE from detecting hot Jupiters.

5. REFERENCES

1. P. Gondoin, O. Absil, M. Fridlund *et al*., Proc. SPIE **4838**, 700 (2003).
2. O. Absil, R. den Hartog, P. Gondoin *et al*., this conference.
3. J. Goodman, *Statistical Optics*, John Wiley & Sons Inc., chap. 9 (1985)
4. P. Gondoin, internal communication (2002)
5. A. Burrows et al., Rev. Mod. Phys. **73**, 719 – 765 (2001)
6. http://www.obspm.fr/encycl/catalog.html (by J. Schneider)
7. J. Meisner and R. le Poole, SPIE **4838**, 609 (2003).
8. C. Koresko *et al*., SPIE **4838**, 625 (2003).
9. TNO TPD, *Achromatic Phase Shifter Final Presentation*, 27 March 2002

Conclusions

In this thesis, we have presented the physical and technical foundations of the GENIE instrument and how future observations can be simulated with a very high fidelity, taking into account all noise sources encountered in ground-based infrared interferometry. In particular, we have shown that the foreseen performances of the VLTI in 2007 (when GENIE is supposed to come on-line) are not sufficient to meet the tight requirements on the depth and stability of starlight rejection imposed on the GENIE instrument. Therefore, dedicated control loops must be devised to reduce the harmful effects of the residual atmospheric turbulence, namely differential phase errors and intensity mismatches between the beams of the interferometer. The preliminary design and the expected performance of such control loops have been discussed thoroughly in the present thesis, leading to the conclusion that optimized control subsystems should allow to meet the GENIE requirements both in the L' band and in the N band. A few open questions remain, especially regarding the calibration of the thermal background and residual stellar signals, as well as the availability of fast compensation devices such as optical delay lines, dispersion correctors and intensity matching devices. Provided that these issues can be solved by means of the methods proposed here, nothing seems to prevent GENIE from detecting and characterizing faint circumstellar disks and bright exoplanets with low resolution spectroscopy in a near future.

Bibliography

[AB81] D. Allen and J. Barton, *A study of sky noise, 1.5 $\mu m - 5\ \mu m$*, Pub. A.S.P. **93** (1981), 381–384.

[ABC+02] F. Allard, I. Baraffe, G. Chabrier, T. Barman, and P. Hauschildt, *Spectra and Evolution of Extrasolar Planets*, SF2A-2002: Semaine de l'Astrophysique Francaise, June 2002, pp. 539–542.

[Abs01] O. Absil, *Nulling interferometry with IRSI-Darwin: detection and characterization of Earth-like exoplanets*, June 2001, End-of-studies dissertation for the degree of "Ingénieur physicien", Université de Liège.

[Abs02] O. Absil, *GENIE: Study of aperture configurations*, Tech. report, ESA/ESTEC, July 2002.

[BHLL01] A. Burrows, W. Hubbard, J. Lunine, and J. Liebert, *The theory of brown dwarfs and extrasolar giant planets*, Rev. Mod. Phys. **73** (2001), no. 3, 719–766.

[BP93] D. Backman and F. Paresce, *Main sequence stars with circumstellar solid material: The Vega phenomenon*, Protostar and Planet III (E.H. Levy & J.I. Lunine, ed.), Tucson, Univ. of Arizona Press, 1993, pp. 1253–1304.

[BP03] P. Bordé and G. Perrin, *Updated results on prototype chalcogenite fibers for 10 micron wavefront modal filtering*, Toward Other Earths: Darwin/TPF and the Search for Extrasolar Terrestrial Planets, vol. SP-539, ESA's Publication Division, 2003, in press.

[Bra78] R. Bracewell, *Detecting nonsolar planets by spinning an infrared interferometer*, Nature **274** (1978), 780.

[Cas01] F. Cassaing, *Optical path difference sensors*, C. R. Acad. Sci. Paris **2** (2001), no. IV, 87–98.

[CdF94] V. Coudé du Foresto, *Interférométrie astronomique infrarouge par optique guidée monomode*, Ph.D. thesis, Université de Paris VII, July 1994.

[Cid96] P. Ciddor, *The refractive index of air: new equations for the visible and near infrared*, Appl. Opt. **35** (1996), no. 9, 1566–1573.

[CRM95] J.-M. Conan, G. Rousset, and P.-Y. Madec, *Wave-front temporal spectra in high-resolution imaging through turbulence*, J. Opt. Soc. Am. A **12** (1995), no. 7, 1559–1570.

[CSS87] M. Colavita, M. Shao, and D. Stealin, *Atmospheric phase measurements with the Mark III stellar interferometer*, Appl. Opt. **26** (1987), 4106–4112.

[DWHG00] W. Dent, H. Walker, W. Holland, and J. Greaves, *Models of the dust structures around Vega-excess stars*, Mon. Not. R. Acad. Soc. **314** (2000), 702–712.

[ESA00] ESA, *DARWIN, the Infrared Space Interferometer*, July 2000, Concept and Feasibility Study Report, ESA-SCI(2000)12.

[ESO] ESO, *Astroclimatology of La Silla*, http://www.eso.org/gen-fac/pubs/astclim/lasilla/diffrefr.html.

[FATK98] S. Fajardo-Acosta, C. Telesco, and R. Knacke, *Infrared photometry of β Pictoris type systems*, AJ **115** (1998), 2101–2121.

[FG03] M. Fridlund and P. Gondoin, *The Darwin mission*, Interferometry in Space (M. Shao, ed.), Proc. SPIE, vol. 4852, 2003, pp. 394–404.

[Gon02] P. Gondoin, *Simulations of GENIE nulling performances (the N band Bracewell configuration case)*, Tech. report, Space Science Department, European Space Agency, October 2002.

[Goo85] J. Goodman, *Statistical Optics*, Wiley & Sons, 1985.

[Gre85] R. Green, *Spherical astronomy*, Cambridge University Press, 1985.

[Her60] G. Herbig, *The spectra of Be- and Ae-type stars associated with nebulosity*, ApJ Suppl. Ser. **4** (1960), 337–368.

[HL86] R. Hill and R. Lawrence, *Refractive index of water vapor in infrared windows*, Infrared Phys. **26** (1986), 371–376.

[Hon85] S. Hong, *Henyey-Greenstein representation of the mean volume scattering phase function for zodiacal dust*, Astron. Astroph. **146** (1985), 67–75.

[KB00] M. Kuchner and M. Brown, *A search for exozodiacal dust and faint companions near Sirius, Procyon, and Altair with the NICMOS coronagraph*, Pub. A.S.P. **112** (2000), 827–832.

[KBK98] M. Kuchner, M. Brown, and C. Koresko, *An 11.6 micron Keck search for exo-zodiacal dust*, Pub. A.S.P. **110** (1998), 1336–1341.

[KBvDW01] H.-U. Käufl, P. Bouchet, A. van Dijsseldonk, and U. Weilenmann, *A sky-noise measurement and its implication for ground-based infrared astronomy in the 10 μm atmospheric window*, Experimental Astronomy **2** (2001), 115–133.

[KG01] B. Koehler and Ph. Gitton, *Interface control document between VLTI and its instruments*, December 2001, VLT-ICD-ESO-15000-1826.

[KH87] S. Kenyon and L. Hartmann, *Spectral energy distribution of T Tauri stars: disk flaring and limits on accretion*, ApJ **323** (1987), 714–733.

[KS01] M. Kuchner and E. Serabyn, *Modeling exozodiacal dust detection with the Keck interferometer*, accepted for publication in ApJ, 2001.

[KSC+03] B. Koresko, C.and Mennesson, E. Serabyn, M. Colavita, R. Akeson, and M. Swain, *Longitudinal dispersion control for the Keck Interferometer Nuller*, Interferometry in Optical Astronomy II (W. Traub, ed.), Proc. SPIE, vol. 4838, 2003, pp. 625–635.

[Kur79] R. Kurucz, *Model atmospheres for G, F, A, B and O stars*, ApJ Suppl. Ser. **40** (1979), 1–340.

[KWF+98] T. Kelsall, J. Weiland, B. Franz, W. Reach, R. Arendt, E. Dwek, H. Freundenreich, M. Hauser, S. Moseley, N. Odegard, R. Silverberg, and E. Wright, *The COBE diffuse infrared background experiment search for the cosmic infrared background. II. Model of the interplanetary dust cloud*, ApJ **508** (1998), 44–73.

[Lay97] O. Lay, *The temporal power spectrum of atmospheric fluctuations due to water vapor*, Astron. Astroph. Suppl. Ser. **122** (1997), 535–545.

[LGWP98] C. Leinert, U. Graser, R. Waters, and G. Perrin, *Internal concept review for MIDI, the mid-infrared interferometric instrument for the VLTI*, October 1998.

[Mas94] C. Masson, *Atmospheric effects and calibrations*, Astronomy with Millimeter and Submillimeter Wave Interferometry (M. Ishiguro & W. Welch, ed.), ASP Conf. Ser., vol. 59, 1994, pp. 87–95.

[Mat02] R. Mathar, *Computed dispersion of water vapor in the atmospheric window at 10 μm*, Tech. report, Max-Planck Institute of Astronomy, July 2002.

[Men99] B. Mennesson, *Interférométrie stellaire dans l'infrarouge thermique: observations d'environnements circumstellaires par optique guidée monomode et contributions à la mission spatiale DARWIN*, Ph.D. thesis, Université de Paris VII, December 1999.

[MG01] S. Ménardi and A. Gennai, *Technical Specifications for the PRIMA Fringe Sensor Unit*, December 2001, VLT-SPE-ESO-15740-2210.

[MGST01] R. Millan-Gabet, P. Schloerb, and W. Traub, *Spatially reseolved circumstellar structure of Herbig Ae/Be stars in the near-infrared*, ApJ **546** (2001), 358–381.

[MKO+00] T. Miyata, H. Kataza, Y. Okamoto, T. Onaka, T. Yamashita, and K. Nakamura, *Midinfrared Camera and Spectrometer (MICS) and sky noise measurements in the N-band*, Optical and IR Telescope Instrumentation and Detectors (A. Moorwood, ed.), Proc. SPIE, vol. 4008, 2000, pp. 842–851.

[MLP03] J. Meisner and R. Le Poole, *Dispersion affecting the VLTI and 10 micron interferometry using MIDI*, Interferometry in Optical Astronomy II (W. Traub, ed.), Proc. SPIE, vol. 4838, 2003, pp. 609–624.

[MOR02] B. Mennesson, M. Ollivier, and C. Ruilier, *On the use of single-mode waveguides to correct the optical defects of a nulling interferometer*, J. Opt. Soc. Am. A **19** (2002), no. 3, 596–602.

[MS97] V. Mannings and A. Sargent, *A high-resolution study of gas and dust around young intermediate-mass stars: Evidence for circumstellar disks in Herbig Ae systems*, ApJ **490** (1997), 792–803.

[NB91] N. Nightingale and D. Buscher, *Interferometric seeing measurements at the La Palma Observatory*, Mon. Not. R. Acad. Soc. **251** (1991), 155–166.

[Nol76] R. Noll, *Zernike polynomials and atmospheric turbulence*, J. Opt. Soc. Am. A **66** (1976), no. 3, 207–211.

[NPN+01] A. Natta, T. Prusti, R. Neri, D. Wooden, V. Grinin, and V. Mannings, *A reconsideration of disk properties in Herbig Ae stars*, Astron. Astroph. **371** (2001), 186–197.

[Oll99] M. Ollivier, *Contribution à la recherche d'exoplanètes - Coronographie interférentielle pour la mission DARWIN*, Ph.D. thesis, Université de Paris XI, December 1999.

[OM97] M. Ollivier and J.-M. Mariotti, *Improvement in the rejection rate of a nulling interferometer by spatial filtering*, Appl. Opt. **36** (1997), no. 22, 5340–5346.

[PR] P. Puxley and B. Rodgers, *Observing with GEMINI – Observing conditions constraints*, http://www.gemini.edu/sciops/ObsProcess/.

[Qui99] A. Quirrenbach, *Observing through the turbulent atmosphere*, Principles of Long Baseline Stellar Interferometry (P.R. Lawson, ed.), JPL publ., 1999, pp. 71–86.

[Qui03] ———, *VLTI performance and nulling needs*, Proceedings of the GENIE - DARWIN workshop, vol. SP-522, ESA, 2003.

[RC01] C. Ruilier and F. Cassaing, *Coupling of large telescopes and single-mode waveguides: application to stellar interferometry*, J. Opt. Soc. Am. A. **18** (2001), no. 1, 143–149.

[Rod81] F. Roddier, *The effects of atmospheric turbulence in optical astronomy*, Progress in optics (E. Wolf, ed.), vol. XIX, North-Holland, Amsterdam, 1981, pp. 281–376.

[Rya02] P. Ryan, *Scintillation correlations in the near-infrared*, Pub. A.S.P. **114** (2002), 462.

[Sch] J. Schneider, *The Extrasolar Planet Encyclopedia*, available at the URL: http://www.obspm.fr/encycl/encycl.html.

[SCH+88] M Shao, M. Colavita, B. Hines, D Staelin, D. Hutter, K. Johnston, D. Mozurkevich, R. Simon, J. Hershey, J. Hughes, and G. Kaplan, *The Mark III stellar interferometer*, Astron. Astroph. **193** (1988), 357–371.

[SR88] S. Shaklan and F. Roddier, *Coupling starlight into single-mode fiber optics*, Appl. Opt. **27** (1988), no. 11, 2334–2338.

[Tat71] V. Tatarskii, *The effects of the turbulent atmosphere on wave propagation*, Jerusalem: Israel Program for Scientific Translations, 1971.

[VC01] C. Vérinaud and F. Cassaing, *Piston control with adaptive optics in stellar interferometry*, Astron. Astroph. **365** (2001), 314–323.

[VDHO02] J. Vink, J. Drew, T. Harries, and R. Oudmaijer, *Probing the circumstellar structure of Herbig Ae/Be stars*, Mon. Not. R. Acad. Soc. **337** (2002), 356–368.

[WG03] R. Wilhelm and P. Gitton, *The VLTI environment and GENIE*, Toward Other Earths: Darwin/TPF and the Search for Extrasolar Terrestrial Planets, vol. SP-539, ESA's Publication Division, 2003, in press.